

Synthesis of model nanocatalysts for industrial applications

vorgelegt von
M.Sc. Xiao Xie
aus Hunan, China

von der Fakultät II – Mathematik und Naturwissenschaften
der Technischen Universität Berlin
zur Erlangung des akademischen Grades

Doktor der Naturwissenschaften
- Dr. Rer. Nat. -

genehmigte Dissertation

Promotionsausschuss:

Vorsizender: Prof. Dr. Michael Gradzielski
Gutachter: Prof. Dr. Reinhard Schomäcker
Gutachter: Prof. Dr. Arne Thomas
Gutachter: Prof. Dr. Rainer Haag

Tag der wissenschaftlichen Aussprache: 20.01.2014

Berlin 2014

D83

The work presented herein was carried out in the research group of Prof. Dr. Arne Thomas (functional materials group) and Prof. Dr. Reinhard Schomäcker (chemical engineering and catalysis group), at the department of chemistry at Technical University of Berlin, Germany, in the time between Apr. 2009 and Nov. 2013.

Acknowledgements

First of all, I would like to give my most sincere appreciation to my both supervisors Prof. Dr. Arne Thomas and Prof. Dr. Reinhard Schomäcker. Prof. Schomäcker, since I joined your group for my master thesis in 2007, I have been learning all the time from you. I will always remember the first german word I learnt from you: Fortschritt. As you said, progress is step by step, which is also your spirit and attitude to scientific research. Especially I want to thank you for helping me greatly to apply and extend the scholarship from BIG_NSE and organize my PhD projects. And Arne, as you said before, you and Prof. Schomäcker are my mama and papa from the lab. If Prof. Schomäcker is an affable papa, you are a “strict” but love mama. Because of your rich knowledge and fruitful ideas, I have learnt so much from group seminars and every discussion with you. I am also appreciated for the finance support which was a big favor from you.

My love colleagues, I want to thank you all. Without you, my PhD life would be not so colorful. Dear Elham, Kamal and “morphia members”, although my son is not named as HaJeRo, I always remember the nice lunch time when we were together. Rob, since you are the only person who got the “yellow print” from Kai, both Kai and I will be unable to forget you. Gabi, when I joined Prof. Schomäcker’s group, you are the first person who taught me to build up the setup, to use BET and GC, to wear the safety glasses the whole time in the lab, I appreciate your great help so much. Caren and Sören, I want to thank you not only for the TEM measurements, and also for so many times discussion with you. It was so nice of you to help me to find out and solve the problem from the synthesis procedure. Christa (Frau Löhr), Anne, Jens, Maria, Christina, Benjamin and Jen Dirk, thank you all for lots of measurements and documents preparation. Because of your nice help, my PhD work became much easier. Liebe Yasemin, you and your spinag cake always make me so happy, I will miss you. Melissa, Yan, Henritte and Dersy, although you all left me alone in Berlin, I am still thankful that I met you and be a friend of you. Our lady’s evening is one of the best moments of my Berlin memories.

My BIG_NSE family members, it was my luck to join this group and stayed with you for an unforgettable initial phase. And you, JP, you are the FATHER of this family. We all love you and need you. Sara my sweetie, I will remember your lovely smile and our nice time together, the journey to Rostock, the dinner on Reichstag, lunch breaks in campus coffee... Especially, I want to thank you for the Raman measurements. Jen, do you still remember our long scientific

discussion from the social evening party? At that time I was quite depressed because of the work. You encouraged me so much and try to help me out. Although we are not meeting so often any more, I always think of you and remember you.

I want to give my deepest acknowledgements to my family. Papa and Mama, thank you for giving me the life, growing me up and standing beside me to support me all the time with your unsubstitutable love. My Schatz Dirk, every time I had trouble or problem with my work, you always tried to help me for the solution. I haven't told you yet, thank you for experiencing my life together with me, thank you for loving me. And Kai, my love son, you are such a considerate gift for mummy. Can you imagine, if you cried every day, how could I finish my thesis? Because of you and you papa, I feel my life is complete.

Abstract

Different one-pot approach methods are used to synthesize metal oxide nanoparticles (MONPs) and noble metal nanoparticles (NMNPs) for specific catalytic applications. A solid solution of $\text{Ni}_x\text{Mn}_{1-x}\text{O}$ supported on porous silica is obtained by a one-pot approach, a combination of co-precipitation and the sol-gel process. Through adjusting the pH to 10, the gelation of sodium metasilicate is controlled at a low rate, which contributes to the high dispersion of metal precursors and subsequent forming metal precipitates in the network of the gel. By that $\text{Ni}_x\text{Mn}_{1-x}\text{O}$ nanocrystallites highly dispersed on amorphous silica can be obtained. Interestingly, $\text{Ni}_x\text{Mn}_{1-x}\text{O}$ catalysts show high activity for the dry reforming of methane (DRM) reaction. For the first time, the thermodynamic equilibrium (TDE) of the DRM reaction below 600 °C is achieved with $\text{Ni}_x\text{Mn}_{1-x}\text{O}$ catalysts. Compared to the bulk $\text{Ni}_x\text{Mn}_{1-x}\text{O}$ catalyst, silica supported $\text{Ni}_x\text{Mn}_{1-x}\text{O}$ exhibits highly improved catalytic performance in the DRM reaction. An optimized catalyst, $\text{Ni}_{0.05}\text{Mn}_{0.95}\text{O}/\text{SiO}_2$ (calcined at 750 °C), at the conditions of 600 °C and GHSV 80 L h⁻¹ g_{cat}⁻¹, is stable for 5 days and the conversion of methane is still 50% after 120 h time on stream.

Pd dispersed on silica xerogel is synthesized by a one-pot approach and tested for hydrogenation reactions. By using a water soluble polymer, the preformed Pd NPs are stabilized during the sol-gel process and therefore are highly dispersed on the xerogel. The polymer is removed completely by water extraction and can be reused for the next preparation. The obtained Pd/SiO₂ xerogel shows comparable activity as the homogeneous Pd sol catalyst in the hydrogenation of cyclooctadiene (COD). During the recycling applications, after 10 runs no deactivation or metal leaching is observed yet.

Another noble metal catalyst, Pt supported on SBA-15 is also synthesized by a one-pot approach and tested for both liquid-phase hydrogenation and gas-phase oxidation reactions. Poly(vinyl alcohol) (PVA) is employed as both a stabilizer for Pt NPs and a template to create interconnection between the channels in SBA-15. Under a certain concentration, Pt loading shows no influence on the surface area and pore structure of the support SBA-15. The obtained Pt/SBA-15 catalyst is highly active and stable in both oxidation of CO and hydrogenation of COD reactions. During the recycling applications, no Pt leaching or Pt NPs agglomeration is observed, indicating efficient immobilization of Pt NPs on SBA-15.

Zusammenfassung

Mehrere Eintopfreaktionen werden in dieser Arbeit angewendet um Metalloxid- und Edelmetall-Nanopartikel für die Anwendung in der Katalyse herzustellen. Eine feste $\text{Ni}_x\text{Mn}_{1-x}\text{O}$ Lösung wird durch die Kombination aus Co-Fällung und Sol-Gel-Prozesses an poröses Silikat angebracht. Hierdurch konnten $\text{Ni}_x\text{Mn}_{1-x}\text{O}$ Nanokristalle erhalten werden, welche höchst dispergiert und an Silikat angebracht vorlagen. Interessanterweise zeigen die $\text{Ni}_x\text{Mn}_{1-x}\text{O}$ Katalysatoren eine hohe Aktivität in der der trockenen Gasspaltung von Methan (DRM). Erstmalig konnte das thermodynamische Gleichgewicht der DRM Reaktion durch die Verwendung des $\text{Ni}_x\text{Mn}_{1-x}\text{O}$ schon unter 600 °C erreicht werden. Im Vergleich zu dem Bulk Katalysator besitzt der Silikat stabilisierte $\text{Ni}_x\text{Mn}_{1-x}\text{O}$ eine stark verbesserte katalytische Aktivität für die DRM Reaktion. Der optimierte Katalysator $\text{Ni}_{0,05}\text{Mn}_{0,95}\text{O}/\text{SiO}_2$ welcher bei 750 °C kalziniert wurde, ist bei 600 °C und GHSV 80 L h⁻¹ g_{cat}⁻¹ für 5 Tage stabil und der Umsatz von Methan beträgt noch 50% nach 120 Stunden im Gasstrom.

Pd auf Silikatxerogelen dispergiert wird durch eine Eintopfreaktion synthetisiert und für Hydrierungsreaktionen angewendet. Durch die Verwendung von wasserlöslichen Polymeren können die vorgebildeten Pd-Nanopartikel während dem Sol-Gel-Prozess stabilisiert werden und liegen daher höchst dispergiert in dem Xerogel vor. Das Polymer wird vollständig durch eine wässrige Extraktion entfernt und kann somit für die nächste Reaktion wiederverwendet werden. Das hergestellte Pd/SiO₂ xerogel zeigt eine hohe Aktivität, welche mit der von homogenen Pd-Solkatalysatoren in der Hydrierung von Cyclooctadien (COD) vergleichbar ist. Durch das Recycling durch zehnmalig durchgeführte Wasserextraktion wird kein nachteiliges Metall-Leaching beobachtet.

Zusätzlich kann ein Pt Edelmetallkatalysator, an SBA-15 angebracht, ebenfalls durch eine Eintopfreaktion hergestellt werden. Dieser wird auf dessen Aktivität in einer Flüssig- und Gasphasenoxidationen untersucht. Polyvinylalkohol (PVA) wird sowohl als Stabilisator für die Pt NPs als auch als Templat für die Herstellung von verbundenen Poren in SBA-15 verwendet. Bei einer bestimmten Konzentration hat die Pt Beladung keinen Einfluss auf den Oberflächeninhalt und die Porenstruktur des SBA-15-Gerüsts. Der hergestellte SBA-15-Katalysator ist während der Oxidation von CO und der Hydrierung von COD höchst aktiv und stabil. Das Recyclings konnte ohne nachteiliges Pt-Leaching oder Agglomerierungen der NPs durchgeführt werden.

Table of Contents

1. Introduction.....	1
1.1 Introduction to porous materials	1
1.1.1 Definitions of pores and classification of porous materials.....	1
1.1.2 Development of porous materials	2
1.1.3 Sol-gel synthesis of inorganic oxides.....	3
1.1.3.1 Sol-gel process applied to silica.....	4
1.1.3.2 Mechanism of sol-gel process of silica precursors	6
1.1.3.3 Different parameters for silica formation	8
1.1.3.4 Aging and drying in aerogel, xerogel and cryogel silicas	9
1.1.3.5 Advantages and limitations of sol-gel process.....	12
1.2 MONPs and NMNPs in catalysis	13
1.2.1 Application of NMNPs in hydrogenation reactions.....	13
1.2.1.1 Unique properties of NMNPs	14
1.2.1.2 Immobilization of NMNPs on porous materials.....	14
1.2.1.3 The role of stabilizer during formation of NMNPs	16
1.2.2 Application of MONPs in catalysis.....	17
1.3 Background of the DRM reaction.....	19
1.3.1 Thermodynamic equilibrium and mechanism of the DRM reaction	20
1.3.2 Solid catalysts in the DRM reaction.....	23
1.3.2.1 Metal oxides supported Ni catalysts	24
1.3.2.2 Supported nanoparticle catalysts.....	24
1.3.2.3 Solid solution catalysts	25
1.3.2.4 Perovskites catalysts	27
1.3.3 Deactivation in the DRM reaction	28

1.3.4 Challenge of investigating a catalyst for the DRM reaction.....	28
1.4 Immobilization of NMNPs --- a literature survey	31
2. Scientific goal	34
3. Experimental section.....	36
3.1 Amorphous silica supported NiMnO catalyst for the DRM reaction.....	36
3.2 One-pot synthesis of silica xerogel supported Pd NPs for catalytic applications.....	38
3.3 One-pot synthesis of Pt NPs supported on SBA-15 for catalytic applications	39
3.4 Characterization methods.....	40
4. Amorphous silica supported NiMnO for the DRM reaction.....	41
4.1 A solid solution of $\text{Ni}_x\text{Mn}_{1-x}\text{O}$ catalyst for the DRM reaction.....	41
4.2 Bulk $\text{Ni}_x\text{Mn}_{1-x}\text{O}$ solid solution for the DRM reaction.....	44
4.2.1 Synthesis and characterization of bulk $\text{Ni}_{0.2}\text{Mn}_{0.8}\text{O}_{\text{cp}}$ catalyst.....	44
4.2.2 Thermodynamic equilibrium of the DRM reaction under the standard conditions	46
4.2.3 Catalytic performance of $\text{Ni}_{0.2}\text{Mn}_{0.8}\text{O}_{\text{cp}}$ in the DRM reaction	47
4.2.4 What makes $\text{Ni}_{0.2}\text{Mn}_{0.8}\text{O}_{\text{cp}}$ so active for the DRM reaction?.....	48
4.2.5 Influence of Ni loading on the activity of NiMnO catalyst.....	50
4.2.6 Stability study of bulk $\text{Ni}_{0.2}\text{Mn}_{0.8}\text{O}_{\text{cp}}$ catalyst	52
4.3 NiMnO nanocrystallites supported on porous silica for the DRM reaction.....	57
4.3.1 Advantages of silica as catalyst support	57
4.3.2 Synthesis and characterization of $\text{Ni}_{0.2}\text{Mn}_{0.8}\text{O}/\text{SiO}_2$ nanocrystallites.....	58
4.3.3 Catalytic performance of $\text{Ni}_{0.2}\text{Mn}_{0.8}\text{O}/\text{SiO}_2$ in the DRM reaction	62
4.3.3.1 Activity study	63
4.3.3.2 Long term stability at 525 °C	64
4.3.3.3 Long time stability at 675 °C	68
4.3.4 $\text{Ni}_{0.05}\text{Mn}_{0.95}\text{O}/\text{SiO}_2$ calcined at high temperature	72

4.4 Summary and conclusion	79
5. Mesoporous silica supported NMNPs for catalytic applications	83
5.1 One-pot synthesis of silica xerogel supported Pd NPs for catalytic applications.....	83
5.1.1 Synthesis and characterization of silica xerogel supported Pd catalysts	84
5.1.2 Catalytic application of silica xerogel supported Pd catalysts	88
5.1.3 Conclusion	92
5.2 Ultra high surface area SBA-15 supported Pt NPs for hydrogenation reactions.....	93
5.2.1 Synthesis and characterization of SBA-15 materials.....	94
5.2.2 Synthesis and characterization of Pt@SBA-15 catalyst	99
5.2.3 Catalytic application of Pt@SBA-15 catalyst	101
5.2.4 Conclusion	105
6. Summary and conclusion	106
7. Outlook.....	109
Appendix A. Additional information.....	110
Appendix B. References.....	116
Appendix C. Characterization methods	126
Appendix D. Publications and conference contributions.....	139
Appendix E. Curriculum Vitae	140

List of abbreviations

Abbreviation	Explanation
AC	Activated carbon
BET	Brunauer-Emmet-Teller
COD	Cyclooctadiene
CVD	Chemical vapor deposition
DRM	Dry reforming of methane
hPG-b-mPEG	Hyperbranched polyglycerol-block-poly(ethylene glycol)
ICP-MS	Inductively coupled plasma mass spectrometry
LTM	Long term measurement
MOFs	Metal-organic frameworks
MONPs	Metal oxide nanoparticles
NM	Noble metal
NMNPs	Noble metal nanoparticles
PAMAM	Polyamidoamine
PEO	Poly(ethylene oxide)
POM	Partial oxidation of methane
PPI	Poly(propylene imine)
PVA	Poly(vinyl alcohol)
PVP	Poly(vinyl pyrrolidone)
RWGS	Reverse water gas shift
SMSI	Strong metal-support interaction
SRM	Steaming reforming of methane
TDE	Thermodynamic equilibrium
TEOS	Tetraethyl orthosilicate
TEM	Transmission electron microscopy
TMOS	Tetramethyl orthosilicate
TOF	Turn over frequency
XRD	X-ray diffraction

1. Introduction

1.1 Introduction to porous materials

A solid material that contains cavities, channels or holes can be regarded as a porous material. The presence of pores in a solid material can bring itself all sorts of useful properties that the corresponding bulk material would not have. Physical properties such as density, thermal conductivity and strength are dependent on the pore structure of the solid. The characteristics of a porous material, such as surface area, porosity and pore size distribution, can determine the behavior and performance of the material.¹ For example, porosity influences the chemical reactivity and the physical interaction of a solid with gases and liquids; high surface area porous materials are of great importance especially as catalysts, catalyst supports, thermal insulators, sensors, filters, electrodes and burner materials. The science and technology of porous materials has progressed steadily and is expanding in many new directions with respect to processing methods and applications.

1.1.1 Definitions of pores and classification of porous materials

In general porous materials have a porosity (volume ratio of pore space to the total volume of the material) between 0.2-0.95. Porous materials are of scientific and technological interest because of their ability to interact with atoms, ions and molecules not only at their outer surfaces, but throughout the bulk of the material. Not surprisingly, traditional applications of porous materials thus involve ion exchange, adsorption (for separation) and catalysis.²

This chapter is a literature survey about preparation methods of porous materials (mainly about the sol-gel process of silica materials), different methods of immobilizing MONPs and NMNPs on porous materials, and catalytic applications of these immobilized MONPs and NMNPs. It also contains the introduction of the DRM reaction including the reaction mechanism, the development of catalysts, and the deactivation problem. A short introduction of NMNPs supported on porous silica for catalytic applications was presented in the end.

Based on the accessibility for an external fluid, pores can be classified into open pores and closed pores. Materials with open pores which are connected to the surface of the material can be applied in adsorption, sensing, separation and catalysis. Materials with closed pores which are isolated from the outside are useful in sonic and thermal insulation, or lightweight structural applications. Pores have various shapes and morphology such as cylindrical, spherical, hexagonal and slit types, which is determined by properties and concentration of the template. According to pore size, porous materials are classified by International Union of Pure and Applied Chemistry (IUPAC) into three categories: microporous with pore diameter of less than 2 nm, mesoporous with pores between 2-50 nm and macroporous with pores larger than 50 nm. The distribution of sizes, shapes and volumes of the voids in porous materials directly relates to their ability to perform a desired function in a particular application.

1.1.2 Development of porous materials

Over the last decade, there has been a dramatic increase in synthesis, characterization and application of novel microporous materials.³ They are mostly used as heterogeneous acid and redox catalysts in petroleum industry and in the production of chemicals for various types of shape-selective conversion and separation reactions.⁴ Among the family of microporous materials, the best known members are zeolites which have a narrow and uniform micropore size distribution due to their crystallographically defined pore system. These materials are crystalline oxides with a tetrahedral framework structure that contains cavities in which 'guest' molecules can move freely.⁵ Usually zeolites are synthesized under hydrothermal conditions.⁶ Aluminosilicates zeolites can be synthesized through a zeolitization of a mixed solution containing Si and Al species, metal cations, organic molecules and water.

It is possible to say that zeolites are the most widely used catalysts in industry. They have become extremely successful as catalysts for oil refining, petrochemistry, and organic synthesis in the production of fine and speciality chemicals, particularly when dealing with molecules having kinetic diameters below 10 Å.⁷ One of their most useful properties is their ability for selecting molecules based on size (molecular sieving properties). But for some applications, such as cracking of hydrocarbons, and specifically hydrocracking, this advantage becomes a weakness due to the poor access of large reactants to the acid sites located inside the crystals.⁵

In 1961, organic molecules were used in zeolite synthesis as the first time reported by Barrer and Denny.⁸ They noted that the addition of quaternary ammonium cations sodium aluminosilicate gels increased the framework Si/Al ratio. Afterwards the application of organic materials in zeolite synthesis was quickly expanded.⁹ In 1992, the first paper reported on ordered mesoporous silicas (MCM-41, MCM-48, and MCM-50) synthesized in the presence of cationic surfactants via a supramolecular templating mechanism.¹⁰ Compared to the diffusion inside zeolites, mesoporous materials permit faster migration of guest molecules in the host frameworks, which enhances the mass transfer efficiency significantly in catalytic applications.

Metal-organic Frameworks (MOFs) have open framework structures, involving the coordination of metal ions to organic `linker` moieties. In the 1990s, MOFs materials gained interest, but an obvious shortcoming of these materials is the pores collapsing and the structural rearrangement upon guest removal or guest exchange. MOF-5, consisting of Zn^{2+} and 1,4-benzenedicarboxylate, is the first such solid exhibiting permanent porosity and it has a microporous volume larger than any known zeolite.¹¹ Porous MOFs are unlikely to compete with zeolites and other oxide-based porous materials in high-temperature-applications due to their limited long-term stability under such conditions and high cost. But the ability to prepare such solids, including frameworks with extra-large pores and high pore volumes, is nevertheless likely to open up many application possibilities in niche areas.² For example, the methane adsorption capacity of MOF materials based on copper dicarboxylates and triethylenediamine,^{11,12} exceeds that of any other known crystalline material.

The past decades have seen significant advances in the ability to fabricate new porous solids with ordered structures from a wide range of different materials. This has resulted in materials with unusual properties and broadened their application range beyond the traditional use as catalysts, adsorbents and ion exchangers. In fact, porous materials contribute to developments in areas ranging from microelectronics to medical diagnosis.²

1.1.3 Sol-gel synthesis of inorganic oxides

The sol-gel process is the most common and widely used process to synthesize porous materials. This process is a colloidal route with an intermediate stage including sol formation and gelation.

A sol is a stable suspension of colloidal particles in a liquid medium. A gel is a three dimensionally interconnected porous solid network that expands stably throughout the liquid medium. Metal salts and alkoxides are typical precursors which are responsible for the formation of porous materials, with the general formula of M_mX_n and $M(OR)_n$, respectively. In a sol-gel process, metal hydroxides, from hydrolysis of metal salts or alkoxides precursor, form small colloidal NPs which disperse in the solution so that a sol is formed. These small NPs link together to three dimensional networks filled with the liquid phase, which is the state of a gel. The precursor sol can either be deposited on a substrate to form a film (e.g. by dip-coating or spin-coating), casted into a suitable container with the desired shape (e.g. to obtain monolithic ceramics, glasses, fibers, membranes, aerogels), or used to synthesize powders (e.g. microspheres, nanospheres).

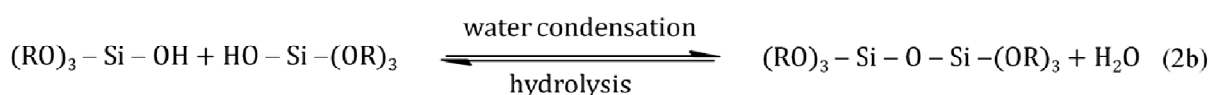
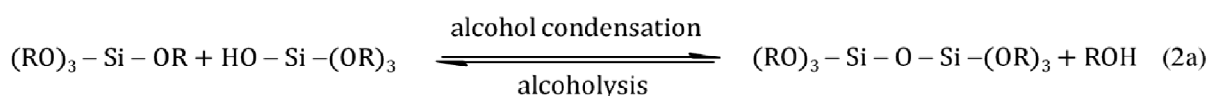
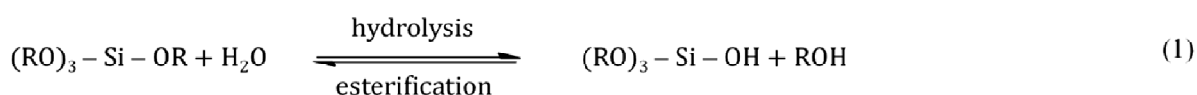
Main advantages of the sol-gel process are low temperature and ease of the process, high homogeneity, high purity, and high surface area of the obtained product. The average pore size, pore size distribution, surface area, refractive index and polarity of the resultant matrix can be controlled and tailored via manipulations in the sol-gel process conditions. Furthermore, the mild reaction conditions offer an opportunity to sol-gel derived materials for further modification and processing. For example, they can incorporate various molecules such as proteins, enzymes, dyes, organic and organometallic reagents into glass composites. The derived materials have diverse applications in optics, electronics, energy, space, biosensors, controlled drug release and separation technology.

1.1.3.1 Sol-gel process applied to silica

The sol-gel process of silica precursors has been studied much more extensively than that of any other precursors, due to the fact that Si atoms carry a lower reduced partial positive charge than metals such as Al, Ti and Zr. In case of these metals, the significant magnitude of partial positive charge δ^+ , e.g. 0.63 in $Ti(OEt)_4$ and 0.65 in $Zr(OEt)_4$,¹³ causes an easy nucleophilic attacking of oxygen atoms from water molecules, which carry a partial negative charge δ^- . In consequence, both the hydrolysis and condensation reactions of these metal precursors are fast. Hence, it is difficult to experimentally determine both reactions separately. Moreover, instead of polymer

network, oligomers or packed clusters are derived from the fast hydrolysis and condensation reactions. In contrast, Si carries a reduced partial positive charge, $\delta^+ \approx 0.32$ in $\text{Si}(\text{OEt})_4$,¹³ which yields slow gelation kinetics. Often the hydrolysis and condensation reactions of Si alkoxides need to be catalyzed, either with acids or bases. The most common silica precursors are alkoxysilanes $\text{Si}(\text{OR})_4$, such as tetramethyl orthosilicate, $\text{Si}(\text{OCH}_3)_4$, and tetraethyl orthosilicate, $\text{Si}(\text{OC}_2\text{H}_5)_4$, designated as TMOS and TEOS separately. Since the monomer has four arms, the resulting polymer is extremely branched and a monolithic sol-gel block can in principle be one huge molecule.

Most of the sol-gel procedures are aqueous, but nonaqueous sol-gel chemistry has also been developed. The following reaction procedure describes the sol-gel process of silica where R is an alkyl group. In the hydrolysis reaction, alkoxide groups are hydrolyzed and converted to hydroxyl groups. A complete hydrolysis (eq. 3) can be achieved when the stoichiometric molar ratio $\text{H}_2\text{O}/\text{Si}(\text{OR})_n$ is 4. Any intermediate species $[(\text{OR})_2\text{-Si}(\text{-OH})_2]$ or $[(\text{OR})_3\text{-Si}(\text{-OH})]$ would be considered as the result of partial hydrolysis (eq. 2a, 2b). Subsequent condensation reactions involve the silanol groups (Si-OH), produce siloxane bonds (Si-O-Si) and the by-products, alcohol or water.



The complexity of the polymerization process has two levels. The first one is the competition between the rate of the hydrolysis of SiOR groups (eq. 1), forming SiOH and ROH , and the rate

of the condensation/polymerization steps (eq. 2a and 2b). Under most conditions, condensation can start before a complete hydrolysis. Reaction conditions, such as pH, H₂O/Si molar ratio and catalyst, can force complete hydrolysis before condensation begins. Due to the immiscibility of the alkoxide and water, a mutual solvent, e.g. an alcohol, is usually used as homogenizing agent to facilitate the hydrolysis process¹⁴. The second one is that, in small oligomers, each of the SiOH and SiOR groups has a distinctly different electronic and steric environment, resulting in distinct hydrolysis and condensation rates for each of these groups.

1.1.3.2 Mechanism of sol-gel process of silica precursors

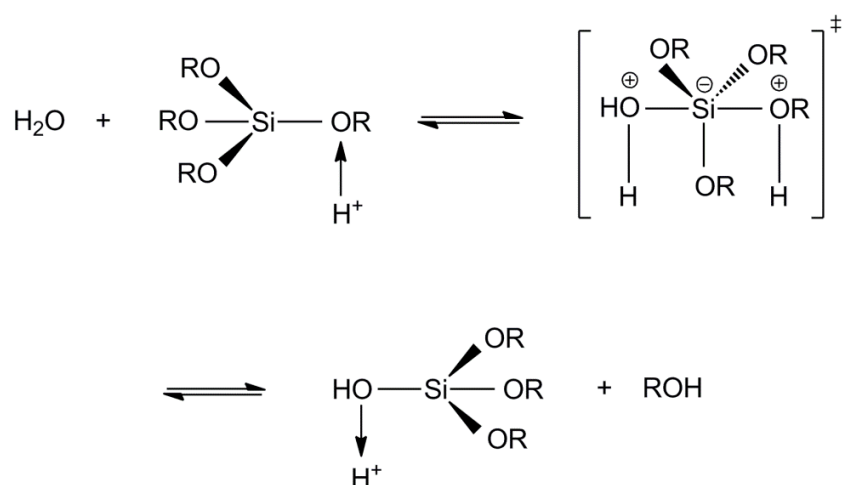
It is known that Si atoms possess relative low partial positive charge ($\delta^+ = 0.32$ in Si(OEt)₄)¹³ and the nucleophilic attack of O atom from water molecules becomes difficult. In consequence, both the hydrolysis and condensation reactions of silica precursors can be the order of months. In order to facilitate polymerization, Brønsted acids and bases are used to catalyze both the hydrolysis and condensation steps through nucleophilic substitution. Acids and bases cause different reaction mechanisms to catalyze hydrolysis and condensation.

In the acid-catalyzed reaction, the first step is the protonation of an alkoxyl group. Silicon donates electron density to the protonated alkoxyl group and becomes more electrophilic in the reaction and thus can be attacked by water molecule. This reaction follows a S_N2 mechanism. Figure 1.1 shows the hydrolysis of Si(OR)₄ catalyzed by acid.¹⁵⁻¹⁷

A water molecule attacks the silicon atom from the opposite side as that of protonated alkoxyl group and acquires a positive charge. The magnitude of the charge on the protonated alkoxyl group is correspondingly reduced with the ultimate effect of making the alcohol group labile. As the alcohol leaves, the silicon undergoes inversion of configuration, and the water group loses a proton taking the positive charge with it, as been proposed by Sommer and coworkers.¹⁵⁻¹⁷

Studies have shown that by reducing steric crowding around the silicon atom, an increase in the hydrolysis rate is observed. This type of mechanism favors the condensation reaction occurring between small clusters at terminal silicons, which form relatively long polymer chains with little branching. This process has been referred to as the reaction-limited cluster aggregation.¹⁸

Under acidic conditions:



Under basic conditions:

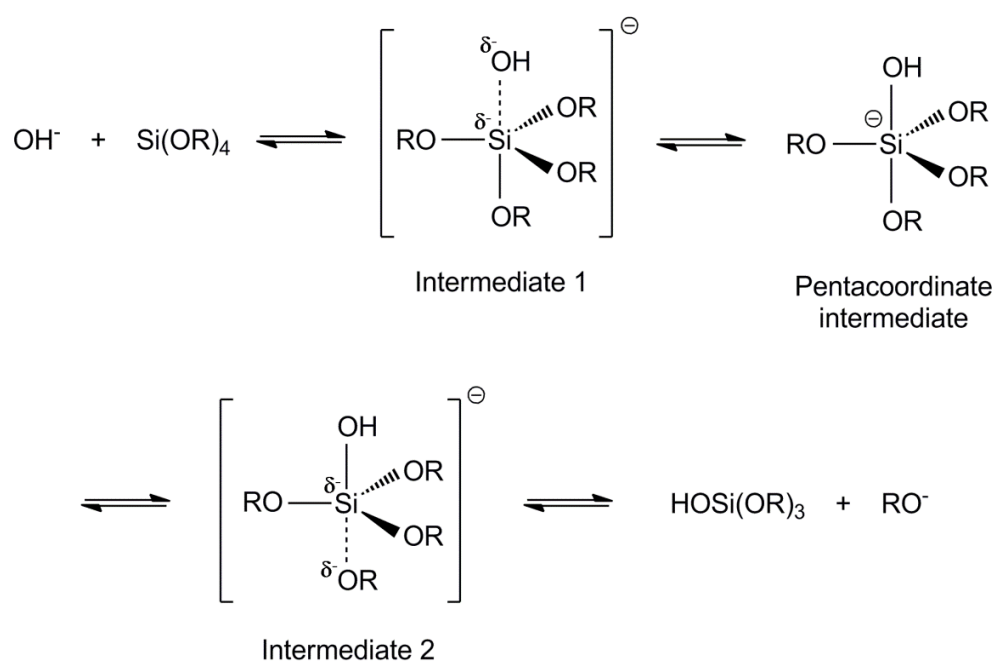


Figure 1.1 Acid catalyzed $\text{S}_{\text{N}}2$ -Si hydrolysis showing transition state (upper), and base catalyzed $\text{S}_{\text{N}}2^{**}$ -Si and $\text{S}_{\text{N}}2^*$ -Si hydrolysis showing intermediates 1 and 2 (bottom).

Under basic conditions, the first step is an attack of a hydroxide ion to the silicon. A $\text{S}_{\text{N}}2^{**}$ -Si and $\text{S}_{\text{N}}2^*$ -Si mechanism proposed by Pohl and Osterholtz is described in Figure 1.1 (bottom).¹⁹ In this

case a stable pentacoordinate intermediate is proposed, and $S_N2^{**}\text{-Si}$ and $S_N2^*\text{-Si}$ represent the rate-determining formation or decay of 2 intermediates, intermediate 1 and intermediate 2, respectively. The hydrolysis rate is sensitive to inductive and steric effects due to the formal negative charge at the silicon imparted to it from the electron withdrawing group of the hydroxide ion (OH^-) in the transition state between intermediate 1 and intermediate 2. Once the silicon has achieved a formal negative charge, the steric effects determine which group will leave. In Figure 1.1 (bottom) the OR group is larger than the OH group and will leave first, taking the negative charge with it. Steric interference prohibits clusters from undergoing condensation with each other.

From an examination of the two types of reaction mechanisms, it is apparent that the rate-determining step is different for the acid and the base catalyzed reactions. This affects cluster growth, and it is known that the overall final network produced is governed by the relative rates of hydrolysis and condensation. In the base-catalyzed route, the hydrolysis step is rate limiting. It produces a network which is more cross-linked than that produced under acidic conditions.

1.1.3.3 Different parameters for silica formation

Besides the reaction kinetics of gel formation, the nature of precursor materials, catalysts and solvents, the use of modifying agents, pH, the synthesis temperature, and the aging or drying conditions etc., all these factors can significantly affect the textural and structural characteristics of the resulted silica materials. Longer alkoxy groups such as $\text{Si}(\text{OR})_4$ ($\text{R} = \text{C}_5\text{H}_{12}$) cause incompletely reacted monomers which remain in the system and evaporate during drying and heating. Branching and increasing of the chain length of precursor substituent decreases the hydrolysis rate.²⁰ Compared to the transition metal alkoxides, TEOS is known to be less sensitive to hydrolysis, due to the poor electropositivity of Si.²¹ Thus, a change of surface charge can easily be carried out by changing pH to enhance the hydrolysis of silicon alkoxides. The pH also influences the dissolution of silica oligomers.²² At high pH values, where the particles may have a high solubility in the sol, more porous structures are formed. On the other side, under low pH values fine pore networks and dense structures are obtained due to low dissolution-precipitation rate.²³ The quantity of water in the sol-gel solution strongly influences the hydrolysis and

condensation kinetics. In case of Si(OR)_4 precursor, it is preferable when the stoichiometric molar ratio water/ Si(OR)_n is equal to or higher than 4 under acidic conditions, because a low water content or high dilution with alcohols (solvents) can lead to a high solubility of oligomers therefore a decrease in the yield of SiO_2 .²⁴ The temperature of aging and drying also takes an important role with respect to homogeneity, purity and porosity of the silica gels. Under atmospheric conditions, drying involves the loss of water, alcohol and other volatile components, which leads to gel shrinkage,²² and as a consequence to high stress in the structure.²⁵ If the strains cannot be released by relaxation, it will be difficult to obtain monoliths due to the cracks appearing.²⁴ Furthermore, it may create additional random porosity, deformation and breaking of the structure. When gel starts formation, both hydrolysis and condensation are not completed and some reactive silanols remain in the system. Aging at relative high temperature (100-500 °C) can accelerate hydrolysis and condensation and remove the organic species which leads to formation of covalent Si-O-Si bonds. In addition, increasing thermal treatment temperature leads to increasing porosity.²⁶

1.1.3.4 Aging and drying in aerogel, xerogel and cryogel silicas

Aging is the process of keeping the gel in the solution for a period of time in order to increase the strength of the gel network so that gels cracking and pores collapsing during drying can be avoided. It was demonstrated that condensation in silica gels continues long after gelation due to the large concentration of labile hydroxyl groups. Therefore, in a conventional sol-gel process, the aging lasts for at least 24 hours in order to obtain a stable and massive network.

Besides aging, the drying process can also affect the pore structures of silica gels. Once a stable three-dimensional polymer network is formed, it is necessary to remove the reaction media solvent. There are different types of drying methods, each of which produces materials with different properties. Therefore drying is another synthesis condition that needs to be taken into account when trying to control the final properties of the gel. The most widely used drying methods include (a) supercritical drying, i.e. eliminating the solvent in supercritical conditions (high pressures and temperatures), which produces an aerogel; (b) subcritical drying, i.e. drying the gel by simple evaporation of the solvent at ambient pressure, which produces a xerogel; (c) freeze-drying, i.e. the solvent is frozen and then removed by sublimation, which produces a

cryogel. Figure 1.2 shows a schematic representation for the obtaining of aerogels, xerogels and cryogels by the conventional method. The drying conditions determine the textural and structural properties of the final materials. Moreover, none of these drying methods are perfect. All the three methods have their advantages and disadvantages, as shown in Table 1.²⁷ The choice of method depends on the requirements of the material for specific applications.

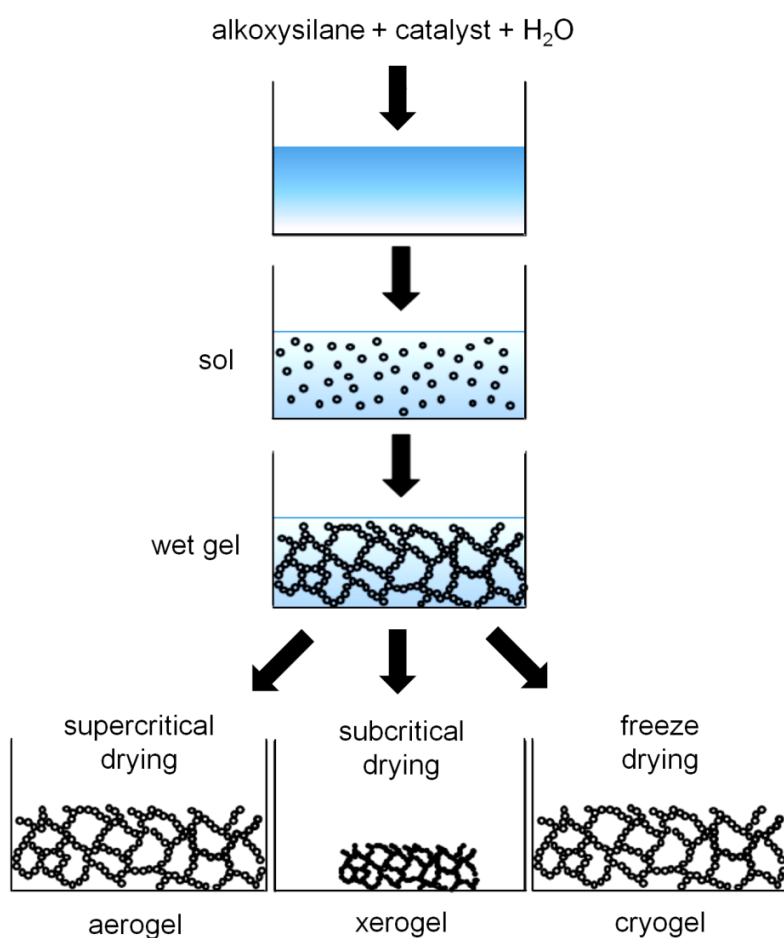


Figure 1.2 A schematic representation for the obtaining of aerogels, xerogels and cryogels by the conventional method.

Table 1 Summary of the main characteristics of the drying methods for the obtaining of silica gels.²⁷

Drying method	Material	Advantages	Disadvantages
Supercritical	Aerogel	- No shrinkage of pore texture	- Requirements of high T. and P. - Extremely high cost - Long process time - Necessarity of solvent exchange with CO ₂
Subcritical	Xerogel	- Simple, rapid and cheap - High surface areas and pore volumes	- Capillary forces destroy part of the initial porosity
Freeze	Cryogel	- Low shrinkage - High pore diameter	- High cost, long time, complicated method - With aqueous gel, need to exchange the solvent

Based on the removal of the solvent under high pressure and temperature, supercritical drying is the best way to preserve the porous texture and structural properties created during the synthesis of the gels. The resulting aerogels possess unique properties such as high pore volumes, low density, low thermal conductivity etc., which make them widely applied for pesticides, absorbers, fuel storage materials, thermal insulators, capacitors and so on. However, supercritical drying is also the most expensive and complicated drying method. In addition, this process is tedious and time consuming, requiring several days to obtain dry gels.

Subcritical drying is the cheapest and easiest drying process, and usually it is rapid compared to supercritical drying or freeze-drying. Xerogels can be easily obtained in the form of monoliths, powders and even films. The drying of gels under subcritical conditions is based on the evaporation of the solvent. When the solvent inside the pores of the material evaporates, the pores are subjected to high tension which causes the partial collapse of the porous structure. However, in many cases the partial shrinkage of the porous structure is not a significant issue, especially

when the desired porous texture is micro or micro-mesoporosity. Therefore, compared to aerogels or cryogels, xerogels have most potential for industrial applications.

The third drying method, freeze-drying, is based on the freezing and subsequent removal of the solvent by sublimation. This method is an effective way for preparing gels with a controlled pore structure. With freeze-drying, it is possible to obtain high mesopore volumes, but it is very difficult to prepare monoliths and in addition, this drying process is much more expensive than subcritical drying.

1.1.3.5 Advantages and limitations of sol-gel process

The sol-gel process has captured full attention both from academic and also industrial researchers by virtue of many advantages. This process not only applies for synthesis of oxide materials, it also permits the production of new hybrid organic-inorganic materials which do not exist naturally.²⁸ Using this process, highly pure products are obtained by simple purification of the precursors such as distillation, crystallization, or electrolysis. Furthermore, the kinetics of the various chemical reactions can be easily controlled by the low processing temperature and dilution of the medium. The sol-gel process offers the most outstanding advantages for mixed oxides systems in which the chemical homogeneity of the various elements can be controlled down to the atomic level.²⁸ This brings significant progress into the synthesis of solid solution and perovskites catalysts.

The main limitation to the sol-gel process, especially in the synthesis of ceramics, is the high cost of precursors, especially of alkoxides, which hinders the sol-gel synthesis of ceramics to the mass production of large scale materials. However, the sol-gel process becomes more interesting for synthesis of highly advanced ceramics.

1.2 MONPs and NMNPs in catalysis

Metals and metal oxides (MOs) play a very important role in many areas of chemistry, physics and materials science. The main apparent difference between bulk material and nanomaterial lays on the size difference. Compared to bulk materials, nano-sized metal and metal oxide exhibit unique physical and chemical properties due to their limited size and a high density of corner or edge surface sites, which makes them a class of novel materials with tremendous new applications. Within the last decades, many areas of industry have witnessed the advent of nanoscience. This PhD thesis is concentrated on applying NMNPs and MONPs as catalysts, so that this section is focused only on the uses of nano-sized noble metals (NMs) and MOs in catalysis.

1.2.1 Application of NMNPs in hydrogenation reactions

NM catalysts have been used in many industries, such as refinery, petrochemicals, polymer, chemicals, pharmaceuticals, and environment etc., because of their high activity and selectivity and stability under various reaction conditions. Not only advanced preparation technology but also unique properties of NM catalysts allow them to be used for wide range of applications.

NMNPs show high dissociative adsorption of hydrogen and oxygen. The dissociative adsorbed hydrogen and oxygen are very active and readily react with many substitutes under mild conditions, and byproduct formation can be minimized. Therefore, all NMs, including Pt, Pd, Rh and Ru, present a high activity and also high selectivity in different hydrogenation reactions.

Each NM catalyst shows unique characteristics, for instance, olefin hydrogenation can be accomplished with Pd/Al₂O₃ without hydrogenating aromatic systems at mild condition. In case of hydrogenation of phenol, Pd/Al₂O₃ is selective to cyclohexanone formation; Pt/Al₂O₃ is highly selective to cyclohexane formation, however, Rh or Ru/Al₂O₃ gives high cyclohexanol selectivity. Furthermore, preparation technology of precious metal catalysts has been advanced in recent years based upon nanotechnology. As a result, energy saving, high productivity, production cost reduction were achieved.

1.2.1.1 Unique properties of NMNPs

Catalytic activity and selectivity largely depend on particle size of NMs. For example, bulk gold is chemically inert, while gold particles with the diameter of several nanometers exhibit unexpected high catalytic activity. The term “size effect”, is used to describe the property change accompanied with particle size change. Figure 1.3 is the percentage of surface atoms as a function of the diameter of Pd particles. With reducing particle size, the performance of surface atoms became dominant when the particle size reduced to several nanometers.

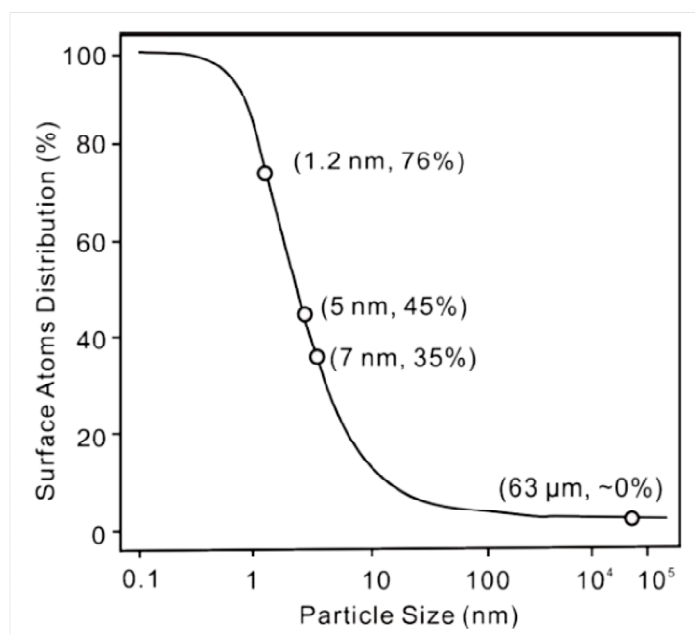


Figure 1.3 The percentage of surface atoms as a function of Palladium cluster diameter.

1.2.1.2 Immobilization of NMNPs on porous materials

Due to the extraordinary high activity, selectivity and stability, NMs possess irreplaceable position in catalysis. However, the extremely high cost limits the industrial application of NM catalysts. Therefore, immobilization of NMNPs becomes extremely important for the catalyst recyclability. NMNPs can be immobilized on porous supports by both chemical and physical routes. The review paper by R. J. White et al. introduced all preparation routes in detail.²⁹ Among

all those chemical routes, impregnation, co-precipitation and deposition-precipitation are most common preparation methods for immobilization of NM catalysts.

Impregnation: Impregnation of high surface area porous supports is the easiest method to prepare supported NM catalysts. It is commonly referred to as wetness impregnation. In this method, a metal precursor, often a metal salt is dissolved in the minimum quantity of solvent to afford its complete dissolution. The resulting solution is then added to a porous solid support and form a highly viscous mixture. The driving force of this process is capillary forces which absorb the metal precursor into the pores of the support. In an ideal case, the volume of metal precursor solution equals the pore volume of the support. The solvent is then removed from the mixture and the final solid is dried in a vacuum oven and subsequently calcined and reduced in H_2 (if necessary) prior to a reaction.³⁰

The impregnation method is suitable especially for preparing MO supported Pt catalysts since the corresponding Pt oxide interacts strongly with the MO (e.g. Al_2O_3 or TiO_2), which enhances the dispersion of Pt NPs. In general, this methodology often provides a broad NP size distribution due to a poor control over the growth of NMNPs. One possible mean to improve this is to lower the concentration of metal loading. Very often the metal loading is controlled below 10% in order to obtain a highly dispersed catalyst. On the other side, the number of active sites per unit is limited because of low metal loading.

Co-precipitation: The co-precipitation method involves the simultaneous precipitation of the NM and the support. Both the metal salt precursor and the support salt precursor dissolve in water (or other solvent) and precipitate with the help of a precipitate precursor (a base or a carbonate). Afterwards the precipitate is separated from the solution by filtration and then dried in vacuum and subsequently calcined and reduced in H_2 (if necessary) prior to a reaction. This method is one of the most common used methods for synthesizing solid catalysts because of its ease, simplicity, low cost and large scalability. However, very often, control of size and chemical homogeneity in the case of mixed-metal oxides are difficult to achieve.

Deposition-precipitation: Deposition-precipitation involves the dissolution of a metal precursor in an appropriate solvent, followed by pH adjustment (often basic) to achieve the complete precipitation of the metal hydroxide. The hydroxide precipitate is subsequently deposited on the surface of a support. Often, after deposition, the catalyst requires a washing step to remove

impurity ions (e.g. halogen ions) to avoid contamination. The obtained solid is then dried, calcined and reduced to form the final catalyst. The deposition-precipitation method allows preparing relatively stable well dispersed gold and Pd NPs in the range of 5 nm on various MO supports such as Al_2O_3 ,³¹ CeO_2 ,³² Fe_2O_3 ³³ and TiO_2 .³⁴ The main limitations of this approach are particle agglomeration and fragile support collapsing.

Precipitation in microemulsions: Compared to traditional impregnation, co-precipitation and deposition-precipitation methods, precipitation in microemulsion provides controllable and narrow particle distribution of NMNPs due to highly dispersion and limited concentration of NM precursor in each micellar solution. Generally, a microemulsion containing NM salt precursor is mixed with another microemulsion solution containing reducing agent, e.g. hydrazine, NM salt is therefore reduced and forms NMNPs which are stabilized in the microemulsion and form colloidal solution. By changing temperature or pH of the emulsion, the micelles break down and NMNPs can be deposited on any porous support. R. Parapat etc. used a thermal sensitive microemulsion system to immobilize Pt NPs on SBA-15. Pt NPs with particle size of nm are highly dispersed on different porous supports.^{35,36} The main drawback of this method is the incomplete release of nanoparticles from micelles. Other possible limitations are the usage of a large amount of surfactants and the difficulty of reusing the surfactants.

Chemical vapor deposition (CVD): Although it requires special instruments, CVD is still a promising route to prepare NMNPs and it has been regarded as a powerful method to generate highly dispersed metal NPs in a controllable way. It involves the vaporization of metals and growth of the NMNPs under high vacuum in the presence of an excess of stabilizing organic solvents and/or reducing agent. However, this method is often limited by the availability of NM precursor, vapor-pressure of the precursor and mass-transfer-limited kinetics.²⁹

1.2.1.3 The role of stabilizer during formation of NMNPs

By traditional impregnation, co-precipitation or deposition-precipitation methods, the resulting product of supported NMNPs have broad particle size distribution and a problem of particles agglomeration/sintering. In order to overcome this limitation and meanwhile take the advantage of simplicity and convenience from these traditional methods, preformed NMNPs, instead of NM

salts, have recently been employed during the synthesis. An effective method is to use stabilizer, often polymers, to avoid NMNPs agglomeration or sintering.

A number of polymers have been employed to enhance NMNPs stabilization properties, such as poly(vinyl alcohol) (PVA), poly(vinyl pyridine), dendrimers and fibers etc. In my PhD work, we have used a water soluble polymer with core-shell architecture, hyperbranched polyglycerol-poly(ethylene glycol) (hPG-b-mPEG), as a stabilizer for immobilization of Pt NPs on silica xerogel. Because of water solubility, this polymer can be separated from the system by ultrasonication in water and thereby be reused. The detail information about this project will be presented in chapter 5.1.

1.2.2 Application of MONPs in catalysis

In catalysis, the size of MOs is the most crucial property for the activity. In the bulk state, many oxides have wide band gaps and a low reactivity. A decrease in the average size of an oxide particle does in fact change the band gap^{37,38} with strong influence on catalytic activity.³⁹ Furthermore, with a nanostructure, the presence of under-coordinated atoms (like corners or edges) or oxygen vacancies in MONPs produce specific geometrical arrangements as well as occupied electronic states located above the valence band of the corresponding bulk material,^{40–42} therefore enhance the chemical activity of the MO catalyst.^{43,44}

MONPs can be obtained by two different approaches, which are so called top-down (from large to small dimensions) and bottom-up (from molecular scale to nanoscale) methods. A common top-down approach involves breaking bulk materials to nano-sized particles. This process is generally associated with the use of mechanical force, such as grinding and ball milling. By that the size distribution of obtained particles is quite broad and uncontrollable. In order to control morphological characteristics with certain chemical versatility, usually a bottom-up approach is employed to prepare nano-sized solid catalysts.

A number of specific methods have been developed to synthesize metal or MONPs, among which most common used methods are co-precipitation, sol-gel processes, the microemulsion technique, solvothermal methods, template or surface derivatized methods, chemical vapor deposition, (multiple-) pulsed laser deposition and so on. Most of the methods mentioned above

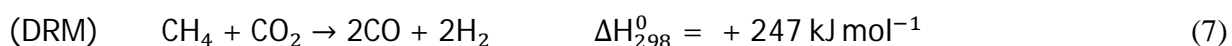
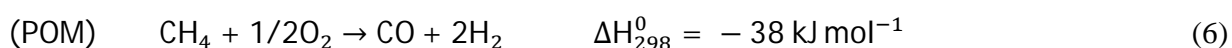
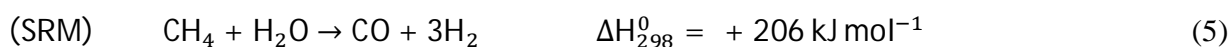
are similar as the methods for preparation of immobilized NMNPs so that will be not repeated here. Only sol-gel process and solvothermal method will be individually described.

Sol-gel processing: The method prepares MOs via hydrolysis of precursors, usually alcoxides in alcoholic solution, resulting in the corresponding oxo-hydroxide. Condensation of molecules releasing water leads to the formation of a network of the metal hydroxide: Hydroxyl-species undergo polymerization by condensation and form a dense porous gel. Appropriate drying and calcinations form ultrafine porous oxides. This method can be used to prepare porous TiO_2 , Al_2O_3 , ZrO_2 and Fe_2O_3 etc.

Solvothermal and hydrothermal synthesis: Solvothermal synthesis is a method for preparing a variety of materials such as metals, semiconductors, ceramics, and polymers. The process involves the use of a solvent in a sealed heated autoclave above ambient temperature and pressure that facilitates the interaction of precursors during synthesis. If water is used as the solvent, the method is called *hydrothermal synthesis*. The synthesis under hydrothermal conditions is usually performed below the supercritical temperature of water (374 °C). The process can be used to prepare different geometries including thin films, bulk powders, single crystals, and nanocrystals. In most of cases, the process is used for preparing nanocrystals. The limitation of this method is the requirement of expensive autoclaves and the availability of specific metal precursors.

1.3 Background of the DRM reaction

Fossil fuels are an important part of everyday life, providing us with multitudes of materials, energy and fuels. Since the twentieth century oil has played the most important role, it has become the driving force for the world's economy, being used for motor car, heated buildings, commercial air travel and so on. However, the finite and readily accessible oil reserves are being depleted and in recent years, the oil price has rocked. Therefore, alternative energy resources are required. One alternative is natural gas, which is composed predominantly of methane. Large amounts of natural gas are mainly found in remote areas, which hinder its full exploitation due to cost ineffective gas transportation, thus it is necessary to convert natural gas into more economically attractive products, such as liquid transportation fuels of higher energy density. There has been considerable investment in research programs, both academic and industrial, for the development of routes from methane to liquid synfuels as substitutes for petroleum. This research has led to a number of promising processes, e.g., the oxidative coupling of methane to higher hydrocarbons,⁴⁵⁻⁴⁸ the oxychlorination of methane to methyl chloride and subsequent conversion to ethane,^{49,50} and the direct production of methanol and other oxygenates.⁵¹⁻⁵³ Among all those processes, the following three attract greatest industrial interest: steam reforming of methane (SRM), dry reforming of methane (DRM) with carbon dioxide, and partial oxidation of methane (POM) with oxygen or air together with the associated reverse water gas shift (RWGS). All these processes are involved with the preparation of synthesis gas from natural gas, which is the most important step in the gas-to-liquid transformation.



Steaming reforming of hydrocarbons is the principle industrial process used for the manufacture of hydrogen and synthesis gas, and more than 80% of the world ammonia production is based on

the steam reforming of hydrocarbons. Nevertheless there are several aspects for further improvement or optimization: the expensive generation of superheated steam (in excess) at high temperature, the production of significant concentrations of CO_2 in the product gas via the reverse water gas shift reaction, and the production of high molar ratio of H_2/CO . In the case of the Fischer-Tropsch synthesis, high H_2/CO ratios limit the carbon chain growth.⁵⁴

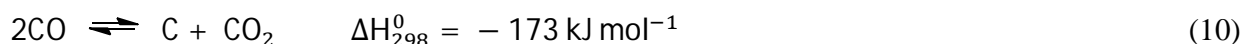
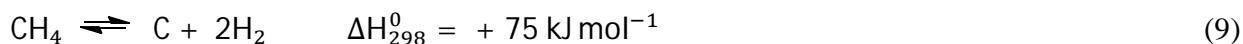
In contrast to endothermic SRM process, exothermic POM process needs much less energy. However, it requires pure oxygen, which is produced in expensive air separation units consuming up to 40% of the cost of a synthesis gas plant. Therefore, during the past half century the SRM process remained the main commercial process for synthesis gas manufacture.

Like the SRM reaction, the DRM reaction is also endothermic. It yields syngas with equal molar ratio of H_2/CO , which can be used directly for the Fischer-Tropsch synthesis of long-chain hydrocarbons. The addition of H_2 will be required to enhance the molar ratio of H_2/CO to 2. It also contributes to minimize of emissions from the green house gases (CH_4 and CO_2) to the environment. In addition, it can be combined with the SRM reaction to obtain variable H_2/CO ratios for various downstream processes. Therefore, methane reforming with CO_2 has been gaining increasing attraction especially in areas where water is not available. However, despite great scientific attention to this topic, no breakthrough technology has emerged so far as the process of methane conversion suffers from both thermodynamic and kinetic limitations. Besides the large amount of energy that is necessary, a suitable catalyst that would decrease the activation energy has yet to be developed.⁵⁵ Sintering of the catalyst and formation of coke are also known difficulties in high temperature DRM reaction. Therefore a suitable catalyst for the DRM process in industrial technology is still waiting for discovery.

1.3.1 Thermodynamic equilibrium and mechanism of the DRM reaction

The DRM reaction (eq. 7) is accompanied by several side reactions, of which the RWGS reaction (eq. 8), the methane cracking reaction (eq. 9) and the CO disproportionation reaction (the Boudouard reaction, eq. 10) seem to be the most important. Both the methane cracking reaction and the Boudouard reaction, produce carbon which deposits on the surface of the catalyst causing

deactivation. The catalyst deactivation in the DRM reaction will be additionally discussed in chapter 1.3.3.



Understanding the mechanism of the DRM reaction is the prerequisite for the discovery and design of a successful catalyst. The highly endothermic DRM reaction requires high reaction temperature to achieve a good conversion. The reaction equilibrium for the production of synthesis gas from CH_4 and CO_2 is typically influenced by the simultaneous occurrence of the RWGS reaction (eq. 8) which results in H_2/CO ratios less than unity.⁵⁶ The equilibrium conversions of CH_4 and CO_2 calculated by the program ARL SOLGASMIX are shown in Figure 1.4. The calculation is based on a feed stream at 1 atm total bar with $\text{CH}_4/\text{CO}_2/\text{He} = 1/1/1.8$. Due to the RWGS equilibrium, the conversion of CO_2 is always higher than that of CH_4 , which is in practice advantageous for producing gas streams with equal molar or lower H_2/CO ratio.

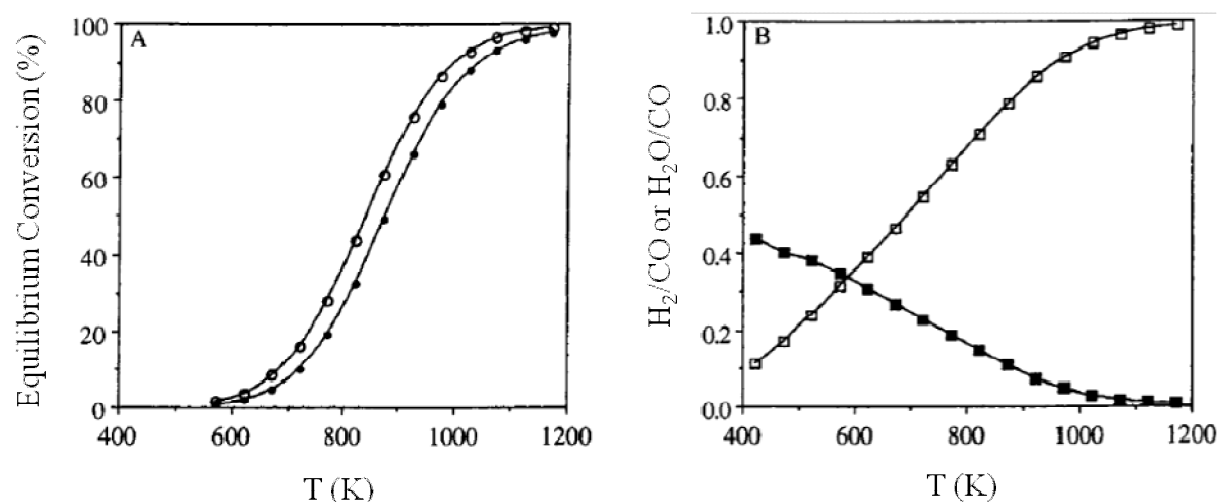
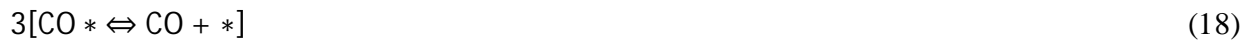


Figure 1.4 (A) Equilibrium conversion of CO_2 (o) and CH_4 (•); (B) product ratios of H_2/CO (□) and $\text{H}_2\text{O}/\text{CO}$ (■) for simultaneous dry reforming and RWGS reactions as a function of temperature. Reaction conditions: $P_{\text{tot}} = 1 \text{ atm}$, $\text{CH}_4:\text{CO}_2:\text{He} = 1:1:1.8$.

The activation of both CH₄ and CO₂ on transition metal surfaces may depend on both electronic and geometric factors such that their dissociative adsorption may be structure sensitive.⁵⁶ Numerous kinetic models have been proposed to describe the DRM reaction quantitatively, for example, the earliest report of a Langmuir-type rate expression for the DRM reaction was presented by Lewis et al. with a Cu/SiO₂ catalyst,⁵⁷ Bodrov etc. studied the DRM reaction over a nickel foil catalyst and fit their data to an expression which they originally derived to explain the kinetics of the SRM reaction.^{58,59} Richardson and Paripatyadar provided redox mechanisms based on a Langmuir-Hinshelwood approach. Zhang and Verykios provided a rate expression, derived from a Langmuirian model assuming that methane dissociation is the rate determining step.⁶⁰ The most consistent model currently available was proposed by Bradford and Vannice over supported Ni and Pt catalysts^{61,62}, which is shown in the following generalized reaction sequence:



It corresponds to the overall reaction stoichiometry:



From the above reaction sequences, * denotes an active site on the catalyst surface, → denotes an irreversible reaction, and ⇌ denotes a quasi-equilibrated reaction. The mechanism can be

summarized as that: the reversible dissociation of CH₄ to yield CH_x species and H₂, nondissociative adsorption of CO₂ on the support, H-promoted CO₂ dissociation in the metal-support interfacial region, the reaction of CH_x species with OH (or O) species to yield CH_xO species in the metal-support interfacial region, and CH_xO decomposition in the metal-support interfacial region to yield CO and H₂. Besides the proposed mechanism, Bradfords et al. also suggested that the proposed kinetic model for the DRM reaction should be applicable to SRM reaction.

The kinetic rate equation developed for dry reforming is shown in Eq. 20-23.⁶³ The water-gas shift reaction was also in the model reaction scheme, assuming first-order reaction in each reactant and the same rate constant as the CO₂ reforming reaction. The corresponding rate equations were formulated according to the Langmuir-Hinshelwood-Hougen-Watson formalism.

$$r_{ref} = \frac{k_1 K_{CH_4} K_{CO_2} (P_{CH_4} P_{CO_2} / P_{H_2}^{0.5} - P_{H_2}^{1.5} P_{CO}^2 / K_{ref})}{(1 + P_{CH_4} / P_{H_2}^{0.5} K_{CH_4} + P_{CO_2} K_{CO_2})^2} \quad (20)$$

Where

$$k_1 = 3.59 * 10^{21} \exp\left(\frac{332.04 \pm 52.40}{RT}\right) \quad (21)$$

$$K_{CH_4} = 2.89 * 10^{-8} \exp\left(\frac{-109.68 \pm 57.53}{RT}\right) \quad (22)$$

$$K_{CO_2} = 3.53 * 10^{-8} \exp\left(\frac{-125.39 \pm \pm 39.11}{RT}\right) \quad (23)$$

1.3.2 Solid catalysts in the DRM reaction

In the DRM reaction, in order to enhance the catalytic activity of a DRM catalyst, it is essential to maximize the number of active sites available to the reactants by dispersing the catalyst species onto a support or carrier surface. Furthermore, the larger the support surface the more likely that the catalytic species will be present as tiny, discrete particles (or crystallites). The smaller the

crystallites, the greater their individual surface to volume ratio and hence the greater total surface area per unit mass for a collection of small crystallites. This maximizing catalytic surface area per unit of mass enhances the number of sites per unit of mass upon which chemisorptions of the reactants and the DRM reaction occurs. To accomplish this, most commonly the catalyst components are dispersed on high surface area porous oxides such as SiO₂, Al₂O₃, TiO₂ or high surface area carbons. The DRM reaction has been concentratively studied over numerous supported metal catalysts, such as NMs^{62,64–67} and the group VIII transition metals,^{68–60} solid solution catalysts^{72–76} and also perovskites catalysts^{77–83}.

1.3.2.1 Metal oxides supported Ni catalysts

In terms of cost, Nickel-based catalysts appear to be the most suitable catalysts for the DRM reaction. An extensive study about Ni supported on Al₂O₃,^{60,84} CaO,⁸⁵ CeO₂,^{86–88} ZrO₂,^{89,90} MCM41,⁹¹ porous silica,^{71,70,69} zeolites,⁹² carbon nanotubes⁹³ etc. has been reported. In general, Ni-based catalysts show good activity when the temperature is above 650 °C. However, the fast deactivation caused by particle sintering and/or carbon deposition significantly inhibits the applications of these catalysts. One method to overcome this severe problem is adding promoters. Alkali and alkaline earth metals have been employed as promoters.^{79,86,95} By diluting the concentration of Ni, agglomeration of Ni clusters and carbon formation can be suppressed to some degree. On the other side, the activity of the catalyst is also drastically reduced by the promoter. Compared to alkali and alkaline earth metals, NPs have much stronger impact on the catalytic performance of Ni. Due to the SMSI properties of NPs and MO supports, both the activity and selectivity of Ni can be significantly improved. However, NM doped Ni catalysts have limited usage for industrial applications because of the high cost of NPs.

1.3.2.2 Supported nanoparticle catalysts

It is well known that NP catalysts are highly active and also selective in the DRM reaction. Various NPs, such as Ru,⁶⁴ Rh,^{96–98} Pd,^{64,73} Pt,^{80,91,92} and Ir, have been investigated extensively for the DRM reaction. It is reported that the strong metal-support interaction (SMSI) between

NPs and MO supports can significantly affect both catalytic activity and stability in the DRM reaction. The SMSI phenomenon was first observed between Group VIII NPs and reducible transition MOs (such as titania).¹⁰¹ It was found that this interaction drastically suppressed the chemisorption of H₂ and CO¹⁰² on the metal surface, which can be explained by simple site blockage of the metal surface due to the overlayer of the partial reduced transition MO. Because of reduced H₂ and CO adsorption, the equilibrium of the DRM reaction is shifted to the production of synthesis gas. Another specific property brought by SMSI is the generation of hydrogen spillover on the surface of the catalyst. Takayasu et al. have suggested that hydrogen spillover onto the support during CH₄ reforming helps to minimize inactive carbon deposition by shifting the equilibrium of reactions, thereby stabilizing CH_x intermediates on the support surface.¹⁰³ Furthermore, SMSI brings reversible reducibility of NPs and an increase of interfaces therefore stabilizes NPs in the form of thin and flat structure on the surface of MOs supports.¹⁰¹ Due to the high cost and poor availability, NPs are often only used as promoters to enhance the performance of Ni catalysts by suppressing the coke formation.

1.3.2.3 Solid solution catalysts

In the DRM reaction, two main kinds of catalysts, Ni- and the NM based catalysts, are employed and extensively studied. The cheap Ni-based catalysts show high activity and selectivity, but involve severe carbon deposition and are deactivated consequently. Compared to Ni-based catalysts, the NM-based catalysts suppress carbon deposition and thereby are highly stable, but not economic. Therefore, from an industrial standpoint, it is more practical to develop an improved Ni-based catalyst which is stable as well as active and selective.⁷⁴

One of the important developments for the DRM reaction is the realization of MgO-NiO solid solution catalyst by Ruckenstein et al.¹⁰⁴. As the best performing example of solid solution catalysts for the DRM reaction, MgO-NiO exhibited high conversion and selectivity and a rather high stability at a reaction temperature of 800 °C. It was suggested that the strong interactions between Ni and Mg inhibited both the sintering of NiO and MgO and the formation of the large clusters of Ni causing coke deposition.^{105,106} Fujimoto and his group also studied MgO-NiO solid solution catalyst and reported a ultra-stable catalyst Ni_{0.03}Mg_{0.97}O which presented neglectable deactivation after 100 days reaction at 850 °C.^{75,76} They presented a scheme of the reaction to

explain the high stability of $\text{Ni}_{0.03}\text{Mg}_{0.97}\text{O}$, shown in Figure 1.5. There are two paths for the activation of CO_2 . One is the activation of CO_2 adsorbed on support surface at interface between Ni metal and support (path I). The other path is the activation of CO_2 on Ni metal surface (path II). It was suggested that path I was more effective for the inhibition of carbon formation than path II. Since CH_x species are the reaction intermediates of whisker carbon formation which cause catalyst deactivation, rapid oxidation of CH_x species on Ni surface by oxygen species from CO_2 dissociation at metal-support interface is a key step for the inhibition of carbon formation.

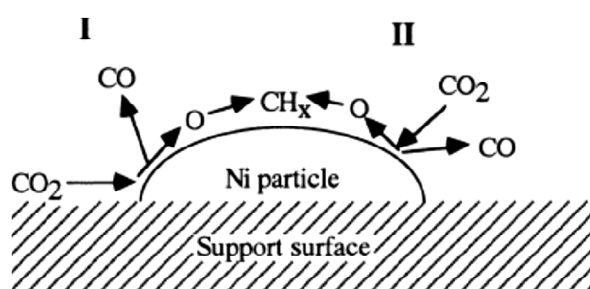


Figure 1.5 Scheme of the reaction of CH_x species with CO_2 .⁷⁶

However, this catalyst was difficult to reduce. The reduction conditions at 850 °C for at least 10 h are much harsher than normal reduction conditions with over 500 °C for 1 h. Moreover, due to the extremely low Ni loading, this catalyst required high temperature for activation. It showed neglectable activity when the reaction temperature was 500 °C.⁷⁵

Similar to NiO, CoO and FeO have the same crystal structure and comparable lattice parameters as MgO. It is also possible to inhibit carbon deposition by the formation of CoO-MgO¹⁰⁷ and FeO-MgO solid solutions.¹⁰⁸ However, the transition MOs exhibit cation deficiency, the defect concentration increasing from NiO to CoO to FeO by sequence, which leads to different behavior of NiO-MgO, CoO-MgO and FeO-MgO solid solution catalysts. The stoichiometric FeO with its rock salt structure is not stable below 10 GPa. At lower pressure, it is a nonstoichiometric complex with a nominal composition of $\text{Fe}_{1-3x}^{2+}\text{Fe}_{2x}^{3+}\text{O}^{2-}$ (x is between 0.04 ~ 0.12).¹⁰⁸ CoO-MgO solid solution catalysts showed similar performance as NiO-MgO catalysts. However, the former one caused hot spots in the application of partial oxidation of methane,^{109,110} which makes the process hazardous and uncontrollable. Later on, Ruckenstein and Wang reported that CoO-MgO

solid solution catalysts also have excellent activity, selectivity and high stability for the combination of POM and DRM reaction.¹¹¹ As an alternative solid solution catalyst, CoO-MgO has similar catalytic performance as NiO-MgO, but requires higher reaction temperature for methane conversion to syngas.⁷⁴

1.3.2.4 Perovskites catalysts

Perovskite type oxides have the same type of crystal structure as calcium titanium oxide (CaTiO_3). The general formula of perovskite type oxides is ABO_3 , in which the cation A of larger size, often rare earth metals, is responsible for the thermal resistance of the catalyst, while the cation B of smaller size, more often transition metals, is associated with the catalytic activity. In many cases, A and B site ions can be partially substituted by other ions and generate a large family of substituted oxides of general formula $\text{A}_{1-x}\text{A}_x'\text{B}_{1-x}\text{B}_x'\text{O}_3$, in which x is the substitution degree.^{112,113} The extensive use of these oxides as catalysts is not only due to their ability in stabilizing unusual oxidation states of the transition metal cation (B or B') but also to their ability for providing high oxygen mobility and also high structural stability.⁷⁸ These characteristics make perovskite oxides an attractive alternative to Ni based catalysts in the DRM reaction.

In general, the perovskite-based Ni catalysts show sufficiently good catalytic properties for the DRM reaction in terms of activity, coke resistance, and thermal stability.¹¹⁴ During the reaction, the perovskites precursors are reduced under H_2 atmosphere at elevated temperatures, by that the perovskite structure are partially or completely destroyed and the metallic Ni (0) is generated as active sites. However, perovskites catalysts need high activation temperature in the DRM reaction due to their endothermicity¹¹⁵⁻¹¹⁷. Furthermore, the strong metal-metal interaction in perovskites catalysts makes Ni difficult to reduce and therefore requires high reducing temperature.⁷⁸ Another limitation of perovskites is their small specific surface area (lower than $10 \text{ m}^2/\text{g}$)¹¹⁷ which heavily limits the complete exploitation of the catalytic potential of perovskites catalysts. Recently perovskite-based Ni catalysts were incorporated into a mesoporous SBA-15 support reported by Rivas et al..⁸² The addition of SBA-15 enhanced the dispersion and surface area consequently improved the activity and selectivity of the catalyst.

1.3.3 Deactivation in the DRM reaction

In the DRM reaction, carbon formation on metal surfaces and sintering of the catalyst take the main responsibility for the catalyst deactivation. Carbon formation can occur via two possible pathways which are the CH_4 decomposition reaction (eq. 9) and the Boudouard reaction (eq. 10) separately. Since CH_4 decomposition is endothermic while CO disproportionation is exothermic, the former one is the main contributor to inactive carbon formation at higher reaction temperature and conversely the latter one is the dominating reason at lower reaction temperature. However, due to the different equilibrium constant between CH_4 decomposition and CO disproportionation, the extent of graphitic carbon deposition during the DRM reaction decreases at higher reaction temperatures,⁶⁵ which indicates that CO disproportionation is the main contributor to inactive carbon deposition. Rodriguez reported that the rate-determining step for the formation of filamentous whisker carbon is the diffusion of carbon through a metal particle¹¹⁸. The driving force for this diffusion process is considered to be heat generated by exothermic surface processes, such as CO adsorption and disproportionation.

In overall, carbon formation is dependent on several parameters, such as the metal,^{64, 119} metal crystallite structure, metal-support interactions, support acidity,^{60, 120} and also the support basicity. Additionally, the catalysts which exhibit suppressed, or weak, CO adsorption can sufficiently resist excessive carbon formation during the DRM reaction, due to the inhibition of CO disproportionation.

1.3.4 Challenge of investigating a catalyst for the DRM reaction

Synthesis gas is an important raw material for several industrial processes, such as methanol synthesis, oxo-synthesis and Fischer-Tropsch-synthesis. Presently, synthesis gas is mainly generated via partial oxidation of coal, leading to carbon monoxide. In a subsequent process, hydrogen is formed by water-gas-shift-equilibrium from carbon monoxide and water. An alternative route to obtain synthesis gas is the DRM reaction. CH_4 and CO_2 are inexpensive due to their natural abundance. Conversion of these two molecules through the DRM reaction to higher-value compounds is of interest. However, due to some limitations, this process has not been operated in industry yet.

Considering the TDE limitation (shown in Figure 1.4) and the carbon deposition problem caused by the Boudouard reaction, it is practical to operate the DRM process at high temperatures ($> 1000\text{ }^{\circ}\text{C}$) with a high ratio of CO_2/CH_4 (> 1). However, under these conditions, particle sintering/agglomeration could become severe. Especially, operating a reaction at high temperatures is not economic from an industrial viewpoint. It is desirable to operate the DRM process at lower temperatures and with a ratio of near unity.

The DRM process could be applied in addition to an existing partial oxidation of methane in which carbon dioxide is produced as a side product, such as the oxidative coupling of methane (OCM). The structure of a combined process is shown in Figure 1.6.

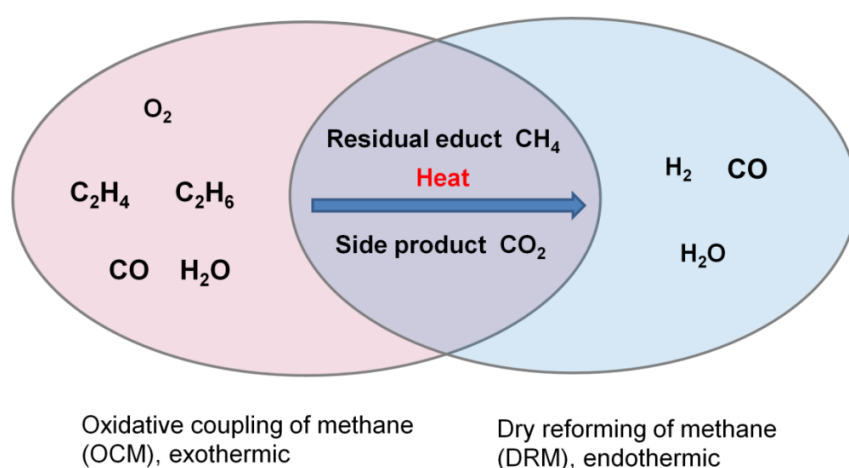


Figure 1.6 Scheme of combining the OCM and the DRM process

The heat produced by such exothermic oxidation reactions could be conveniently used for providing the energy for the endothermic DRM reaction. Besides the usage of heat from the OCM reaction, the main side product CO_2 and the residual reactant CH_4 can also be used for feeding of the DRM reaction. The OCM reaction could be operated at $800\text{--}850\text{ }^{\circ}\text{C}$. Considering the energy loss caused by the heat transfer between reactors where these two separate processes are conducted, it is of course highly desirable to operate the DRM reaction at a temperature 100 K below the OCM reaction.

As the most common catalyst in the DRM reaction, Ni has many advantages including its abundance, high activity and selectivity etc. However, the stability of Ni catalysts is still a main challenge in order to apply this type of catalysts for industrial processes. Because of the thermodynamic limitation of the DRM reaction, a relatively high reaction temperature (above 650 °C) is required in order to achieve a high conversion of CH₄ and CO₂. Under this condition, Ni catalysts can be deactivated because of particle sintering and carbon deposition.

The main challenge is that most of catalysts for the DRM reaction require high temperature to activate. Only a few catalysts reported recently showed activity between reaction temperature of 400-550 °C,^{89,121,90} but the TDE has not been achieved yet under 600 °C. Moreover, the Boudouard reaction is favoured at low temperatures, which deposits carbon onto the surface of active sites therefore causes deactivation.

1.4 Immobilization of NMNPs --- a literature survey

As discussed in chapter 1.2.1.2, there are various routes to immobilize NMNPs on porous supports. This chapter will present recent reported immobilization methods in detail and discuss the advantages and limitations of each method.

NM catalysts are used in a large number of commercially important processes, including hydrogenation, naphtha reforming, oxidation and automotive exhaust catalysis.¹²² Among these catalysts, palladium- and platinum-containing materials have received particular attention in recent years owing to their role as oxidation catalysts in automobile emission control systems as well as reforming catalysts for the production of high-octane gasoline. In order to achieve easy separation and catalyst recycling, NMNPs are often immobilized on a porous solid support.

Various methods and supports have been investigated in order to obtain homogeneous size and dispersion as well as high accessibility of the active species in the porous support, together with their immobilization inside the inorganic host materials to prevent any migration, leaching and agglomeration. Pd and Pt NPs have been immobilized on different supports such as spherical polyelectrolyte brushes,^{123,124} semiconducting MOs,¹²⁵ carbon materials¹²⁶ and alumina films¹²⁷. Mesoporous silica has been regarded as ideal and also most commonly used support due to its high surface area, tunable pore size, high accessibility, excellent stability, and straightforward synthesis.

Recently, it has been reported that Pt NPs with defined size and shape can be obtained in colloidal solution. This catalyst showed excellent activity in the electron transfer reaction between ferricyanide and thiosulfate.¹²⁸ Au NPs have been synthesized with relative precisely controlled particle size in a core-shell system.¹²⁹ The obtained catalysts can be used for selective reactions because the hydrophobic polymer shell allows only hydrophobic molecules to pass through and achieve the metal/metal oxide core. By this method, metal/metal oxide NPs are encapsulated in a polymer in a solution. During the applications, specific separation techniques, e.g. membrane ultrafiltration, are required for reusing the catalyst. The following discussion will mainly focus on NMNPs supported on inorganic oxides.

NMNPs can be immobilized on mesoporous silica supports by impregnation,^{130–133} grafting,^{134–136} and microemulsion^{35,36} etc. followed by calcination and reduction. One of the most prominent

methods is incipient wetness impregnation, in which the silica support is impregnated with NM precursors in solution, followed by thermal treatment and/or reduction to form NMNPs. Due to its simplicity and effectiveness, the wetness impregnation method is successful for large scale production of catalysts. However, NMNPs generated through this method often lack uniformity both in size and shape. To overcome the shortage of the traditional incipient wetness impregnation method, several groups have used hyperbranched or dendritic polymers, which acted as anchors to grasp NM ions, to functionalize mesoporous silica basing on the electrostatic and hydrogen bonding interactions between the dendrimers and the silica support. Cao's group used encapsulate Pd and Pt NPs in the mesopores of SBA-15 functionalized by polyamidoamine (PAMAM). The obtained NPs exhibited good activity in organic reactions.^{137,138} G.A. Somorjai's group also used PAMAM to synthesize Pt and Rh NPs with diameter of ~ 1 nm immobilized on SBA-15.¹³⁹ These NPs catalysts were active for ethylene hydrogenation without any pretreatments. Another often employed dendrimer is poly(propylene imine) (PPI).¹⁴⁰

Similar as these improved wetness impregnation methods, grafting methods can also be used for stabilization of NPs. In case of the former method, a specific polymer with dendritic structure is utilized as a stabilizer and this polymer is removed by thermal treatment at the end of preparation. The stabilization can be achieved by hydrogen bonding or electrostatic interactions between polymer and NPs. In contrast, using the grafting method, some ligands such as thiols and phosphines are inserted into porous matrix irremovably. NPs are stabilized by covalent bonds between NMs and ligands such as gold-thiols,¹⁴¹ cobalt-phosphine¹³⁶ etc. Because of these chemical bonds, NPs are strongly stabilized and particles agglomeration can be totally inhibited. It was also reported that by using reducing agents the *in situ* growth of NMNPs was controlled, and NPs with different particle size & narrow particle size distribution can be obtained.^{141–144} One question is: Do these chemical bonded NPs have any catalytic activity? Since above all the cited papers didn't mention any applications of presented grafted NPs, it is still critical to apply this type of materials in catalysis.

Recently there are increasing publications with one step approach to prepare metallic catalysts with NMNPs finely dispersed on a mineral support.^{145–147} In this method, support precursor, NM precursor, template and reducing agent are mixed in one solution. Under suitable conditions, a porous network is formed via sol-gel process, and meanwhile the NM precursor is reduced and

forms NMNPs located in the pores of the support. The template is removed by the following thermal treatment.

However, NMNPs are in situ formed during the sol-gel process, which makes it difficult to control the formation and growth of NMNPs which is most crucial to obtain highly dispersed NMNPs on porous supports. One efficient method to solve this problem is using preformed metal colloids or metal sols, in which NMNPs are stabilized by a polymer. By choosing a specific polymer stabilizer, adjusting the concentration of NM precursor and polymer, particle agglomeration is successfully suppressed and therefore the size of NMNPs can be controlled. During the subsequent immobilization process, due to the static electric interaction between the polymer and NMNPs, a high dispersion of NMNPs on a porous support can be ensured. One of the pioneer reports from A. Corma etc.¹⁴⁸ established the validity of the concept of such an approach. They synthesized gold NPs and stabilized them by capping with a quaternary ammonium ion ligand, with a long alkyl chain at one end and a triethoxysilyl group at the other end. The stabilized gold colloids joined the subsequent sol-gel process of TEOS, by that Au NPs were highly dispersed on mesoporous silica without severe agglomeration. By using this concept, Somorjai et al. prepared Pt NPs dispersed on SBA-15 using preformed Pt colloids stabilized by poly(vinyl pyrrolidone) (PVP).¹⁴⁹ They found Pt particle agglomeration during the synthesis and silica matrices disorder occurred severely under acidic conditions. Therefore, their process proceeded under neutral conditions which caused SBA-15 much lower surface area. More recently, it was reported that n-octylsilane was an optimal stabilizer for Pt colloids due to a strong bonding between n-octylsilane and Pt particles.¹⁵⁰ In this procedure the calcination temperature was limited at 320 °C in order to avoid particle sintering and pore collapse.

In my PhD work, we used a water soluble polymer hPG-b-mPEG and PVA individually to stabilize Pd and Pt sols for the subsequent sol-gel process. The detailed information about the procedure and the catalytic performance of the obtained catalysts will be presented in chapter 5.1 and 5.2. The advantages of the one-pot synthesis including the easy process, mild conditions, no need for support functionalization make this approach interesting for synthesizing catalysts for industrial applications.

2. Scientific goal

Solid catalysts in heterogeneous catalysis provide numerous opportunities for being recovered and recycled from reaction environments. These features can lead to improved processing steps, better process economics, and environmentally friendly industrial manufacturing. However, traditional solid catalysts with non-porous structure are limited in the accessibility of their active sites and thus the scope of reactions that they can accomplish is restricted. Soluble catalysts are active in a much larger variety of reaction types than traditional solid catalysts but suffer from the high challenge to be recycled. In order to combine the characteristics of high activity and selectivity from homogeneous catalysis together with the characteristics of recyclability and recoverability from heterogeneous catalysis, various booming developments focus on loading or immobilizing catalytic NPs/species on porous materials matrix.

During catalytic applications, controlling the size, shape and dispersion of NPs is the key to enhance their selectivity and activity. One mechanism to achieve this control is to utilize nanoporous materials as supports. For example, by employing polymers as stabilizers, the size and dispersion of NPs is able to be controlled because particle sintering can be avoided by static electric interaction between polymers and NPs. Immobilization and stabilization of NPs allow exploitation of the special properties that occur at this size regime. Therefore, the fusion between NPs and nanoporous materials technology represents one of the most interesting and rapidly expanding areas. It offers the opportunity to design specific catalysts for specific catalytic applications.

As a porous support, mesostructured silica (SBA-15, silica xerogel and amorphous silica) is most favorable due to its straightforward synthesis, high surface area, tunable pore size and stable structure. Moreover, in most cases silica support is inert during the reaction so that it will not poison or deactivate the catalyst. Therefore mesoporous silica was chosen as the support for immobilization of the model catalysts.

The goal of my PhD thesis is to develop the potential of mesoporous silica supported NMNP and MONP catalysts for industrial applications. In the project of “*Amorphous silica supported NiMnO for the DRM reaction*”, the specific goal is to design a suitable catalyst for the DRM reaction fulfilling the requirements of industrial applications. The catalyst should be economic,

active, stable and also easy to obtain. By following the structural change of the catalyst during preparation and reaction, we want to obtain the correlation between the structure transition and activation/deactivation of the catalyst. Thereby we set up a concept of stabilizing the catalyst by controlling its structure. Certainly it is interesting to investigate the structure and the properties of a catalyst and answer the following questions:

1. Which type of catalysts can be activated at relatively low reaction temperature?
2. How to avoid carbon deposition and catalyst deactivation?
3. How do the active sites form from the pre-catalyst and how do they interact with reactants and products during the reaction?
4. In which state are the active species stable?
5. How does the structure of a catalyst influence its catalytic performance?
6. Is there any interaction between the support and the metal?
7. How does the support influence the activity and the stability of the catalyst?

In another project “*Immobilization of NMNPs onto mesoporous silica by a one-pot approach for catalytic applications*”, the specific goal is to immobilize NMNPs on silica xerogel or SBA-15 with simple but controllable methods. Particle agglomeration is often a severe problem for the recycling of NMNPs catalyst, therefore, the dispersion and stabilization of NMNPs on the support are the most crucial factors for their catalytic performance. In order to obtain a NM catalyst with optimal performance, it is necessary to study some important issues:

1. How does the synthesis approach influence on the structure of the catalyst?
2. Which type of method is controllable and suitable for synthesizing industrial catalysts?
3. How to avoid particle agglomeration during the synthesis and during the catalytic applications?

3. Experimental section

3.1 Amorphous silica supported NiMnO catalyst for the DRM reaction

Preparation and characterization of $\text{Ni}_x\text{Mn}_{1-x}\text{O}$ and $\text{Ni}_x\text{Mg}_{1-x}\text{O}$ by co-precipitation method:

(1.25 ~ 5.00 mmol) $\text{Ni}(\text{OAc})_2 \cdot 4\text{H}_2\text{O}$ and (20.00 ~ 23.75 mmol) $\text{Mn}(\text{NO}_3)_2 \cdot 4\text{H}_2\text{O}$ (for $\text{Ni}_x\text{Mg}_{1-x}\text{O}$, the precursors were $\text{Ni}(\text{OAc})_2 \cdot 4\text{H}_2\text{O}$ and $\text{Mg}(\text{NO}_3)_2 \cdot 6\text{H}_2\text{O}$) were dissolved in 100 ml of deionized water. 0.055 mol NaHCO_3 was dissolved in 50 ml of deionized water. The NaHCO_3 solution was added into the metal precursor solution drop wise under vigorous stirring. Molar ratio $\text{Ni}(\text{OAc})_2:\text{Mn}(\text{NO}_3)_2/\text{Mg}(\text{NO}_3)_2:\text{NaHCO}_3 = x:(1-x):2.2$. The mixture was stirred for 8 h at room temperature, followed by filtration of the precipitate and washing with deionized water. The obtained solid was dried in vacuum at 80 °C overnight and then calcined at 500 °C for 4 h and subsequent reduction at 500 °C for 4 h. Quantitative yield was observed. The obtained materials are named $\text{Ni}_x\text{Mn}_{1-x}\text{O}_{\text{cp}}$ and $\text{Ni}_x\text{Mg}_{1-x}\text{O}_{\text{cp}}$ respectively.

Preparation and characterization of $\text{Ni}_{0.2}\text{Mn}_{0.8}\text{O}$ by co-precipitation/sol-gel method:

25 mmol $\text{Na}_2\text{SiO}_3 \cdot 5\text{H}_2\text{O}$ was dissolved in 50 ml deionized water. First 30 ml NaHCO_3 (55 mmol) aqueous solution and later a certain amount of HCl (2 M, ~ 20 ml) were added into the Na_2SiO_3 solution, the pH was adjusted to 9-10 by HCl. Subsequently 50 ml of metal precursor solution, containing 5 mmol $\text{Ni}(\text{OAc})_2 \cdot 4\text{H}_2\text{O}$ and 20 mmol $\text{Mn}(\text{NO}_3)_2 \cdot 4\text{H}_2\text{O}$ was added into the mixture under vigorous stirring (note that the solution becomes immediately viscous, thus manual stirring is advisable). Molar ratio $\text{Na}_2\text{SiO}_3:\text{Ni}(\text{OAc})_2:\text{Mn}(\text{NO}_3)_2:\text{NaHCO}_3 = 1:x:(1-x):2.2$ (150 ml mixture contains 25 mmol metal precursors). In the following step, the whole mixture was stirred at room temperature for 24 h, followed by filtration of the precipitate and washing with deionized water. The obtained solid was dried in vacuum at 80 °C overnight and then calcined at 500 °C for 4 h with subsequent reduction at 500 °C for 4 h. The obtained materials are named $\text{Ni}_{0.2}\text{Mn}_{0.8}\text{O}_{\text{cp-SiO}_2}$. The catalyst $\text{Ni}_{0.05}\text{Mn}_{0.95}\text{O}_{\text{cp-SiO}_2_750}$ (molar ratio of Ni/Mn = 5/95) was calcined first at 500 °C for 4 h then at 750 °C for another 4 h with subsequent reduction at 750 °C for 4 h. Quantitative yield was observed. The materials are investigated before the reduction process.

Catalyst testing:

The catalytic testing was performed in a fixed-bed reactor made of silica with an inner diameter of 5 mm and a length of 40 mm. Silica is known to have no catalytic activity on the reaction in the examined temperature range of 400-850 °C. The reactor was heated by an electric furnace (HTM Reetz). The catalyst bed consisted of varying masses of catalyst and silica grains (Merck) with a total volume of 1.25 ml.

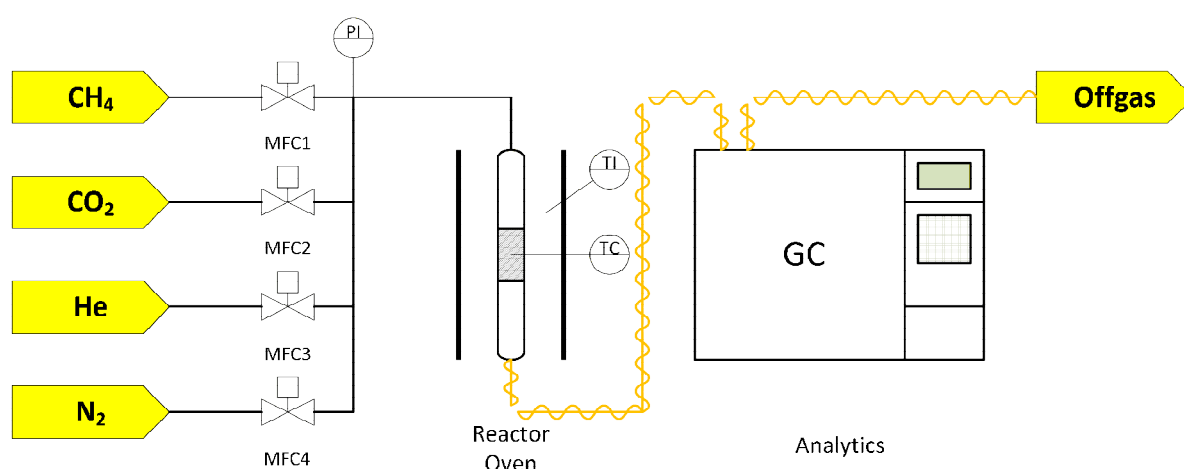


Figure 3.1 The scheme of experimental setup of the DRM reaction.

Before experiments started, the catalysts were in situ reduced in a pure hydrogen flow of 15 ml min⁻¹ at a temperature of 500 °C for one hour. Accordingly, the gas composition was chosen to be CH₄:CO₂:N₂ = 2:2:1 for both screening and long term experiments. Thereby, nitrogen was taken as internal standard for the gas analysis. Samples were taken after 25 min steady-state at each temperature point. Process gas analysis was performed by gas chromatography (HP 5890 Series II) equipped with methanizer, TCD, FID and mole sieve 5 Å and Hayesep Q columns (both Supelco). Argon was used to be carrier gas to detect small amounts of hydrogen in the process gas.

3.2 One-pot synthesis of silica xerogel supported Pd NPs for catalytic applications

Preparation of preformed Pd sol Pd/hPG-b-PEG (by Sabrina Nowag):

200 μl of H_2PdCl_4 solution ($1.07 \times 10^{-2} \text{ mol L}^{-1}$) were added into 10 ml of an aqueous solution of the polymer hPG-b-mPEG (10 g L^{-1}). The mixture was left at r.t. for 24 h. 1 ml of a freshly prepared aqueous NaBH_4 solution (the molar ratio of NaBH_4 to HPdCl_4 is 4, excess of NaBH_4 is expected to ensure the complete reduction of HPdCl_4 to Pd) was added at once, upon which the brown solution slowly turned into black, indicating the formation of Pd NPs. At 25 °C, the reduction of Pd ions by the polymer was finished within one day.

Preparation of SiO_2 xerogel:

Silica gel was prepared by adding 12-20 ml 2 M HCl drop wise to 1 ml TMOS. The mixture was stirred 8 h at 75-80 °C. After precipitation, water washing and overnight drying in vacuum oven, it yields a white solid monolith.

Preparation of Pd/ SiO_2 catalyst:

- 1) The catalyst was prepared by mixing the metal sol of hPG-b-mPEG stabilized Pd (5 ml) with 2M HCl (12-20 ml), followed by drop wise addition of TMOS (3 ml). Molar ratio of the precursor sol was hPG-b-mPEG/Pd/TMOS/ H_2O = 10^{-6} : $0.5 \sim 2 \times 10^{-4}$:0.015:0.22. The mixture was stirred in a closed flask at room temperature for 15 min, and subsequently at 75-80 °C for 8 h.
- 2) A gray gel was obtained in step 1. This solid was precipitated and washed with ultrasonication in water for 15 min \times 4 times.
- 3) The final product was obtained in the shape of monolith by drying the solid from step 2 in a vacuum oven at 60 °C overnight. It was meshed into powder before being applied into hydrogenation reactions.

3.3 One-pot synthesis of Pt NPs supported on SBA-15 for catalytic applications

Preparation of SBA-15-V:

0.5 g of P123 ($\text{EO}_{20}\text{PO}_{70}\text{EO}_{20}$, $M_w = 5800$ g/mol) was dissolved in a mixture of distilled water (7.5 g) and 2 M HCl solution (15.0 g), with continuous stirring and the temperature was controlled at ~ 35 °C; after the P123 was fully dissolved, a freshly prepared 1 wt.% aqueous PVA ($M_w = 130,000$ g/mol) was added in different amounts. To this solution, 1.1 g TEOS was added and the resulting mixture was stirred at ~ 35 °C for 24 h, subsequently poured into a teflon-lined autoclave and aged at $80 \sim 150$ °C for another 24 h. Finally, the sample was filtered, dried at 100°C overnight and calcined at 500 °C for 4 h. The samples show comparable thermal and long-term stability under ambient conditions as observed for pure SBA-15 materials.

Preparation of Pt/SBA-15:

The platinum sol was prepared by mixing 100 ml 0.015 M H_2PtCl_6 solution with 3 ml 0.1 wt.% PVA solution. Subsequently 0.1 M NaBH_4 (20 equ. to Pt) was added in drop wise. The sol was stirred 5 min for the further step. The PVA stabilized Pt sol was used to prepare the Pt/SBA-15 catalyst. The loading of platinum measured by ICP analysis was 0.29 wt.%.

3.4 Characterization methods

BET: Nitrogen sorption isotherms were measured at liquid-nitrogen temperature (-196 °C) with an Autosorb-1. The samples were degassed at 150 °C overnight before the measurement. The BET surface area was calculated by multiple-point (five-point) measurement.

ICP-MS: The mass content of metals was measured by ICP-MS Element 2 (Varian Inc., USA), with sample gas flow 0.863 L/min and plasma power 1350 W.

Raman spectra: The measurement was done using a Labram 3 with 10 mW 647 nm excitation.

Solid state NMR: The solid-state NMR ^{13}C CPMAS (Cross Polarization Magic Angle Spinning) measurements were carried out using a Bruker 4 mm double resonance probe-head operating at a spinning rate of 10 kHz. ^{13}C chemical shifts were referenced externally to tetramethyl silane using adamantane as a secondary reference.

TEM: TEM images were obtained on a Philips CM200 instrument, operated at 120 keV, using amorphous carbon-coated copper grids. The specimens were dispersed in water with ultrasonication and loaded onto a copper grid.

TPR: 65 mg catalyst was used for TPR/TPO measurement. TPR experiment proceeded under a mixed gas with 10% H_2 in N_2 . Gas flow velocity was 60 ml/min. Reduction temperature was between r.t.-750 °C with a heating rate of 1 K/min. The samples were held at 750 °C for 30 min. TPO experiment was carried out under air with a gas flow velocity of 60 ml/min. Oxidation temperature was between r.t. and 800 °C with a heating rate of 10 K/min and the samples were held at 800 °C for 30 min.

XRD: XRD was performed using a Bruker D8 Advance X-ray diffractometer with $\text{Cu K}_{\alpha 1} = 1.5418 \text{ \AA}$ radiation between 2° and 90° (2 θ).

4. Amorphous silica supported NiMnO for the DRM reaction

4.1 A solid solution of $\text{Ni}_x\text{Mn}_{1-x}\text{O}$ catalyst for the DRM reaction

So far the solid solution NiO-MnO has not been reported as a catalyst yet. It is the first time that, here in my PhD project, NiO-MnO solid solution is applied for the DRM reaction. Before considering this material as a catalyst for the DRM reaction, it is necessary to mention SMSI, which is described in the chapter 1.3.2.2 (page 24). It appears that these interactions require transition metal cations with d orbital electrons. The surface transition metal cations must be reduced to produce oxygen vacancies, so that a charge transfer from the reduced cation to the adjacent metal atom will occur, resulting a strong anionic attraction between the support and the metal.¹⁵¹ The overlap of metal atom and adjacent cation d orbital electrons causing a weak covalent bond is another contribution. For example, when TiO_2 is reduced to $\text{TiO}_{3/2}$, Ti^{4+} with a d^0 electron configuration is converted to Ti^{3+} with a d^1 configuration. The absence of SMSI with some transition MOs, e.g. ZrO_2 , was attributed to the difficulty of reducing their d^0 cations to the d^1 state.¹⁰² Another important prerequisite is the reducibility of the transition metal oxide.

Tauster et al. extensively investigated SMSI behavior with a wide range of MOs supporting group VIII metals. It was found that, similar to titania, oxides of manganese, niobium, vanadium and tantalum showed also SMSI. But no SMSI was evident for alumina, silica, magnesia, scandia, hafnia, zirconia, or yttria.¹⁵¹

The strength of SMSI is determined by the migration rate of transition MOs to the surface of metals. It is proven that the migration of MnO_x occurs much more rapidly than that of TiO_x . An

This chapter discusses the main project of my PhD work, which is about the DRM reaction. In this project, I collaborated with Dr. Torsten Otremba (a former colleague from AK Schomäcker, currently a postdoc in BasCat – UniCat BASF Joint Lab). My work was mainly about the synthesis and characterization of the catalyst, finding out the relationship between the structure and catalytic properties of the catalyst by following the structural changing during the catalytic applications, so that optimizing the catalyst through designing and adjusting the structure of the catalyst. Torsten contributed most of catalytic data over the DRM reaction. Later on Mr. Patrick Littlewood (AK Schomäcker, TU Berlin) took over the DRM project and also contributed a part of the catalytic data (noted in the results discussion).

experimental study has shown that a 12 nm thick Ni film deposited on TiO_2 showed signs of TiO_x after 10 min exposure to H_2 at 425 °C.¹⁵² In contrast, a 15 nm thick Ni film deposited on MnO , shows substantial amounts of MnO_x on its surface after 100 s of vacuum annealing at 230 °C.¹⁵³ This means that MnO has even much stronger interaction with group VIII metals than TiO_2 . Most NMs supported on transition MO supports show SMSI which make them highly stable as well as active over the DRM reaction. However, considering the cost, a solid solution or a perovskite catalyst will be more feasible for industrial applications.

Because of the SMSI between Ni and MnO , we expected that when a MnO supported Ni catalyst is applied for the DRM reaction, this catalyst should show a significantly reduced H_2/CO adsorption (compared to Ni supported on other oxides), which drives the DRM reaction to the production of H_2 and CO . Ni^0 clusters can be stabilized either by spreading of Ni^0 onto the surface of MnO or by fast migration of MnO onto Ni^0 clusters therefore minimizing the size of Ni^0 clusters and also suppressing Ni^0 clusters agglomeration. Mn has already been used as a doping element in order to increase the stability of Ni catalysts in the DRM reaction.^{154,94,87,155,156} The enhanced stability of Ni is owing to the partial coverage of the Ni surface by patches of Mn so that CO_2 adsorption on the surface of Ni is increased, resulting in the formation of surface carbonate species which remove carbon precursors from the catalyst surface.^{94,87} This means that Mn surface shows stronger CO_2 adsorption than Ni surface and therefore accelerate the reverse Boudouard reaction and remove the surface carbon.

Instead of choosing Ni supported on MnO catalyst, we decided to use NiO-MnO solid solution catalyst as our target, because within the solid solution, Ni^{2+} homogeneously replaces the position of Mn^{2+} in the unit cells. Therefore the surface Ni^{2+} has low concentration but high dispersion, which is absent in the catalyst of MnO supported Ni. After reduction, the formed Ni^0 will correspondingly be highly dispersed by that Ni^0 particle sintering is suppressed and the stability of the catalyst is ensured. During the synthesis of the catalyst, no matter at which oxidation state the Mn starting material is, during the calcination in the ambient atmosphere, it will be oxidized. However, the SMSI will be actualized by the reduction process where Mn^{x+} ($x > 2$) will be reduced to Mn^{2+} and the surface Ni^{2+} can be reduced to Ni^0 .

Besides of the most crucial property of SMSI between Ni and MnO , there are some more factors making NiO-MnO catalyst extraordinary interesting for investigation:

1. Both Ni and Mn are abundant metals. Low cost materials are always more preferable in industrial application.
2. NiO and MnO have the same NaCl type crystal structure and thereby a solid solution of NiO-MnO could be formed with varying molar ratio of NiO/MnO.¹⁵⁷
3. It has been proven that MnO surfaces show a stronger CO₂ adsorption which accelerates the reverse Boudouard reaction and removes the surface carbon from methane decomposition therefore avoids catalytic deactivation.

Basing on the factors mentioned above, NiO-MnO has been chosen for the candidate catalyst for the DRM reaction. It is desirable to observe an exciting catalytic performance of NiO-MnO promoted by the interaction between the active sites Ni⁰ and MnO for the DRM reaction.

4.2 Bulk $\text{Ni}_x\text{Mn}_{1-x}\text{O}$ solid solution for the DRM reaction

4.2.1 Synthesis and characterization of bulk $\text{Ni}_{0.2}\text{Mn}_{0.8}\text{O}_{\text{cp}}$ catalyst

In order to obtain a direct impression of the catalytic activity of NiMnO catalysts, we select NiMgO as a reference catalyst. Both NiMnO and NiMgO catalysts are synthesized under identical conditions. A bulk $\text{Ni}_{0.2}\text{Mn}_{0.8}\text{O}$ catalyst is synthesized by conventional co-precipitation method. NaHCO_3 is used as the precipitation precursor to obtain a high specific surface area, since metal carbonates release CO_2 during calcination. The later shown BET results indicate that NaHCO_3 indeed gives a high surface area catalyst. For comparison, a $\text{Ni}_{0.2}\text{Mg}_{0.8}\text{O}$ solid solution catalyst is prepared by the same method. The samples prepared by co-precipitation method are named as $\text{Me}_x\text{Me}'_y\text{O}_{\text{cp}}$ (x and y indicate atomic molar fractions of the corresponding metals). The detailed information about the preparation process and the materials before reduction are shown in Appendix A.

Nitrogen adsorption isotherms of $\text{Ni}_{0.2}\text{Mg}_{0.8}\text{O}_{\text{cp}}$ and $\text{Ni}_{0.2}\text{Mn}_{0.8}\text{O}_{\text{cp}}$ are shown in Figure 4.1. It should be mentioned that NiMgO synthesized by co-precipitation reported elsewhere^{75,158} has a surface area of $20 \text{ m}^2/\text{g}$. In contrast, the sample NiMgO obtained from our method shows a much higher surface area of $170 \text{ m}^2/\text{g}$. Both NiMgO and NiMnO show a similar surface area and a meso-size porosity which can be crucial for reactants diffusing to the active sites.

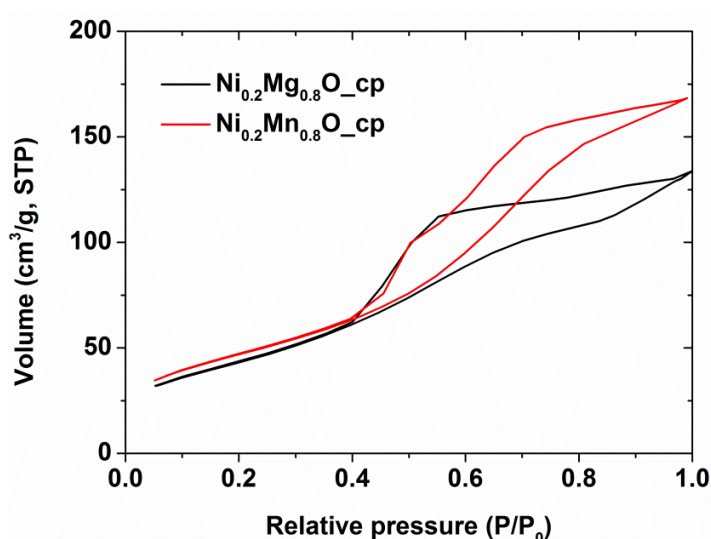


Figure 4.1 N_2 adsorption isotherms of $\text{Ni}_{0.2}\text{Mg}_{0.8}\text{O}_{\text{cp}}$ and $\text{Ni}_{0.2}\text{Mn}_{0.8}\text{O}_{\text{cp}}$.

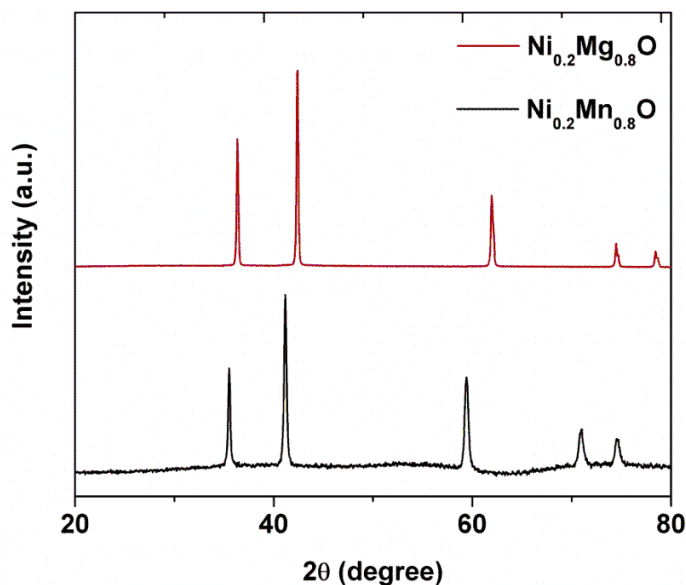


Figure 4.2 The XRD patterns of $\text{Ni}_{0.2}\text{Mn}_{0.8}\text{O}_{\text{cp}}$ and $\text{Ni}_{0.2}\text{Mg}_{0.8}\text{O}_{\text{cp}}$.

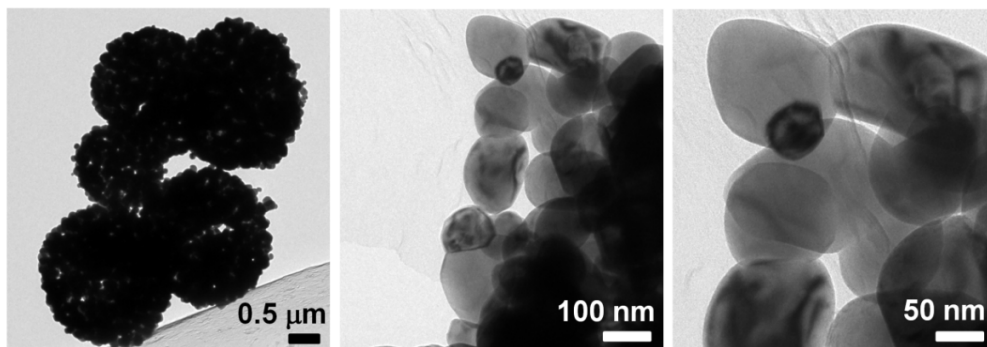


Figure 4.3 TEM images of $\text{Ni}_{0.2}\text{Mn}_{0.8}\text{O}_{\text{cp}}$.

XRD patterns of $\text{Ni}_{0.2}\text{Mn}_{0.8}\text{O}_{\text{cp}}$ and $\text{Ni}_{0.2}\text{Mg}_{0.8}\text{O}_{\text{cp}}$ are presented in Figure 4.2. It shows that both samples are composed of a single phase of $\text{Ni}_{0.2}\text{Mn}_{0.8}\text{O}$ and $\text{Ni}_{0.2}\text{Mg}_{0.8}\text{O}$, respectively. In order to investigate the structure of the materials, TEM images of $\text{Ni}_{0.2}\text{Mn}_{0.8}\text{O}_{\text{cp}}$ are obtained, shown in Figure 4.3. Large spherical aggregates in the range of 1.5–3 μm are observed, which are composed of smaller MONPs with a size of 50–200 nm, with a broad size distribution.

4.2.2 Thermodynamic equilibrium of the DRM reaction under the standard conditions

In order to compare the real performance of the catalysts and obtain detail information about the catalytic deactivation, the saturation of the catalyst usage and the TDE of the reaction should be avoided. Therefore, it is necessary to obtain the data about TDE of the DRM reaction before the catalytic studies. Since most of DRM reactions (except the long term measurements at 675 °C) in this project are investigated with a gas molar ratio of $\text{CH}_4:\text{CO}_2 = 1:1$, the TDE is calculated based on this gas flow. Figure 4.4 shows the TDE conversion of the DRM reaction in the reaction temperature range of 400-800 °C. Considering the cost of energy input, it is more feasible to proceed this reaction at relative low temperature, e.g. at or below 600 °C. When the reaction temperature is too low, the TDE severely limits the conversion of the reactants. Therefore, 550-600 °C will be an optimal reaction temperature from the point of view of industry.

It should be mentioned that in the following presented catalytic results, the conversion of CH_4 is sometimes over the thermodynamic equilibrium limitation. The reason is that the TDE data presented here was calculated without consideration of side reactions. In real reaction conditions, the reverse Boudouard reaction and the reverse WGSR could convert CO_2 and CH_4 to C and H_2O , which shifts the equilibrium and enhance the reaction rate under the TDE.

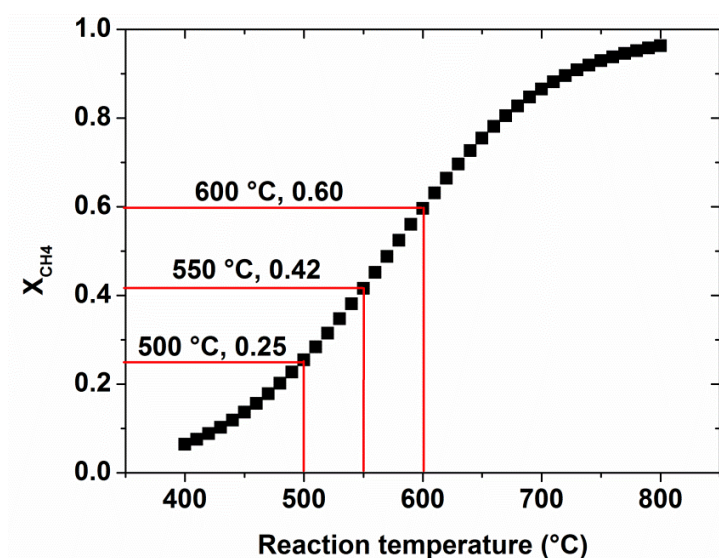


Figure 4.4 Thermodynamically limited conversion of the DRM reaction with the reaction temperature range of 400-800 °C.

4.2.3 Catalytic performance of $\text{Ni}_{0.2}\text{Mn}_{0.8}\text{O}_{\text{cp}}$ in the DRM reaction

The DRM reaction has been studied intensively at high temperature above 650 °C, which is due to the thermodynamic limitation and the poor activity of most of catalysts at lower temperature. Recently Meshcani et al. reported that their best performing catalyst is Ni supported on 0.1% Pt/MgO which gives 38% conversion of CH_4 at 550 °C, with 200 mg catalyst and $15 \text{ L h}^{-1} \text{ g}_{\text{cat}}^{-1}$ GHSV.¹²¹ Another example is mesoporous $\text{La}_2\text{O}_3\text{-ZrO}_2$ supported Ni reported by S. Sokolov et al.⁹⁰ They tested this catalyst at 400 °C, with 100 mg catalyst and $7.2 \text{ L h}^{-1} \text{ g}_{\text{cat}}^{-1}$ GHSV, where 5% of H_2 yield and 8% of CO yield were achieved.

In this project, all catalysts are tested for the DRM reaction in a fixed-bed reactor made of quartz with an inner diameter of 5 mm and a length of 40 mm. In order to verify the activity of the catalyst $\text{Ni}_{0.2}\text{Mn}_{0.8}\text{O}_{\text{cp}}$, the screening experiment of the DRM reaction over both catalysts, $\text{Ni}_{0.2}\text{Mg}_{0.8}\text{O}_{\text{cp}}$ and $\text{Ni}_{0.2}\text{Mn}_{0.8}\text{O}_{\text{cp}}$, respectively, are operated under identical conditions. The experiment starts from 400 °C and ramps to 850 °C, with an increasing rate of 50 °C and each temperature lasting for 0.5 h. Conversion of CH_4 as a function of the reaction temperature is presented in Figure 4.5.

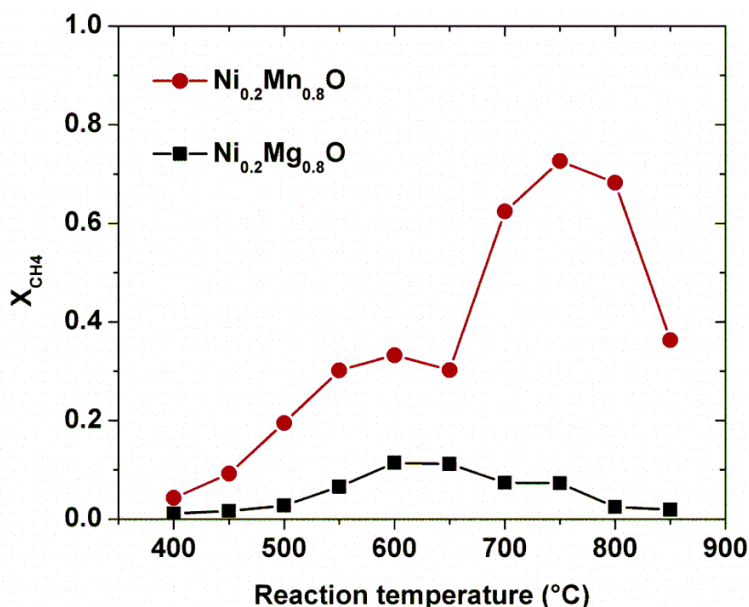


Figure 4.5 Conversion of CH_4 as a function of the reaction temperature for two solid solution catalysts $\text{Ni}_{0.2}\text{Mg}_{0.8}\text{O}_{\text{cp}}$ and $\text{Ni}_{0.2}\text{Mn}_{0.8}\text{O}_{\text{cp}}$, respectively. Reaction conditions: $\text{CH}_4:\text{CO}_2:\text{N}_2:\text{He} = 1:1:0.5:7.5$, $m_{\text{cat}} = 100 \text{ mg}$, $\text{GHSV} = 40 \text{ L h}^{-1} \text{ g}_{\text{cat}}^{-1}$.

It is obvious that $\text{Ni}_{0.2}\text{Mn}_{0.8}\text{O}_{\text{cp}}$ is much more active than $\text{Ni}_{0.2}\text{Mg}_{0.8}\text{O}_{\text{cp}}$ over the whole temperature range. The former one has been activated since the beginning of the experiment at 400 °C and the activity is strongly growing with increasing reaction temperature, especially between 650-700 °C. Over the catalyst $\text{Ni}_{0.2}\text{Mn}_{0.8}\text{O}$, TDE of the DRM reaction is fully achieved under these mild conditions. In contrast, $\text{Ni}_{0.2}\text{Mg}_{0.8}\text{O}_{\text{cp}}$ requires higher temperature for activation and the catalyst starts reactant conversion at 500 °C. The activity increases slowly with the increasing reaction temperature and achieves the maximum at 600 °C. After 5 hours reaction at 850 °C, $\text{Ni}_{0.2}\text{Mg}_{0.8}\text{O}_{\text{cp}}$ shows no more activity. Both catalysts suffer from deactivation at higher reaction temperature.

4.2.4 What makes $\text{Ni}_{0.2}\text{Mn}_{0.8}\text{O}_{\text{cp}}$ so active for the DRM reaction?

The screening results presented above show that $\text{Ni}_{0.2}\text{Mn}_{0.8}\text{O}_{\text{cp}}$ is much more active than $\text{Ni}_{0.2}\text{Mg}_{0.8}\text{O}_{\text{cp}}$. In order to obtain a quantitative impression, $\text{Ni}_{0.2}\text{Mn}_{0.8}\text{O}_{\text{cp}}$ is compared with all reported DRM catalysts tested below 600 °C.^{89,90,121}

Table 2 The activity of some Ni-based catalysts in the DRM reaction below 600 °C.

catalyst	T_R (°C)	GHSV ($\text{L h}^{-1}\text{g}_{\text{cat}}^{-1}$)	m_{cat} (mg)	X_{CH_4} (%)
$\text{Ni}_{0.2}\text{Mn}_{0.8}\text{O}_{\text{cp}}$	550	80	50	30
Ni/MgO/0.1% Pt ¹²¹	550	15	200	30-38
Ni/ZrO ₂ ⁸⁹	500	15	200	10
Ni/La ₂ O ₃ /ZrO ₂ ⁹⁰	400	7.2	100	5% H ₂ 8% CO

Interestingly, $\text{Ni}_{0.2}\text{Mn}_{0.8}\text{O}_{\text{cp}}$ shows higher activity than any other Ni-based catalysts, including Pt doped NiMgO solid solution. Considering the impressively high activity, one would ask, why is $\text{Ni}_{0.2}\text{Mn}_{0.8}\text{O}_{\text{cp}}$ so active in the DRM reaction? What decides or affects the activity of this catalyst?

$\text{Ni}_{0.2}\text{Mn}_{0.8}\text{O}_{\text{cp}}$ and $\text{Ni}_{0.2}\text{Mg}_{0.8}\text{O}_{\text{cp}}$ are prepared under identical conditions, with the same atomic ratio of Ni/Mn or Ni/Mg as 1/4, and with very similar surface area of 150-170 m^2/g . BET isotherms of these 2 catalysts are shown in Figure 4.1. The XRD patterns in Figure 4.2 indicate that both catalysts form a solid solution before being applied to the DRM reaction. The most probable answer for the much higher activity of NiMnO catalyst is SMSI between Ni and MnO, which is absent between Ni and MgO. Due to SMSI, the NiMnO catalyst possesses special properties such as suppressed adsorption of CO and H_2 , significant enhancement of the boundary surface, which makes it more active for the DRM reaction.

For a Ni catalyst, the active sites are atomic Ni^0 or Ni^0 clusters. Therefore, besides of the strong influence of the support, the concentration of surface Ni atoms which decides the size of reduced Ni^0 particles is another crucial factor: high concentrations cause Ni clusters agglomeration, therefore resulting catalytic deactivation. Low concentrations can avoid Ni clusters agglomeration but cause sparse active sites resulting in low activity. Conclusively a suitable concentration of surface Ni atoms is important for synthesizing a highly active catalyst. Figure 4.6 illustrates possible factors influencing the activity of a Ni catalyst in the DRM reaction. Essentially, the dispersion and stability of surface Ni^0 atoms/clusters decide the catalytic performance of a Ni catalyst. Therefore, the factors or conditions influencing the formation of Ni^0 active sites become especially important. Taking NiMnO catalyst as the example, the most important factors can be:

1. The interactions between reduced Ni and the support MnO help to stabilize Ni^0 on the surface of MnO. Moreover, the strength between Ni^{2+} and the unit cells has significant impact on Ni^{2+} diffusion, which strongly affects the concentration of surface Ni.
2. The concentration of Ni loading in the catalyst has a direct impact on the formation of active sites Ni^0 . Ni cluster sintering/agglomeration can be suppressed by decreasing the concentration of Ni therefore stability of the catalyst is enhanced.

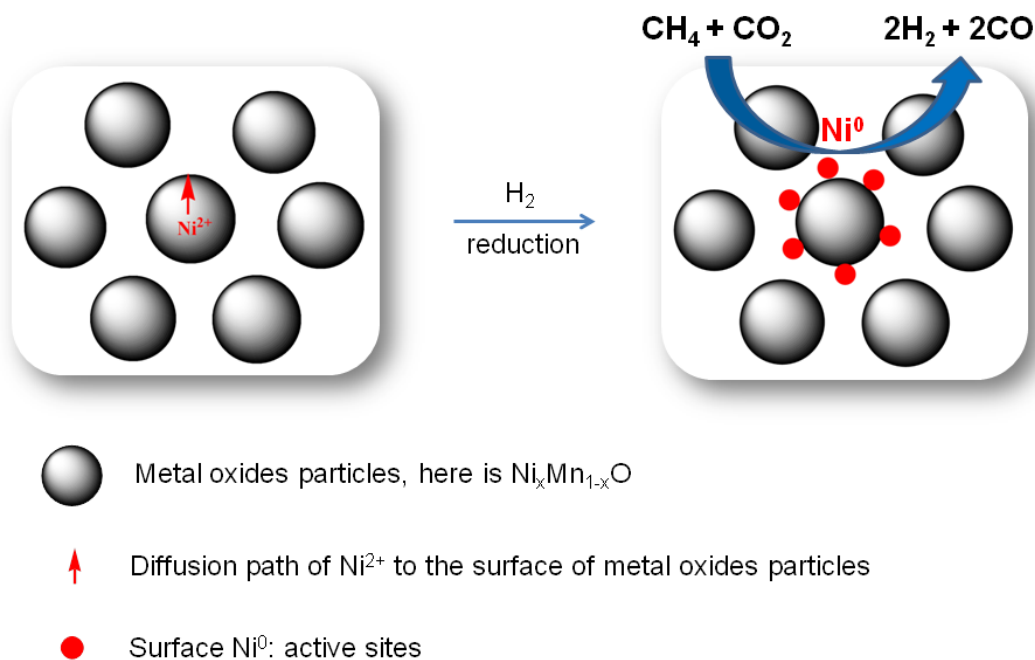


Figure 4.6 Illustration of possible factors which influence the activity of a Ni catalyst in the DRM reaction.

3. The size of MONPs decides the diffusion path of Ni^{2+} to the surface. Smaller MOs give shorter diffusion paths and contribute to faster Ni^0 formation therefore bring higher activity.
4. It has also been reported that the catalyst with very low Ni loading requires high reduction temperature and long reduction time to form a surface Ni^0 .

4.2.5 Influence of Ni loading on the activity of NiMnO catalyst

As discussed above, a suitable Ni concentration in the catalyst is the most direct factor to control the formation of surface Ni^0 . In order to find the suitable concentration, a series of $\text{Ni}_x\text{Mn}_{1-x}\text{O}_{\text{cp}}$ samples ($\text{Ni}_{0.05}\text{Mn}_{0.95}\text{O}$, $\text{Ni}_{0.1}\text{Mn}_{0.9}\text{O}$, $\text{Ni}_{0.2}\text{Mn}_{0.8}\text{O}$ and $\text{Ni}_{0.5}\text{Mn}_{0.5}\text{O}$) are prepared by co-precipitation with identical procedure. (The screening results shown here were provided by Patrick Littlewood)

Figure 4.7A is the screening results of the DRM reaction over the catalysts $\text{Ni}_{0.05}\text{Mn}_{0.95}\text{O}$, $\text{Ni}_{0.1}\text{Mn}_{0.9}\text{O}$, $\text{Ni}_{0.2}\text{Mn}_{0.8}\text{O}$ and $\text{Ni}_{0.5}\text{Mn}_{0.5}\text{O}$ prepared by co-precipitation methods. For all catalysts,

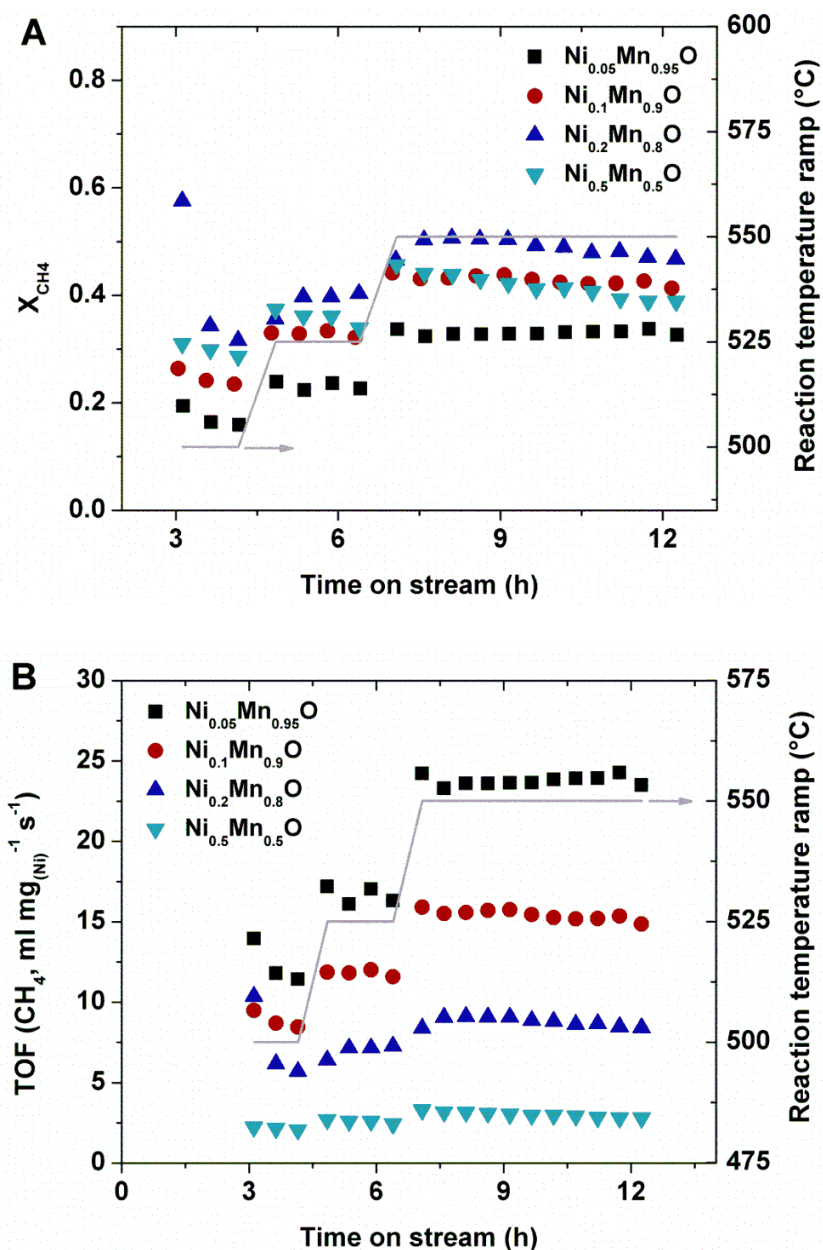


Figure 4.7 Screening experiments over $Ni_{0.05}Mn_{0.95}O_{cp}$, $Ni_{0.1}Mn_{0.9}O_{cp}$, $Ni_{0.2}Mn_{0.8}O_{cp}$ and $Ni_{0.5}Mn_{0.5}O_{cp}$ catalysts. Reaction temperature 500-550 $^{\circ}C$, feed gas $CH_4:CO_2:He = 1:1:8$, $m_{cat} = 50\ mg$, GHSV = 80 $L\ h^{-1}\ g^{-1}$.

the activity increases as ramping up the reaction temperature. Except $Ni_{0.5}Mn_{0.5}O$, the other catalysts show an increasing activity at a higher Ni loading from Ni(0.05) to Ni(0.2). At 500 $^{\circ}C$, all catalysts show deactivation, which is most probably due to the surface carbon deposition caused by CH_4 decomposition. The later occurring higher stability at higher reaction temperature

indicates the removal of surface carbon by the reverse Boudouard reaction; at 525 and 550 °C, $\text{Ni}_{0.05}\text{Mn}_{0.95}\text{O}$ and $\text{Ni}_{0.1}\text{Mn}_{0.9}\text{O}$ are stable however $\text{Ni}_{0.2}\text{Mn}_{0.8}\text{O}$ and $\text{Ni}_{0.5}\text{Mn}_{0.5}\text{O}$ show deactivation, especially at 550 °C. It is noticeable that the enhancement of CH_4 conversion from $\text{Ni}_{0.05}\text{Mn}_{0.95}\text{O}$ to $\text{Ni}_{0.1}\text{Mn}_{0.9}\text{O}$ is higher than that from $\text{Ni}_{0.1}\text{Mn}_{0.9}\text{O}$ to $\text{Ni}_{0.2}\text{Mn}_{0.8}\text{O}$. From the catalytic performance of $\text{Ni}_x\text{Mn}_{1-x}\text{O}$, one can conclude that $\text{Ni}_{0.1}\text{Mn}_{0.9}\text{O}$ is the optimal catalyst due to its good stability as well as activity.

In order to obtain a direct impression of the activity of $\text{Ni}_x\text{Mn}_{1-x}\text{O}_{\text{cp}}$ samples series, the turn over frequency (TOF) of CH_4 as a function of time on steam is presented as Figure 4.7B. It is assumed that all Ni atoms are identical active sites and the TOF of CH_4 is calculated per mg of Ni. It is not surprising that $\text{Ni}_{0.5}\text{Mn}_{0.5}\text{O}_{\text{cp}}$ has the lowest TOF and the TOF increases with decreasing Ni loading, since the catalyst with higher Ni loading has higher concentration of surface Ni and a more severe Ni particle sintering problem. This significantly decreases the number of active sites and causes lower TOF.

4.2.6 Stability study of bulk $\text{Ni}_{0.2}\text{Mn}_{0.8}\text{O}_{\text{cp}}$ catalyst

Generally, carbon deposition by the Boudouard reaction (eq.10) is favoured at low temperatures and low amounts of CO_2 . In order to minimize this effect, the fraction of carbon dioxide is raised to 0.67 and reaction temperature is increased to 675 °C. Based on thermodynamic calculations using values from the NIST database,¹⁵⁹ under these conditions, surface carbon deposition is less favourable. A long term measurement (LTM) is performed at 675 °C with the catalyst $\text{Ni}_{0.2}\text{Mn}_{0.8}\text{O}_{\text{cp}}$, presented in Figure 4.8.

Since N_2 is excluded from the molar fraction calculation, ideally, before any reaction starts the molar fraction of CO_2 and CH_4 should be 0.83 and 0.17, respectively, with zero yields of CO , H_2 and H_2O . In Figure 4.8, the first point of all components (especially in case of CO_2 , CO and H_2O) at the beginning of this experiment is discrete from others, which is also observed in other experiments. The first points of molar fraction reveal a complete consumption of CH_4 , little or no conversion of CO_2 , a low yield of CO and a high yield of H_2 and H_2O . Based on this information one can certainly assume that the dry reforming reaction over $\text{Ni}_{0.2}\text{Mn}_{0.8}\text{O}_{\text{cp}}$ catalyst starts from CH_4 decomposition reaction, described by eq. 9, and CO_2 is mainly reduced by H_2 (RWGS, eq. 8)

instead of surface carbon (the Boudouard reaction, eq.10). The rate of CH_4 decomposition reaction is obviously much higher than that of the Boudouard reaction.

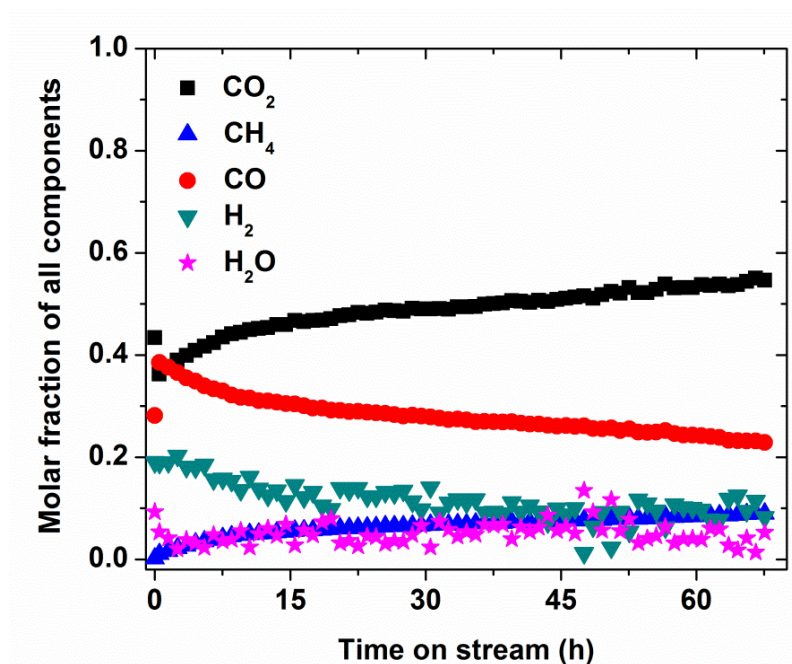


Figure 4.8 A LTM over $\text{Ni}_{0.2}\text{Mn}_{0.8}\text{O}_{\text{cp}}$ in the DRM reaction. Molar fraction of all components as a function of time on stream. ($m_{\text{cat}} = 64.4 \text{ mg}$, reaction temperature 675°C , GHSV = $47 \text{ L h}^{-1} \text{ g}^{-1}$, feed gas $\text{CH}_4:\text{CO}_2:\text{N}_2 = 1:5:1.5$. Note that N_2 is excluded from molar fraction calculation.)

From the 2nd point of molar fractions, there is a strong decrease of CO_2 fraction and an increase of CO fraction, meaning a high conversion of CO_2 and high yield of CO . By comparison, the fraction of CH_4 and H_2 are nearly unchanged. However, the fraction of H_2O decreases greatly. It is not difficult to conclude that the rate of the Boudouard reaction largely increases and thereby the surface carbon produced by CH_4 decomposition is quickly removed.

During the first 13 hours, the catalyst shows severe deactivation. It could be caused by the coverage of the active sites by deposited carbon; it could be also resulted from structural change of the catalyst, such as pore collapsing and phase transition. After 70 h measurement, the activity elapsing of the catalyst tends towards stability. It is imaginable that as time of the reaction, a

steady state could be achieved where the rates of eq. 9 and eq. 10 are equal, and the structure of the catalyst become stable.

In order to distinguish between the reasons of the deactivation by either coke formation or particle sintering/ Ni^0 agglomeration, a reoxidation procedure is established. In case of the deactivation caused by coke formation, a reoxidation can remove the deposited carbon completely and recover the original activity of the catalyst. If the deactivation is caused by particle sintering or agglomeration, the process of reoxidation will not help to recover the lost activity. The reoxidation experiment is processed as follows: after the LTM (70 h reaction at 675 °), the catalyst is treated by oxidation under air flow to remove the possible deposited carbon and subsequent reduction under H_2 flow for the new application to the DRM reaction. The reoxidation experiments are repeated in 3 runs, 1st and 2nd run with 1 h oxidation and 3rd run with 2 h oxidation time.

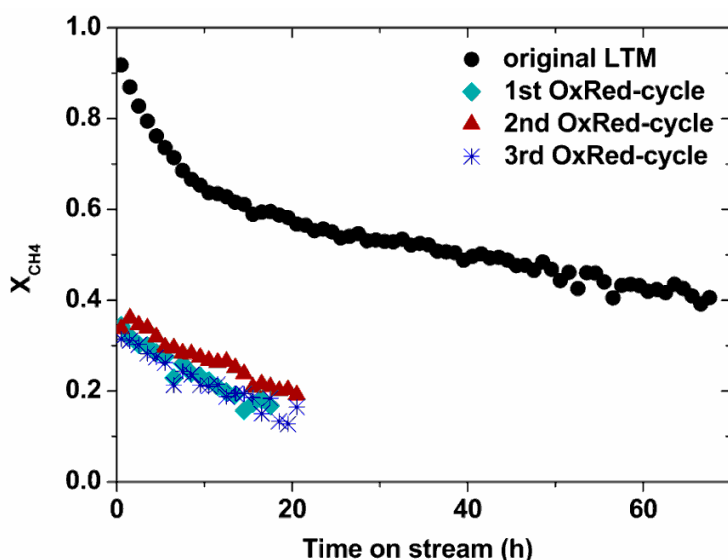


Figure 4.9 Reoxidation experiments of $\text{Ni}_{0.2}\text{Mn}_{0.8}\text{O}_{\text{cp}}$ in the DRM reaction. Conversion of methane as a function of time on stream. ($m_{\text{cat}} = 64.4$ mg, reaction temperature 675 °C, GHSV = $47 \text{ L h}^{-1} \text{ g}^{-1}$, feed gas $\text{CH}_4:\text{CO}_2:\text{N}_2 = 1:5:1.5$)

After the reoxidation experiments, shown in Figure 4.9, the conversion of CH_4 starts at a much lower level compared to that of the original LTM, so one can infer that the main reason of the

deactivation that occurred during the LTM must be agglomeration of Ni^0 clusters to larger Ni^0 NPs. Therefore the activity is unable to be reestablished by the subsequent reoxidation. Carbon deposition can be accompanied as a minor factor. During the reoxidation recycling, the catalyst shows very similar catalytic behavior and the activity of the catalyst is able to be reestablished after the reoxidation treatment, which strongly indicates that the deactivation occurred during reoxidation recycling should be caused by carbon deposition. Furthermore, the same conversion of CH_4 in the beginning of each run indicates that the carbon coverage is removed completely.

Based on the information from the LTM and reoxidation experiments, one can conclude that during catalytic application, particle sintering is the dominant reason for the catalyst deactivation, which is more pronounced in the beginning of the reaction and causes an exponential decay of the activity; in comparison, carbon deposition is a minor factor for the catalyst deactivation, leading to a slower and linear deactivation with reaction time.

XRD patterns and TEM images of $\text{Ni}_{0.2}\text{Mn}_{0.8}\text{O}_{\text{cp}}$ after the LTM are obtained. In Figure 4.10, the XRD patterns reveals an increase of crystallite size after the reaction (as shown in Table 3, page 61), which indicates particle ripening or sintering during the DRM reaction.

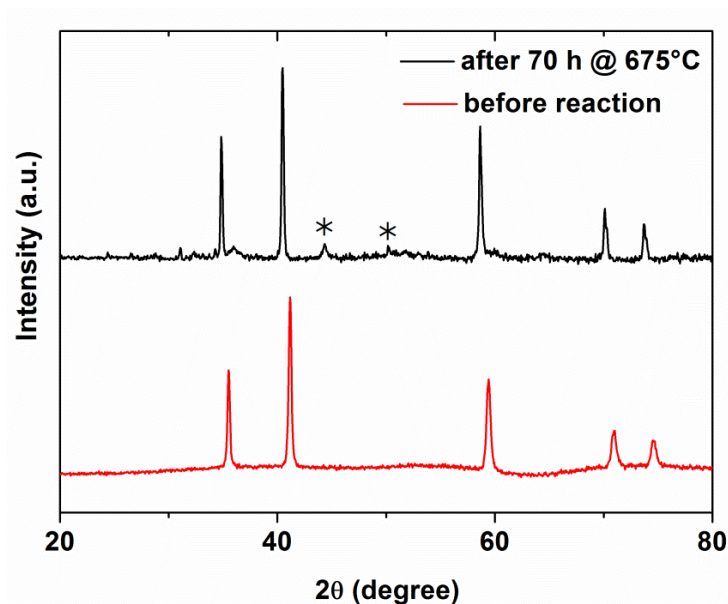


Figure 4.10 XRD of $\text{Ni}_{0.2}\text{Mn}_{0.8}\text{O}_{\text{cp}}$ before and after the LTM at 675 °C for 60 h. (* noted as the phase of Ni^0)

Furthermore, the characteristic peaks from $\text{Ni}_{0.2}\text{Mn}_{0.8}\text{O}_{\text{cp}}$ are shifted to lower 2θ after the reaction, which indicates lower concentration of NiO in the solid solution. The missing Ni^{2+} diffused to the surface and was reduced to Ni^0 . The occurrence of a new phase of Ni^0 (noted from the two small peaks at 2θ 44° and 52°) can confirm it. Since metallic Ni^0 is the active site for the DRM reaction, one could imagine that the agglomeration of metallic Ni to Ni^0 NPs is one of the main reasons for the catalyst deactivation.

TEM images revealed a severe particle sintering during the DRM reaction, shown in Figure 4.11, consistent with the information from the XRD patterns.

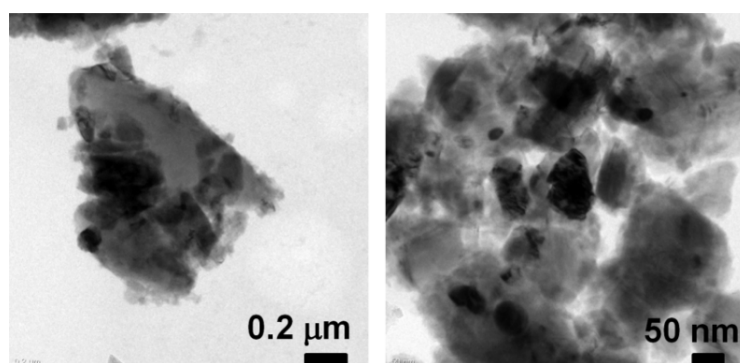


Figure 4.11 TEM images of $\text{Ni}_{0.2}\text{Mn}_{0.8}\text{O}_{\text{cp}}$ after the LTM at 675 °C for 60 h.

4.3 NiMnO nanocrystallites supported on porous silica for the DRM reaction

As discussed in part 4.2, the solid solution $\text{Ni}_{0.2}\text{Mn}_{0.8}\text{O}_{\text{cp}}$ is highly active over the DRM reaction and this catalyst already exhibits activity since the beginning of the reaction at 400 °C. On the other hand, the catalyst shows deactivation after several hours of reaction. The most important issue is to avoid the deactivation while the high activity remains. From the view of microstructure, the catalyst should have the following characters: relative low Ni^{2+} concentration but fast Ni^{2+} diffusion. Fast Ni^{2+} diffusion ensures an easy formation of surface Ni^0 therefore provide a high activity; low Ni^{2+} concentration forming smaller Ni^0 clusters with high dispersed species can avoid the agglomerations of Ni^0 clusters and therefore the catalyst deactivation. In this chapter, it will be discussed in detail how to fulfill the goal by a nanocrystallite catalyst NiMnO with additional SiO_2 support material by a combined preparation method of co-precipitation and sol-gel process.

4.3.1 Advantages of silica as catalyst support

Among the catalysts for the DRM reaction, there are various oxides which are used as support, such as SiO_2 , CaO , MgO , Al_2O_3 , CeO_2 , TiO_2 , La_2O_3 and ZrO_2 etc. Basically those supports are separated as two types: acidic and basic supports.

The support material plays an important role in the reaction. It influences the adsorption of both reactants and products. For example, CH_4 has much stronger adsorption on acidic supports; on the other side, CO_2 shows stronger adsorption on basic supports so that surface carbonate species can be formed which removes deposited carbon from the catalyst surface. Therefore it is assumed that basic supports can inhibit carbon deposition. Besides, when the support interacts with the metal, it can significantly affect the catalytic properties of the catalyst. A strong interaction between the support and metal makes the catalyst more resistant against sintering and coking, but also less active.

In this project, we choose SiO_2 instead of basic metal oxides as the support, because certainly no metal-metal interaction exists between silica and the catalyst. Therefore, it is expected to see that

the addition of silica shows no disturbance to the formation of the solid solution of NiMnO. When a metal oxide with different crystal structure from NiO/MnO is used as the support, the formation of the solid solution NiMnO can be disturbed. As a catalyst, NiMnO solid solution is highly active in the DRM reaction. Our goal is not to study the effect of different supports to the catalyst. Instead, we are interested in the optimization of catalytic properties of NiMnO by decreasing the size and increasing the surface area of NiMnO NPs.

4.3.2 Synthesis and characterization of $\text{Ni}_{0.2}\text{Mn}_{0.8}\text{O}/\text{SiO}_2$ nanocrystallites

From the results presented in Chapter 4.2.5, among the series of bulk catalysts $\text{Ni}_x\text{Mn}_{1-x}\text{O}$ with different Ni loading, $\text{Ni}_{0.1}\text{Mn}_{0.9}\text{O}$ exhibits best catalytic performance with good stability as well as high activity. In case of silica supported NiMnO catalyst, considering the addition of silica (equal molar amount as metal oxides), we choose $\text{Ni}_{0.2}\text{Mn}_{0.8}\text{O}/\text{SiO}_2$ as a standard catalyst to ensure the same overall Ni loading as the bulk catalyst $\text{Ni}_{0.1}\text{Mn}_{0.9}\text{O}$.

A NiMnO/SiO₂ catalyst, named $\text{Ni}_{0.2}\text{Mn}_{0.8}\text{O_cp-SiO}_2$, is prepared using a combination of co-precipitation with a sol-gel process forming the silica phase. Sodium silicate Na_2SiO_3 , also named as water glass, is chosen as the silica precursor. It is worth to mention that this chemical is very cheap with the price of 25 EURO for a 5 kg pack.

During the synthesis, first a Na_2SiO_3 solution is mixed with the precipitation precursor NaHCO_3 . In order to obtain suitable gelation kinetics of Na_2SiO_3 , a certain amount of HCl solution is added to the mixture until the pH decreases to ~ 10 , where Na_2SiO_3 starts gelating. Subsequently the metal salt precursors are added to the mixture drop wise. Due to the dispersion of NaHCO_3 in the gel and also the drop wise addition of metal salt precursors, NiCO_3 and MnCO_3 precipitate slowly and therefore highly disperse in the silica gel formed meanwhile. This one-pot approach is practical for industrial catalysts synthesis due to its large scalability, ease and simplicity without any tedious or time consuming processes. With this new method, $\text{Ni}_x\text{Mn}_{1-x}\text{O}$ nanocrystallites dispersed on porous silica can be obtained. The following detailed characterization and catalytic information will show the benefits of the catalyst obtained from this one-pot approach.

The samples prepared by co-precipitation method are named $\text{Me}_x\text{Me}'_y\text{O}_{\text{cp}}\text{-SiO}_2$. X and y indicate the molar fraction of the corresponding metal. Without any additional note, the molar ratio of metal oxides to silica is 1. The detail preparation process is shown in Chapter 3.1.2.

In order to investigate the influence of silica on the dispersion of the NiMnO catalyst, $\text{Ni}_{0.2}\text{Mn}_{0.8}\text{O}_{\text{cp}}\text{-SiO}_2$ is compared with $\text{Ni}_{0.2}\text{Mn}_{0.8}\text{O}_{\text{cp}}$ at each state. In Figure 4.12, H_2 -TPR profiles of the as synthesized materials (before reduction), $\text{Ni}_{0.2}\text{Mn}_{0.8}\text{O}_{\text{cp}}\text{-SiO}_2$ and $\text{Ni}_{0.2}\text{Mn}_{0.8}\text{O}_{\text{cp}}$, show two dominant peaks in temperature ranges between 200-250 °C and 300-350 °C, respectively, which is probably attributed to the reduction sequence from MnO_2 to Mn_3O_4 and finally to MnO . First of all, one can realize that the area of each peak from the sample $\text{Ni}_{0.2}\text{Mn}_{0.8}\text{O}_{\text{cp}}\text{-SiO}_2$ is much smaller than that from $\text{Ni}_{0.2}\text{Mn}_{0.8}\text{O}_{\text{cp}}$, which is caused by the lower content of manganese oxide due to the dilution by SiO_2 . Secondly, compared to $\text{Ni}_{0.2}\text{Mn}_{0.8}\text{O}_{\text{cp}}$, H_2 -TPR profile of $\text{Ni}_{0.2}\text{Mn}_{0.8}\text{O}_{\text{cp}}\text{-SiO}_2$ is shifted to lower temperature, which indicates that MnO_2 can easier be reduced to MnO and therefore easier form a solid solution of NiMnO. By that it could be inferred that $\text{Ni}_{0.2}\text{Mn}_{0.8}\text{O}_{\text{cp}}\text{-SiO}_2$ can be activated at lower reaction temperature.

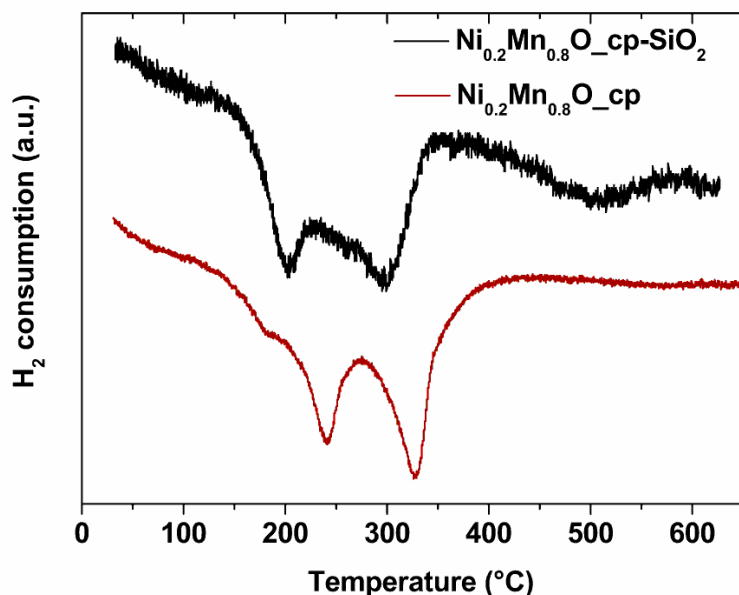


Figure 4.12 H_2 -TPR profiles of $\text{Ni}_{0.2}\text{Mn}_{0.8}\text{O}_{\text{cp}}\text{-SiO}_2$ and $\text{Ni}_{0.2}\text{Mn}_{0.8}\text{O}_{\text{cp}}$ before reduction.

The samples $\text{Ni}_{0.2}\text{Mn}_{0.8}\text{O}_{\text{cp}}\text{-SiO}_2$ and $\text{Ni}_{0.2}\text{Mn}_{0.8}\text{O}_{\text{cp}}$ before reduction are additionally determined by XRD. The XRD patterns are presented in Figure IV (Appendix A, page 110). Before reduction both samples are composed of mixed phases of MnO_2 and NiMnO_3 . This confirms the assumption from the TPR experiments that the two dominant peaks are attributed to the reduction from MnO_2 to Mn_2O_3 and from Mn_2O_3 to MnO , separately.

In all XRD patterns of $\text{Ni}_x\text{Mn}_{1-x}\text{O}_{\text{cp}}\text{-SiO}_2$ samples, a broad peak at $2\theta \sim 22^\circ$ is noted as the characteristic peak from silica. It must be noted that in case of all silica supported samples, the silica peak at $2\theta \sim 22^\circ$ is excluded by baseline subtraction, to obtain a clear and high resolution XRD patterns. The XRD patterns of the catalysts are presented in Figure 4.13.

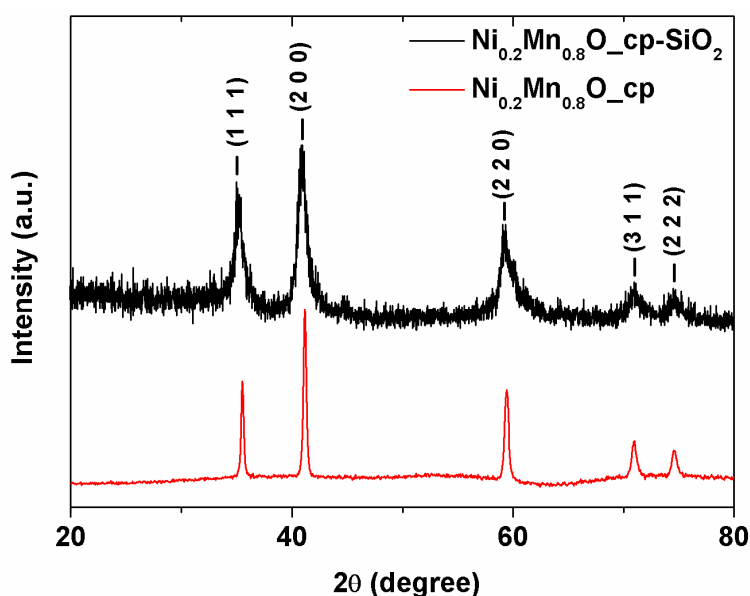


Figure 4.13 XRD patterns of $\text{Ni}_{0.2}\text{Mn}_{0.8}\text{O}_{\text{cp}}\text{-SiO}_2$ and $\text{Ni}_{0.2}\text{Mn}_{0.8}\text{O}_{\text{cp}}$.

It can be seen that a solid solution of $\text{Ni}_x\text{Mn}_{1-x}\text{O}$ is formed in both cases. A metal ratio corresponding to $x = 0.2$ reflects the initial molar ratio of the metals used in the synthesis. This ratio is also found in the final oxide by ICP measurements (see Table 3). The similar peak positions in both patterns furthermore show that the simultaneous formation of an amorphous silica phase in $\text{Ni}_{0.2}\text{Mn}_{0.8}\text{O}_{\text{cp}}\text{-SiO}_2$ indeed does not influence the crystal structure formation or composition of the ternary oxide. However, compared to $\text{Ni}_{0.2}\text{Mn}_{0.8}\text{O}_{\text{cp}}$, the pattern of

Ni_{0.2}Mn_{0.8}O_cp-SiO₂ shows much broader peaks indicating the formation of smaller crystallites. Applying the Scherrer formula, an average crystallite size of around 30 nm is found for the bulk oxides, while this is greatly reduced to around 10 nm for the supported oxides (Table 2). Also an increased surface area of 221 m²/g is found for Ni_{0.2}Mn_{0.8}O_cp-SiO₂ by nitrogen sorption measurements. This noticeable increase of the surface area is not only due to the smaller particle size of the metal oxide, but it can be assumed that also the silica phase had a large contribution.

Table 3 Summary of the structural properties of the catalysts.

Sample name	Preparation method ^a	S _{BET} (m ² /g)	Crystal size ^b (nm)		ICP Ni % ^e	C _{deposited} w.t.% ^f
			B.R. ^c	A.R. ^d		
Ni _{0.2} Mg _{0.8} O_cp	cp	170	---	---	0.200	---
Ni _{0.2} Mn _{0.8} O_cp	cp	158	24.5/ 33.2	35.0/35.6	0.201	2.38
Ni _{0.2} Mn _{0.8} O_cp-SiO ₂	cp-SiO ₂	221	10.5/ 8.5	21.2/19.2	0.200	3.54 /0.21

^a cp: co-precipitation; cp-SiO₂: co-precipitation combined with a sol-gel process of Na₂SiO₃·5H₂O.

^b The crystal size is derived from the Scherrer equation using the (1 1 1) and (2 0 0) peaks of the diffractogramm.

^c B.R.: before the catalytic reaction

^d A.R.: after 40 h at 525 °C in the DRM reaction.

^e molar fraction of Ni/(Mn+Ni).

^f the results of carbon deposition is obtained by elemental analysis. Ni_{0.2}Mn_{0.8}O_cp is tested after the reaction at 525 °C for 40 h; Ni_{0.2}Mn_{0.8}O_cp-SiO₂ is tested after the reaction at 525 °C for 40 h and at 500°C for 60 h separately.

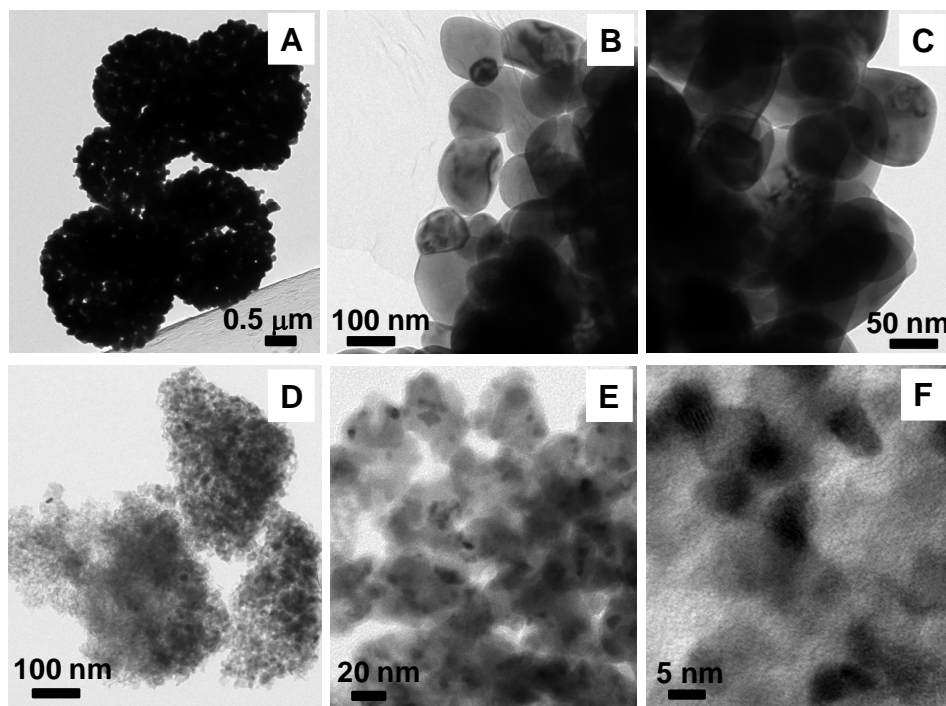


Figure 4.14 TEM images of $\text{Ni}_{0.2}\text{Mn}_{0.8}\text{O}_{\text{cp}}$ (A-C) and $\text{Ni}_{0.2}\text{Mn}_{0.8}\text{O}_{\text{cp}}\text{-SiO}_2$ (D-F).

In order to further investigate the structure of the materials, TEM images of $\text{Ni}_{0.2}\text{Mn}_{0.8}\text{O}_{\text{cp}}$ and $\text{Ni}_{0.2}\text{Mn}_{0.8}\text{O}_{\text{cp}}\text{-SiO}_2$ are shown in Figure 4.14. Figure 4.14 A-C show the sample $\text{Ni}_{0.2}\text{Mn}_{0.8}\text{O}_{\text{cp}}$ obtained from co-precipitation. Large spherical aggregates in the range of 1.5-3 μm are observed, which are composed of smaller metal oxide particles with a size of approx. 100 nm, however with a broad size distribution. In contrast, for $\text{Ni}_{0.2}\text{Mn}_{0.8}\text{O}_{\text{cp}}\text{-SiO}_2$ (D-F) no large metal oxide aggregates can be seen. Instead, MONPs with a diameter of 6-10 nm are observed, which are dispersed on the amorphous silica support. The addition of the silica phase indeed efficiently suppresses the agglomeration and improves the dispersion of MONPs. The approach shown here therefore provides a simple and feasible pathway for the one pot synthesis of supported MONPs, even with mixed metal compositions.

4.3.3 Catalytic performance of $\text{Ni}_{0.2}\text{Mn}_{0.8}\text{O}/\text{SiO}_2$ in the DRM reaction

The nanocrystalline catalyst of $\text{Ni}_{0.2}\text{Mn}_{0.8}\text{O}$ supported on silica is applied for the DRM reaction. It is desired to find out, if and how the additional presence of the silica support and the structure

variation introduced by the here discussed one-pot approach (co-precipitation combined with sol-gel process) influences the catalytic performance of $\text{Ni}_{0.2}\text{Mn}_{0.8}\text{O}$. Therefore, the supported catalyst $\text{Ni}_{0.2}\text{Mn}_{0.8}\text{O_cp-SiO}_2$ is compared to the bulk catalyst $\text{Ni}_{0.2}\text{Mn}_{0.8}\text{O_cp}$ during the following catalytic applications. In order to enable such a comparison, $\text{Ni}_{0.2}\text{Mn}_{0.8}\text{O_cp}$ and $\text{Ni}_{0.2}\text{Mn}_{0.8}\text{O_cp-SiO}_2$ are tested for the DRM reaction under identical conditions.

4.3.3.1 Activity study

Figure 4.15 is a screening experiment over catalysts $\text{Ni}_{0.2}\text{Mn}_{0.8}\text{O_cp}$ and $\text{Ni}_{0.2}\text{Mn}_{0.8}\text{O_cp-SiO}_2$ at low reaction temperature range between 500-550 °C. Obviously the catalyst $\text{Ni}_{0.2}\text{Mn}_{0.8}\text{O_cp-SiO}_2$ shows a much higher activity than $\text{Ni}_{0.2}\text{Mn}_{0.8}\text{O_cp}$ during the whole reaction. At 550 °C, with the catalyst $\text{Ni}_{0.2}\text{Mn}_{0.8}\text{O_cp-SiO}_2$, methane conversion is still over 30% after 17 h reaction time on stream. Despite of high activity, one has to admit that the deactivation is also pronounced for both bulk and nanocrystalline catalysts.

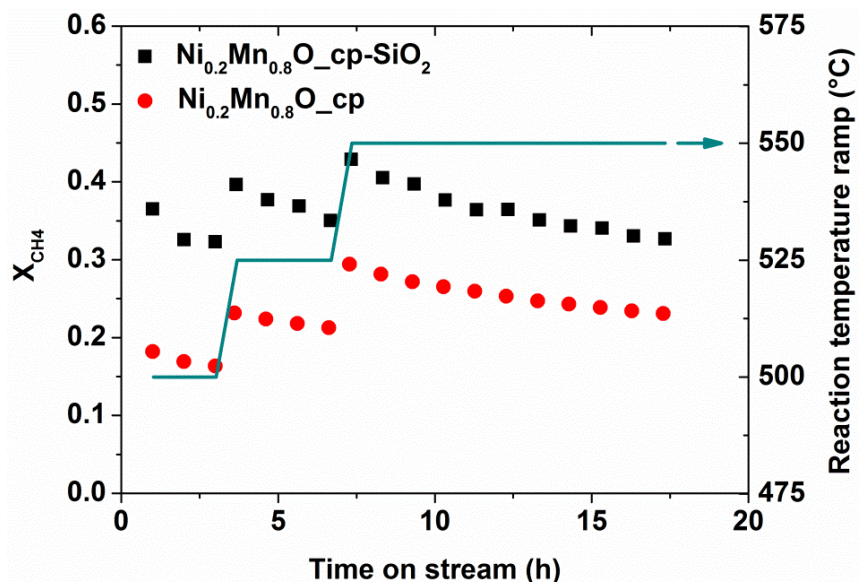


Figure 4.15 Methane conversion as a function of time on stream over $\text{Ni}_{0.2}\text{Mn}_{0.8}\text{O_cp}$ and $\text{Ni}_{0.2}\text{Mn}_{0.8}\text{O_cp-SiO}_2$ catalysts. Feed gas $\text{CH}_4:\text{CO}_2:\text{N}_2:\text{He} = 1:1:0.5:0.75$, for $\text{Ni}_{0.2}\text{Mn}_{0.8}\text{O_cp}$, $m_{\text{cat}} = 50$ mg, GHSV = $80 \text{ L h}^{-1} \text{ g}^{-1}$; for $\text{Ni}_{0.2}\text{Mn}_{0.8}\text{O_cp-SiO}_2$, $m_{\text{cat}} = 100$ mg, GHSV = $40 \text{ L h}^{-1} \text{ g}^{-1}$. The net mass of Ni is 7 mg for both catalysts.

4.3.3.2 Long term stability at 525 °C

In order to obtain more detailed information about the catalyst deactivation and consequently to improve the catalyst by tuning and modifying the structure, some long term experiments are carried out with the nanocrystalline catalyst $\text{Ni}_{0.2}\text{Mn}_{0.8}\text{O}_{\text{cp}}\text{-SiO}_2$.

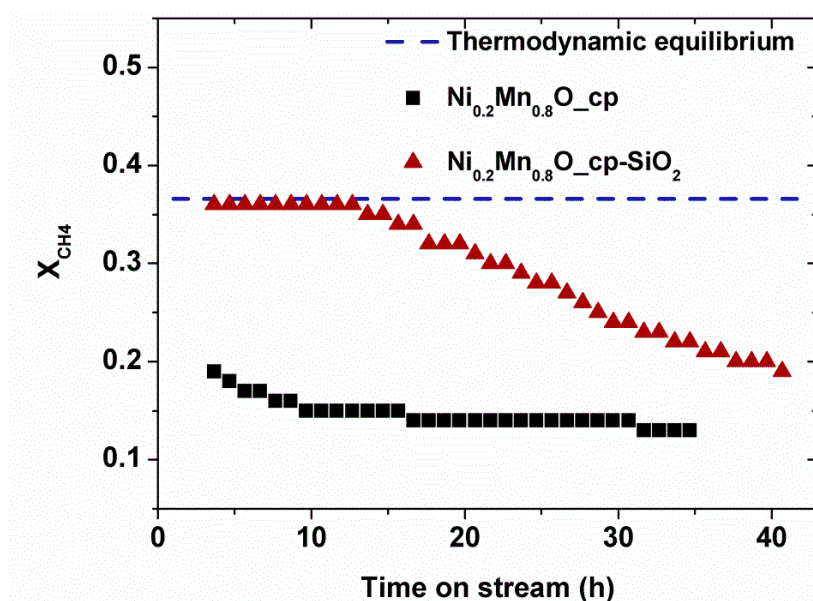


Figure 4.16 CH_4 conversion as a function of time on stream over catalysts $\text{Ni}_{0.2}\text{Mn}_{0.8}\text{O}_{\text{cp}}$ and $\text{Ni}_{0.2}\text{Mn}_{0.8}\text{O}_{\text{cp}}\text{-SiO}_2$. Reaction temperature 525 °C, $\text{CH}_4\text{:CO}_2\text{:N}_2\text{:He} = 1\text{:}1\text{:}0.5\text{:}7.5$ (Note that a double amount of $\text{Ni}_{0.2}\text{Mn}_{0.8}\text{O}_{\text{cp}}\text{-SiO}_2$ is used to observe the same molar amount of Ni in both catalysts. For $\text{Ni}_{0.2}\text{Mn}_{0.8}\text{O}_{\text{cp}}$, $m_{\text{cat}} = 50 \text{ mg}$, $\text{GHSV} = 80 \text{ L h}^{-1} \text{ g}_{\text{cat}}^{-1}$; for $\text{Ni}_{0.2}\text{Mn}_{0.8}\text{O}_{\text{cp}}\text{-SiO}_2$, $m_{\text{cat}} = 100 \text{ mg}$, $\text{GHSV} = 40 \text{ L h}^{-1} \text{ g}_{\text{cat}}^{-1}$).

Figure 4.16 shows the CH_4 conversion as function of time on stream over both catalysts $\text{Ni}_{0.2}\text{Mn}_{0.8}\text{O}_{\text{cp}}$ and $\text{Ni}_{0.2}\text{Mn}_{0.8}\text{O}_{\text{cp}}\text{-SiO}_2$. Both bulk and supported oxides show significant activity and $\text{Ni}_{0.2}\text{Mn}_{0.8}\text{O}$ can easily achieve TDE under mild condition below 550°C in the DRM reaction, which prevails over other reported Ni catalyst in the DRM reaction. Moreover, $\text{Ni}_{0.2}\text{Mn}_{0.8}\text{O}_{\text{cp}}\text{-SiO}_2$ shows a much higher activity than $\text{Ni}_{0.2}\text{Mn}_{0.8}\text{O}_{\text{cp}}$ among the whole course of the experiment and it achieved the TDE during the first 10 h, even though deactivation of this catalyst is more significant.

It should be mentioned that CH_4 conversion differs at 525 °C from the screening results (Figure 4.15) to the LTM results (Figure 4.16). In the screening experiment, the DRM reaction starts from 500 °C. When the temperature increases to 525 °C, both the structure and surface composition of the catalyst have changed. However, in the LTM measurement, the catalyst is fresh. Therefore it is impossible to compare the kinetics of these two experiments.

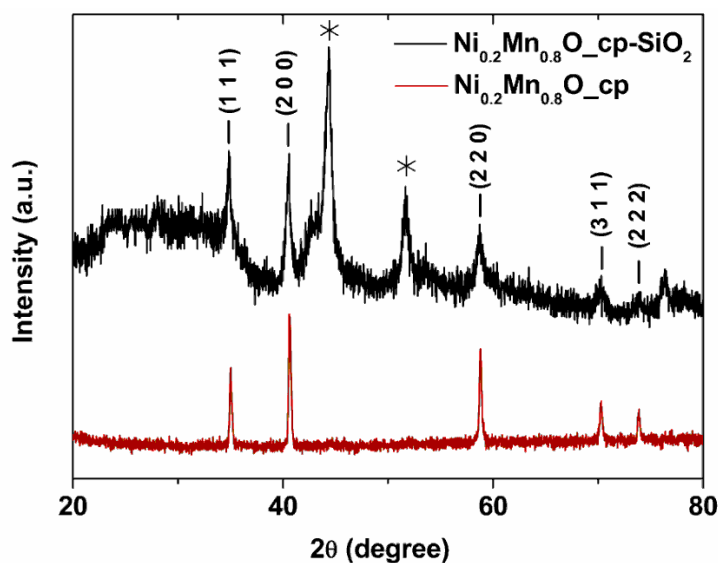


Figure 4.17 XRD patterns of $\text{Ni}_{0.2}\text{Mn}_{0.8}\text{O}_{\text{cp}}$ and $\text{Ni}_{0.2}\text{Mn}_{0.8}\text{O}_{\text{cp-SiO}_2}$ after 40 h time on stream measurement at a reaction temperature of 525 °C. The symbol (*) denotes diffraction peaks of Ni^0 phase.

In order to identify possible changes in the structure of the catalyst, XRD measurements are carried out on the material after the DRM reaction, shown in Figure 4.17. In case of $\text{Ni}_{0.2}\text{Mn}_{0.8}\text{O}_{\text{cp}}$ no considerable change in the XRD patterns is observed, beside a further increase in crystallite size (shown in Table 3), indicating particle sintering during the DRM reaction, a possible reason for the observed slow deactivation. $\text{Ni}_{0.2}\text{Mn}_{0.8}\text{O}_{\text{cp-SiO}_2}$ also shows some enlargement of the $\text{Ni}_x\text{Mn}_{1-x}\text{O}$ crystals, but additionally new distinct diffraction peaks attributed to formation of a Ni^0 metal phase are observed. Accordingly the peaks corresponding to the metal oxide slightly shift to lower angles, which is due to the depletion of nickel in the solid solution.

Notably, the formation of small NPs of the solid solution seems to facilitate the diffusion of Ni species to the surface and the reduction of Ni^{2+} to Ni^0 clusters, which is probably the main reason

for the significantly enhanced activity of the supported solid solution catalyst $\text{Ni}_{0.2}\text{Mn}_{0.8}\text{O}_{\text{cp}}\text{-SiO}_2$. On the other side, the facilitated reduction rate causes the agglomeration of Ni^0 clusters to larger Ni^0 NPs, which results in stronger deactivation in comparison to the bulk material.

Elemental analysis is also applied to investigate carbon deposition on the surface of the catalyst during the reaction. After 40 h reaction at 525 °C, both $\text{Ni}_{0.2}\text{Mn}_{0.8}\text{O}_{\text{cp}}$ and $\text{Ni}_{0.2}\text{Mn}_{0.8}\text{O}_{\text{cp}}\text{-SiO}_2$ show carbon deposition on the surface, with 2.38% and 3.54%, respectively (Table 3). This indicates that with both, bulk and supported $\text{Ni}_{0.2}\text{Mn}_{0.8}\text{O}$ catalysts, carbon deposition on the surface of the catalyst is not a sincere problem in the DRM reaction. Instead, Ni^0 NPs agglomeration could be the major problem which causes the catalyst deactivation.

In order to obtain dynamic information about the formation of Ni^0 clusters or NPs, PXRD patterns of the catalyst $\text{Ni}_{0.2}\text{Mn}_{0.8}\text{O}_{\text{cp}}\text{-SiO}_2$, after 1 h, 10 h and 40 h in the DRM reaction are performed, presented in Figure 4.18.

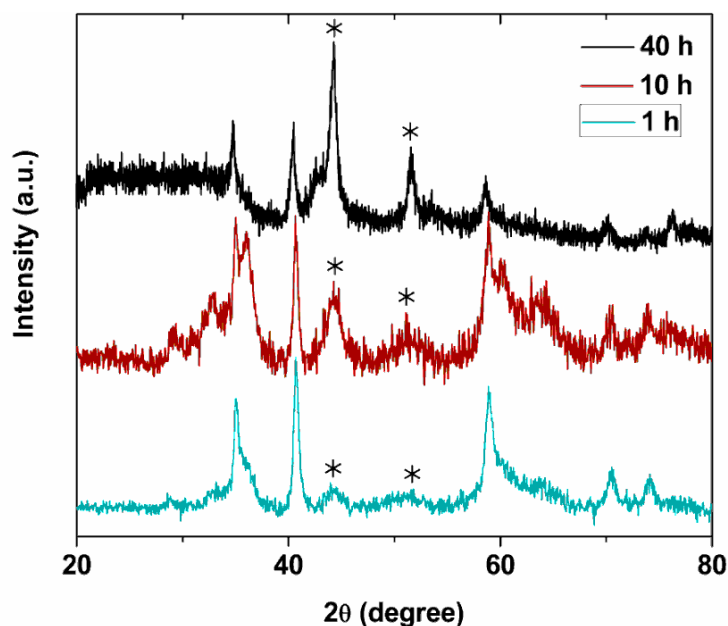


Figure 4.18 XRD patterns of $\text{Ni}_{0.2}\text{Mn}_{0.8}\text{O}_{\text{cp}}\text{-SiO}_2$ after 1 h, 10 h and 40 h over the DRM reaction at a reaction temperature of 525 °C. The symbol denotes diffraction peaks of (*) – Ni^0 phase.

From Figure 4.18, one can see that after 1 h reaction just very weak peaks for Ni^0 can be identified, while after 10 h these peaks become more noticeable and finally become the most

prominent features in the diffractogram after 40 h reaction. Besides the relative intensity, the average size of the Ni^0 crystallites also increases with prolonged reaction time. Thus indeed the agglomeration of Ni^0 clusters to larger Ni^0 NPs is the main reason for the catalyst deactivation.

To verify the effect of the reaction temperature on the formation of Ni^0 and therefore the stability of the supported solid solution catalyst, a LTM using $\text{Ni}_{0.2}\text{Mn}_{0.8}\text{O}_{\text{cp}}\text{-SiO}_2$ is conducted at 500 °C and 550 °C separately, shown in Figure 4.19.

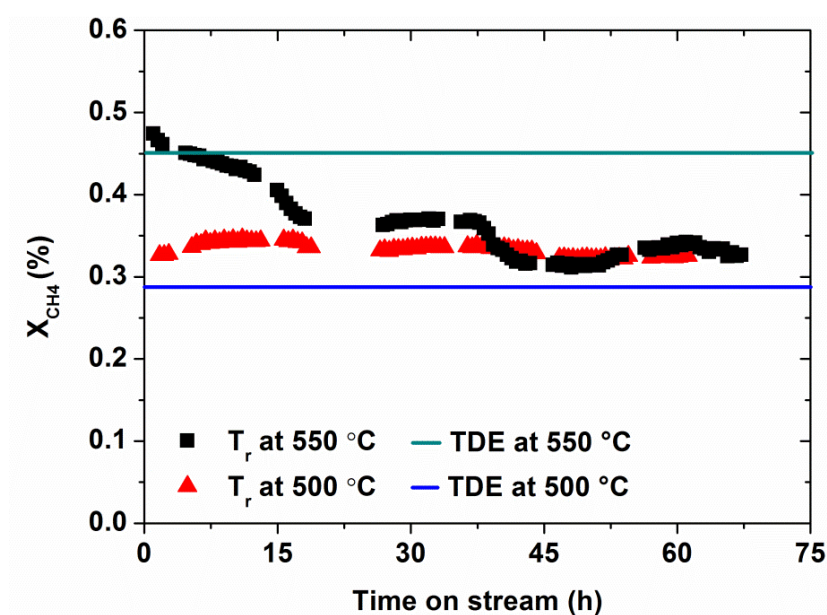


Figure 4.19 The long term stability of $\text{Ni}_{0.2}\text{Mn}_{0.8}\text{O}_{\text{cp}}\text{-SiO}_2$ in the DRM reaction. CH_4 conversion as a function of time on stream. $m_{\text{cat}} = 100$ mg, $\text{CH}_4:\text{CO}_2:\text{N}_2:\text{He} = 1:1:0.5:7.5$, GHSV = $40 \text{ L h}^{-1} \text{ g}^{-1}$.

As expected, also at 550 °C, the catalyst is deactivating rather fast, here even from the beginning of the reaction and reaches a steady state just after 45 h. At least, afterwards the catalyst is showing stable performance still at relatively high level. Beside the formation of large Ni^0 NPs, BET measurements reveals that in the surface area of $\text{Ni}_{0.2}\text{Mn}_{0.8}\text{O}_{\text{cp}}\text{-SiO}_2$ decreases from $221 \text{ m}^2/\text{g}$ to $128 \text{ m}^2/\text{g}$ at 550°C after 65 h reaction, while just negligible changes are observed at 500°C. Thus for the catalyst at 550°C structural changes of the support or particle sintering can be an additional reason for the observed deactivation. At 500 °C the catalyst shows remarkable stability during the whole course of the reaction even after 60 h.

Indeed PXRD of the catalyst after the LTM in Figure 4.20 verifies the assumption that no larger Ni^0 NPs are formed at this temperature, instead, just very weak and broad peaks which can be attributed to the formation of Ni^0 are observed. Additionally the catalyst is investigated by elemental analysis. After 60 h at 500 °C only a trace amount of carbon is observed (0.21%). Thus one can conclude that at relative low temperature, the reduction velocity of Ni^{2+} to Ni^0 is restricted and Ni^0 can be highly dispersed on the surface of the ternary oxide, by that the agglomeration of small Ni^0 clusters to larger particles can be suppressed, therefore the formation of carbon deposition is suppressed, which ensured the stability of the catalyst.

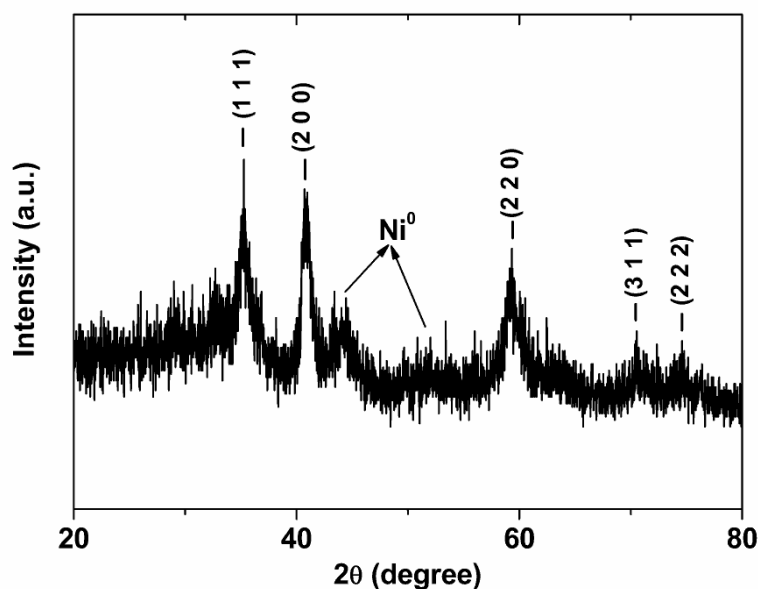


Figure 4.20 XRD patterns of $\text{Ni}_{0.2}\text{Mn}_{0.8}\text{O}_{\text{cp}}\text{-SiO}_2$ after 60 h LTM at 500 °C.

4.3.3.3 Long time stability at 675 °C

In order to inhibit carbon formation on the surface of the catalyst, a LTM with the catalyst $\text{Ni}_{0.2}\text{Mn}_{0.8}\text{O}_{\text{cp}}\text{-SiO}_2$ is measured at 675 °C and the fraction of carbon dioxide is raised to 0.67, presented in Figure 4.21B. The reaction conditions are similar as the LTM with the bulk catalyst $\text{Ni}_{0.2}\text{Mn}_{0.8}\text{O}_{\text{cp}}$ (Figure 4.21A).

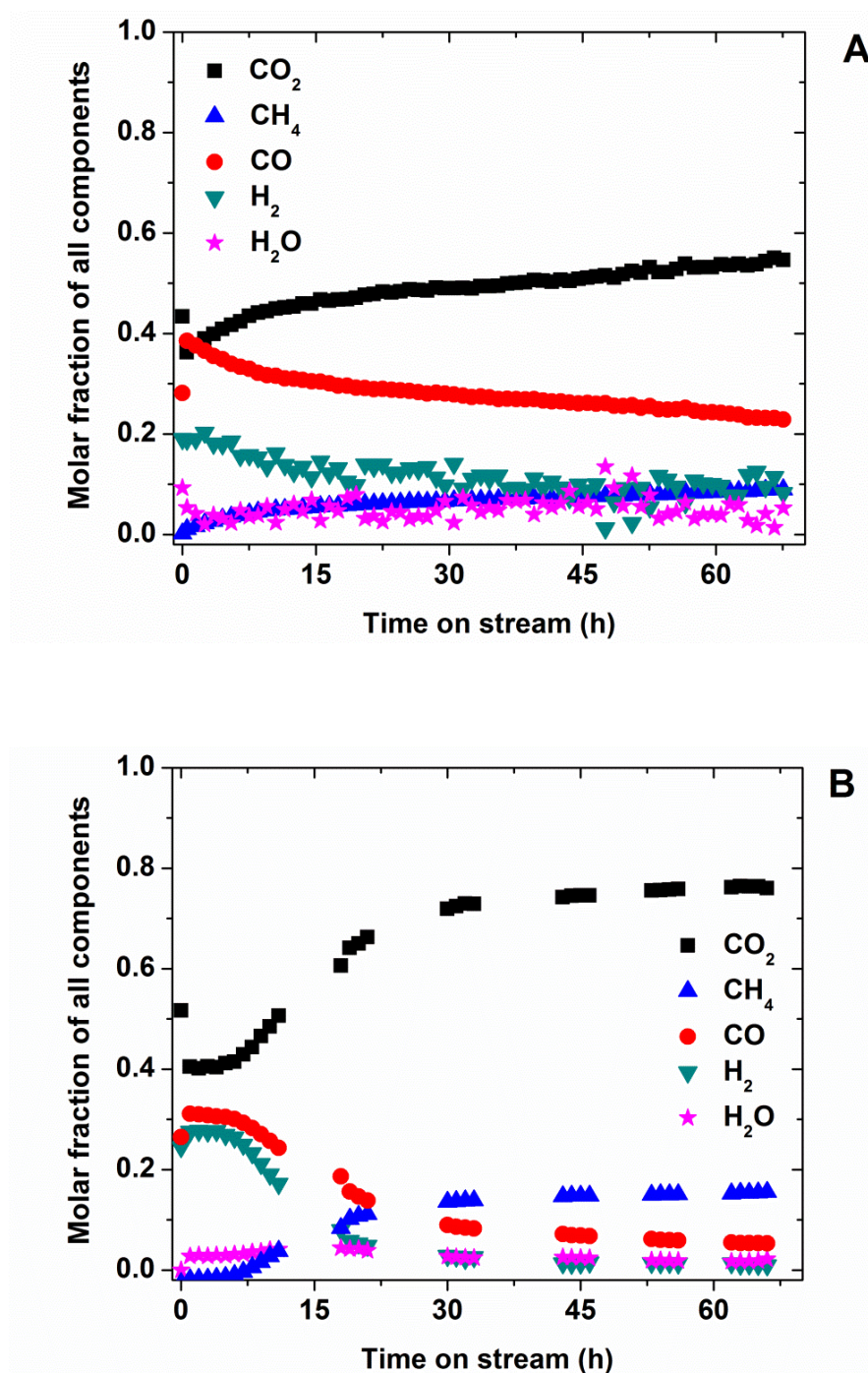


Figure 4.21 A LTM of Ni_{0.2}Mn_{0.8}O_{cp}-SiO₂ (down, B) for the DRM reaction at 675 °C. Molar fraction of all components changes with time on stream. (GHSV = 30 L h⁻¹ g⁻¹, feed gas CH₄:CO₂:N₂ = 1:5:1.5, Note that N₂ is excluded from molar fraction calculation.) For comparison, Figure 4.8 (upper, A) is presented together.

From these two LTMs, overall speaking, the SiO_2 supported catalyst $\text{Ni}_{0.2}\text{Mn}_{0.8}\text{O}_{\text{cp-SiO}_2}$ shows similar catalytic performance as the bulk catalyst $\text{Ni}_{0.2}\text{Mn}_{0.8}\text{O}_{\text{cp}}$: the molar fraction of CO_2 , CO and H_2O over the 1st point is discrete from that of the following points; the first points of molar fractions show a complete consumption of CH_4 , little or no conversion of CO_2 and a low yield of CO ; as the reaction time proceeds, the molar fraction of CH_4 and CO_2 is increasing, in parallel the yield of H_2 and CO is decreasing. However, these are also some different phenomena in these two experiments:

1. In case of the first point (the reaction starting point), there is no H_2O formation over the catalyst $\text{Ni}_{0.2}\text{Mn}_{0.8}\text{O}_{\text{cp-SiO}_2}$. In contrast, H_2O formation is relatively high over the catalyst $\text{Ni}_{0.2}\text{Mn}_{0.8}\text{O}_{\text{cp}}$. From the view of the whole reaction range, the molar fraction of produced H_2O also shows large differences in these two catalysts. Over the bulk catalyst, the fraction of H_2O is between 0.01 and 0.05 during the whole reaction; oppositely, over the supported catalyst, only a neglectable amount of H_2O is produced. This means that the RWGS reaction is stronger inhibited over the supported catalyst $\text{Ni}_{0.2}\text{Mn}_{0.8}\text{O}_{\text{cp-SiO}_2}$.
2. $\text{Ni}_{0.2}\text{Mn}_{0.8}\text{O}_{\text{cp-SiO}_2}$ is stable in the beginning and starts deactivation after 7 h reaction. After 65 h reaction, the catalyst shows very low activity with the molar fraction of H_2 and CO 0.01 and 0.05, respectively. The activity somehow achieves a steady state. In case of the bulk catalyst $\text{Ni}_{0.2}\text{Mn}_{0.8}\text{O}_{\text{cp}}$, the catalyst shows deactivation right after the start of the DRM reaction and the deactivation rate slows down after around 15 h but it has not approached the steady state yet after 65 h reaction. In the end, the molar fraction of H_2 and CO is 0.08 and 0.23, respectively, which is much higher than that over the supported catalyst $\text{Ni}_{0.2}\text{Mn}_{0.8}\text{O}_{\text{cp-SiO}_2}$.
3. With the supported catalyst, the molar ratio of CO/H_2 remains at a value of 1.1 during the first 10 h reaction and increases up to 5.5 with time on stream because of the low yield of H_2 . With the bulk catalyst, the molar ratio of CO/H_2 is fluctuating between 1.8 and 3.0 along the whole reaction time. This indicates that the rates of CH_4 decomposition reaction and the Boudouard reaction differ over the bulk and the supported catalysts.

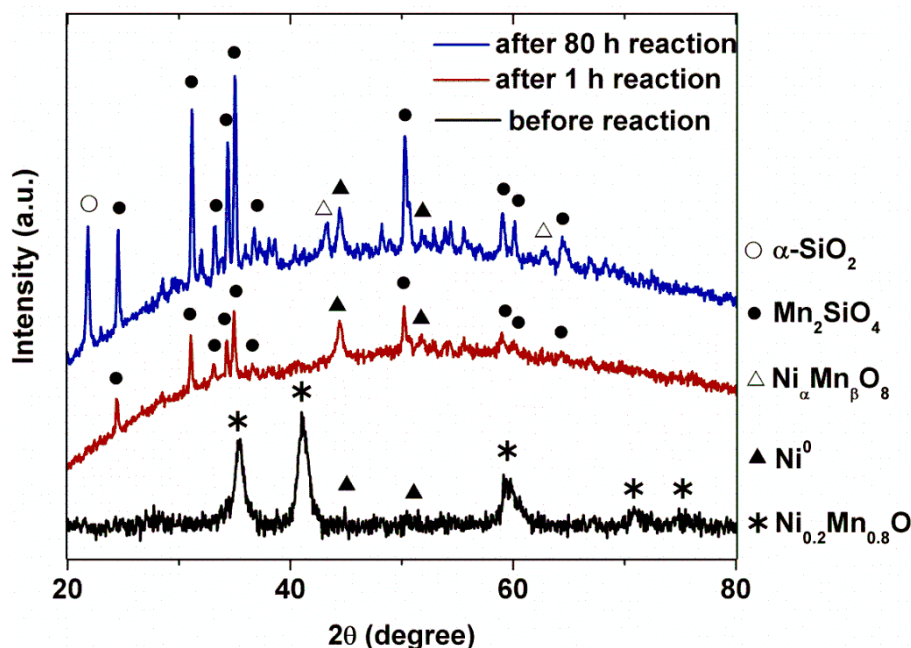


Figure 4.22 XRD patterns of $\text{Ni}_{0.2}\text{Mn}_{0.8}\text{O}_{\text{cp-SiO}_2}$ before and after 1 h, 80 h reaction at 675 °C. (Note that the additional SiO_2 phase of the catalyst after 80 h reaction is from the external mixture of SiO_2 beads in order to dilute the catalyst.)

$\text{Ni}_{0.2}\text{Mn}_{0.8}\text{O}_{\text{cp-SiO}_2}$ after the LTM at 675 °C is characterized by XRD to obtain information about the deactivation mechanism. In Figure 4.22, XRD of $\text{Ni}_{0.2}\text{Mn}_{0.8}\text{O}_{\text{cp-SiO}_2}$ before, after 1 h and 80 h in the DRM reaction (at 675 °C) are presented. As mentioned above, before the reaction, $\text{Ni}_{0.2}\text{Mn}_{0.8}\text{O}_{\text{cp-SiO}_2}$ is composed of a solid solution of $\text{Ni}_{0.2}\text{Mn}_{0.8}\text{O}$ phase (marked as *). After 1 h reaction already a significant phase change has occurred. The solid solution phase disappeared, instead Mn_2SiO_4 (marked as •) and Ni^0 (marked as ▲) phases are formed. After 80 h reaction, the catalyst presents a relative higher intensity of Mn_2SiO_4 and an extra phase of Ni_6MnO_8 (marked as Δ). This shows that the net content of Ni^0 is decreasing during the reaction caused by the transition of Ni^0 to Ni_6MnO_8 phase. Therefore, one can conclude that $\text{Ni}_{0.2}\text{Mn}_{0.8}\text{O}_{\text{cp-SiO}_2}$ catalyst is less stable than $\text{Ni}_{0.2}\text{Mn}_{0.8}\text{O}_{\text{cp}}$ at higher temperatures (> 600 °C) due to the phase transition of $\text{Ni}_{0.2}\text{Mn}_{0.8}\text{O}$ to Mn_2SiO_4 and Ni_6MnO_8 phases. In contrast, at lower temperatures (< 550 °C), $\text{Ni}_{0.2}\text{Mn}_{0.8}\text{O}_{\text{cp-SiO}_2}$ shows impressively high stability as well as high activity.

4.3.4 $\text{Ni}_{0.05}\text{Mn}_{0.95}\text{O}/\text{SiO}_2$ calcined at high temperature

In Chapter 4.3.2 and 4.3.3, it is shown that the solid solution $\text{Ni}_{0.2}\text{Mn}_{0.8}\text{O}$ is highly active for the DRM reaction. However, this catalyst suffers from the fast deactivation. There are two main reasons for the catalyst deactivation, particle sintering and carbon deposition individually. The former one is dominant in the beginning of the reaction causing an exponential decay of the activity and this effect becomes weaker or even disappears as reaction time proceeds; the latter one is a relative minor factor, leading to a slower and linear deactivation during the whole reaction time period.

A simple method to inhibit the effect from particle sintering during reaction applications is calcining the catalyst at high temperature or decreasing the loading of Ni. During high temperature calcination particles have sintered, therefore this effect will not further disturb the catalytic behavior of the catalyst during the reaction applications. Based on this idea, a new catalyst of $\text{Ni}_{0.05}\text{Mn}_{0.95}\text{O_cp-SiO}_2$ is prepared. It is calcined at 750 °C for 4 h. The obtained material is investigated by TPR. Afterwards this material is reduced under H_2 at 750 °C for 4 h and investigated by XRD. It is named as $\text{Ni}_{0.05}\text{Mn}_{0.95}\text{O_cp-SiO}_2\text{_{750}}$.

In Figure 4.23, H_2 -TPR profile of as synthesized $\text{Ni}_{0.05}\text{Mn}_{0.95}\text{O_cp-SiO}_2\text{_{750}}$ (before reduction) shows a dominant peak at 577 °C and a small peak in the range of 706-730 °C. Considering the large difference of area, these two peaks are most probably attributed to the reduction sequence from Mn^{4+} to Mn^{2+} and from Ni^{2+} to Ni^0 . This is different from the TPR profile of as synthesized $\text{Ni}_{0.2}\text{Mn}_{0.8}\text{O_cp-SiO}_2\text{_{500}}$, in which two peaks occurring between 200-250 °C and 300-350 °C respectively with similar area are attributed to the reduction sequence from Mn^{4+} to Mn^{3+} and finally to Mn^{2+} . The appearance of peaks at much higher temperature indicates that $\text{Ni}_{0.05}\text{Mn}_{0.95}\text{O_cp-SiO}_2\text{_{750}}$ is much more difficult to reduce.

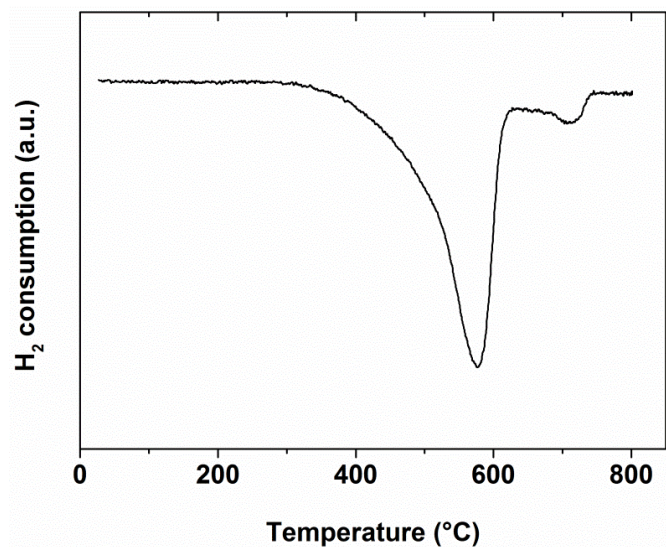


Figure 4.23 H₂-TPR profile of Ni_{0.05}Mn_{0.95}O_{cp}-SiO₂_750 before reduction.

Compared to Ni_xMn_{1-x}O_{cp}-SiO₂_500, Ni_{0.05}Mn_{0.95}O_{cp}-SiO₂_750 is more difficult to reduce. This phenomenon is also observed in case of the solid solution catalyst Ni_{0.03}Mg_{0.97}O.⁷⁵ The calcination of this catalyst proceeded at 850 °C and the following reduction process required the same high temperature. Therefore, Ni_{0.05}Mn_{0.95}O_{cp}-SiO₂_750 is reduced at 750 °C for 4 h before the catalytic applications. Figure 4.24 shows the XRD patterns of Ni_{0.05}Mn_{0.95}O_{cp}-SiO₂_750. It indicates that a solid solution phase is formed.

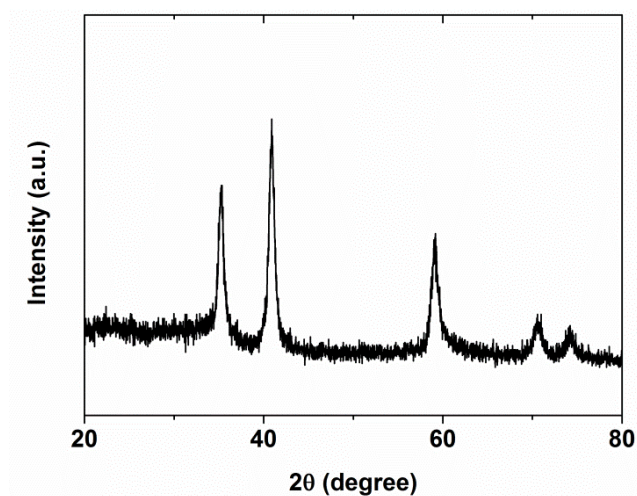


Figure 4.24 XRD patterns of Ni_{0.05}Mn_{0.95}O_{cp}-SiO₂_750.

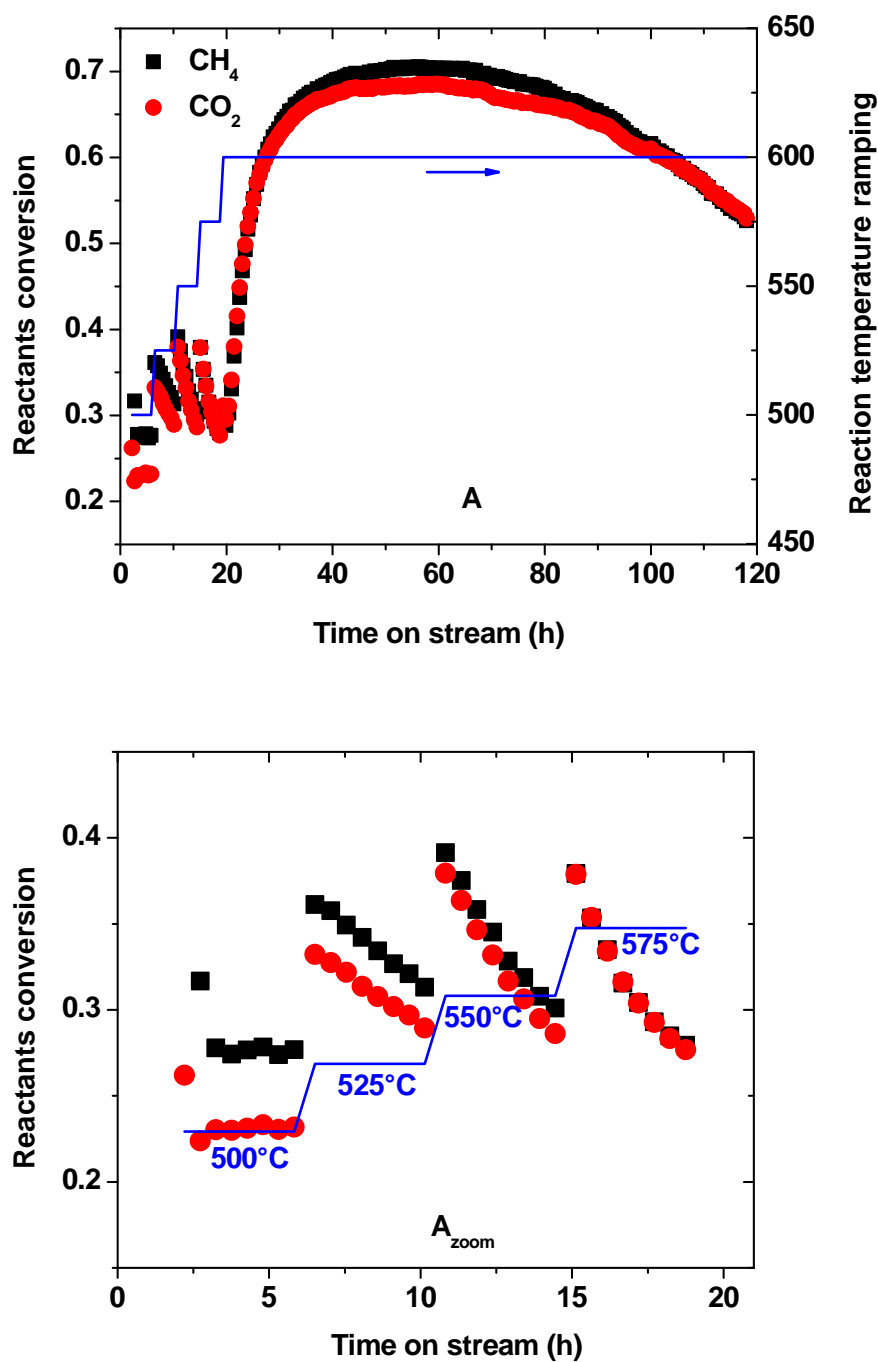


Figure 4.25 A: CH_4 and CO_2 conversion as a function of time on stream with the catalyst $\text{Ni}_{0.05}\text{Mn}_{0.95}\text{O}_{\text{cp-SiO}_2_{750}}$, B: the zoom into plot A between 500 and 575 °C, in the DRM reaction for 5 days. Reaction conditions: $m_{\text{cat}} = 50 \text{ mg}$, $\text{GHSV} = 80 \text{ L h}^{-1} \text{ g}^{-1}$.

$\text{Ni}_{0.05}\text{Mn}_{0.95}\text{O}_{\text{cp-SiO}_2_{750}}$ is applied to the DRM reaction. Figure 4.25 shows the catalytic performance of this catalyst in the DRM reaction. The reaction temperature starts from 500 °C

and is increased in steps of 25 K/h to 600 °C. Between 500-575 °C, each temperature is held for 5 h and afterwards the reaction is settled at 600 °C for 100 h. (the screening results shown here were provided by Patrick Littlewood.)

From Figure 4.25 some interesting information can be deduced:

1. Between 500 - 575 °C, $\text{Ni}_{0.05}\text{Mn}_{0.95}\text{O}_{\text{cp-SiO}_2}$ _750 shows very similar catalytic behavior as $\text{Ni}_{0.2}\text{Mn}_{0.8}\text{O}_{\text{cp-SiO}_2}$ _500 (Figure 4.15). This catalyst is stable at 500 °C but deactivates fast over 500 °C, and the activity increases as ramping reaction temperature. Since the catalyst is calcined at 750 °C for 4 h, it is doubtful that the fast deactivation is caused by particle sintering. The later activity jumping at 575-600 °C also can prove that the fast deactivation between 500-575 °C could not be caused by particle sintering since this effect is not reversible.

2. Between 500 - 525 °C, especially at 500 °C (the starting stage of the reaction), conversion of CH_4 is much higher than that of CO_2 , which indicates that the rate of CH_4 decomposition (eq. 9, $\Delta_{\text{RH}}^\circ = 75.6 \text{ kJ/mol}$) is higher than that of the reverse Boudouard reaction (eq. 10, $\Delta_{\text{RH}}^\circ = 172 \text{ kJ/mol}$) in this temperature range. This is reasonable because CH_4 decomposition is much less endothermic than the reverse Boudouard reaction which makes CH_4 decomposition much more preferable at low reaction temperature. Due to the predominant CH_4 decomposition reaction, carbon species are not able to react with CO_2 and to be removed completely from the surface of the active sites, which causes the fast deactivation between 500-575 °C. As the reaction temperature increases, the reverse Boudouard reaction is accelerated. Therefore, the surface carbon is removed fast by that the deactivation is inhibited and the activity of the catalyst is recovered.

3. When the reaction temperature increases to 600 °C, $\text{Ni}_{0.05}\text{Mn}_{0.95}\text{O}_{\text{cp-SiO}_2}$ _750 shows dramatically increasing activity and achieves highest activity in several hours. The reaction achieves TDE with only 50 mg catalyst and high value GHSV $80 \text{ L h}^{-1} \text{ g}^{-1}$. This catalyst is relative stable and the conversion of CH_4 or CO_2 remains over 50% after 5 days running. Since structural change is avoided by the high calcination temperature, the occurred weak deactivation at 600 °C is most probably a result of surface carbon deposition (due to a slighter higher CH_4 conversion compared to CO_2 conversion) or a phase transition. A further characterization can help to find the answer.

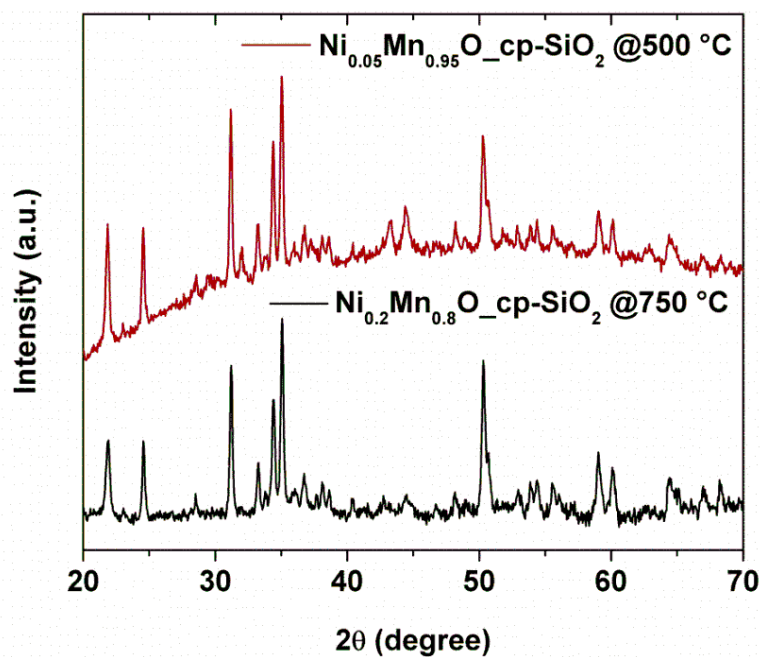


Figure 4.26 XRD patterns of $\text{Ni}_{0.05}\text{Mn}_{0.95}\text{O}_{\text{cp-SiO}_2}$ _750 (after 5 days running at 600°C) and $\text{Ni}_{0.2}\text{Mn}_{0.8}\text{O}_{\text{cp-SiO}_2}$ _500 (after 80 h running at 675°C).

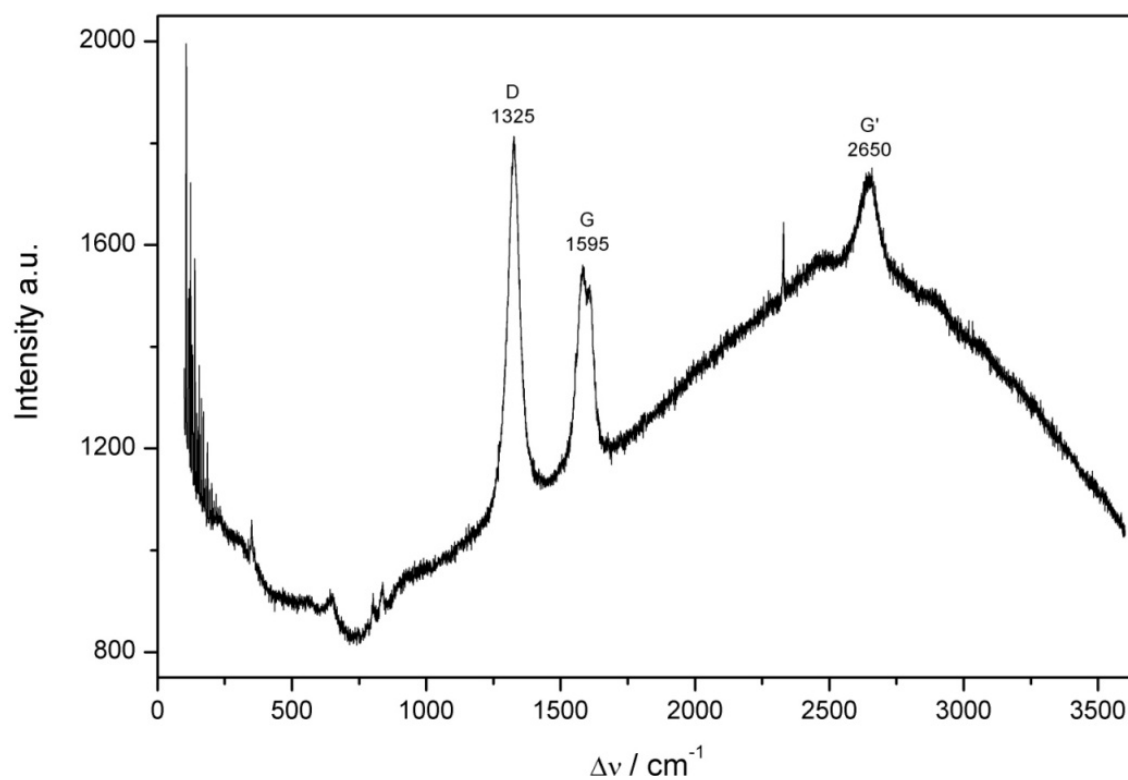


Figure 4.27 Raman spectra of $\text{Ni}_{0.05}\text{Mn}_{0.95}\text{O}_{\text{cp-SiO}_2}$ _750 after 5 days running at 600°C .

$\text{Ni}_{0.05}\text{Mn}_{0.95}\text{O}_{\text{cp-SiO}_2}$ _750 after the reaction is investigated by XRD. Figure 4.26 shows the XRD pattern of this catalyst after 5 days operation at 600 °C. For comparison, the XRD pattern of $\text{Ni}_{0.2}\text{Mn}_{0.8}\text{O}_{\text{cp-SiO}_2}$ _500 (after 80 h running at 675 °C) is also presented. Two patterns are very similar, phase transition occurred to both samples during the LTM reaction. The Raman spectrum of $\text{Ni}_{0.05}\text{Mn}_{0.95}\text{O}_{\text{cp-SiO}_2}$ _750 after the reaction is shown in Figure 4.27, indicating the formation of multi-walled carbon nanotubes.

From the difference of catalytic performance between the catalysts $\text{Ni}_{0.2}\text{Mn}_{0.8}\text{O}_{\text{cp-SiO}_2}$ _500 and $\text{Ni}_{0.05}\text{Mn}_{0.95}\text{O}_{\text{cp-SiO}_2}$ _750, one can obtain some detail information about the impact of material structure on the catalytic properties:

1. In the reoxidation experiment, the catalyst $\text{Ni}_{0.2}\text{Mn}_{0.8}\text{O}_{\text{cp-SiO}_2}$ _500 is deactivated due to particle sintering and surface carbon deposition. Particle sintering is most pronounced in the beginning of the reaction, however, the particles become stable after reaching a certain size. Compared to particle sintering, surface carbon deposition is a minor factor but it can occur during the whole reaction. In case of the catalyst $\text{Ni}_{0.05}\text{Mn}_{0.95}\text{O}_{\text{cp-SiO}_2}$ _750, the catalytic deactivation starts after 68 h running at 600 °C. It strongly indicates that the deactivation is caused by surface carbon deposition, not related to particle sintering. This is reasonable since high calcination temperatures induce larger stable particles therefore particle sintering will not further occur during the following catalytic applications.

2. $\text{Ni}_{0.05}\text{Mn}_{0.95}\text{O}_{\text{cp-SiO}_2}$ is stable for 68 h at 600 °C. However deactivation starts afterwards. It is observed that this catalyst shows phase transition from a solid solution of NiMnO to a mixed phase of Mn_2SiO_4 and Ni_6MnO_8 after the reaction. It is rational to infer that the phase transition is the direct reason for the catalyst deactivation. When the solid solution phase NiMnO disappears, the activity of the catalyst is decreased therefore more surface carbon is deposited which further weakens the activity of the catalyst. As a result, this can explain the accelerated deactivation during the last 40 h of the 5 days experiment. Therefore, one can conclude that the solid solution NiMnO is the catalyst which inhibits surface carbon deposition during the DRM reaction.

3. At relative low temperatures, the rate of the reverse Boudouard reaction is too low to remove the surface carbon from CH_4 decomposition therefore causes severe surface carbon deposition and fast catalyst deactivation. At relative high temperatures, a phase transition will occur and the catalyst is no longer a solid solution of NiMnO, so that the activity of the catalyst will decrease

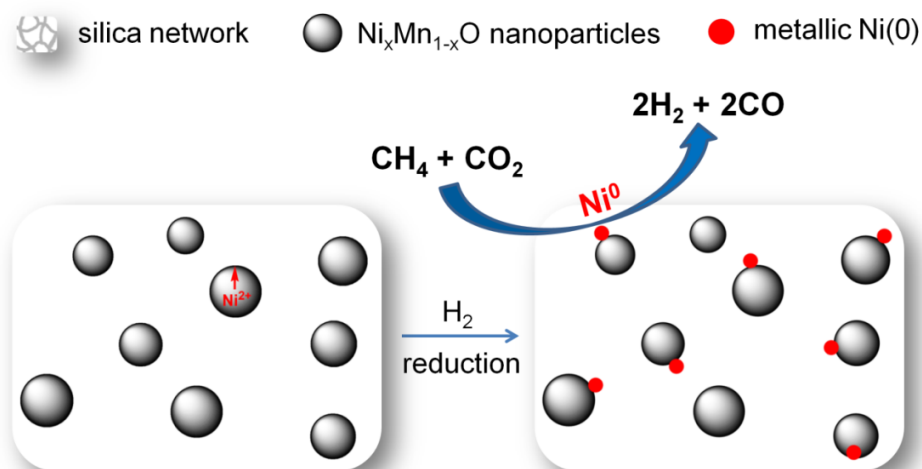
which slows down the reverse Boudouard reaction and causes surface carbon deposition and subsequent fast catalyst deactivation. In conclusion, a suitable reaction temperature is crucial for maintaining the extraordinary stability as well as activity of a NiMnO catalyst. The reaction temperature between 575-600 °C is the optimal temperature for a NiMnO catalyst to maintain its best catalytic performance.

4.4 Summary and conclusion

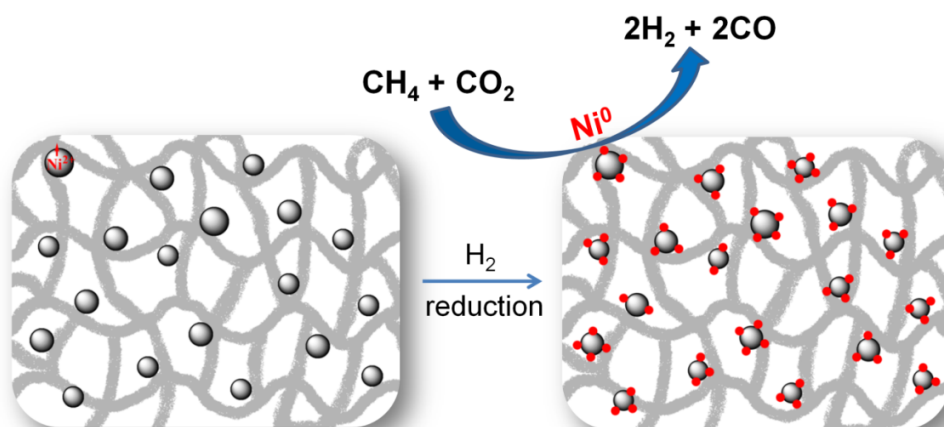
The DRM project describes the synthesis and characterization of a solid solution catalyst $\text{Ni}_x\text{Mn}_{1-x}\text{O}$ and its catalytic performance in the DRM reaction. The highlight of this project is the utilization of $\text{Ni}_x\text{Mn}_{1-x}\text{O}$ for the first time for catalytic applications, and the extraordinary high activity of this catalyst in the DRM reaction. $\text{Ni}_x\text{Mn}_{1-x}\text{O}$ is chosen as the model catalyst for the DRM reaction due to SMSI between Ni and MnO, the identical crystal structure of NiO and MnO (NaCl type), the low cost and abundance of Ni and Mn elements, and a strong CO_2 adsorption property of MnO.

By a combined co-precipitation and sol-gel process, $\text{Ni}_x\text{Mn}_{1-x}\text{O}$ nanocrystallites are formed and highly disperse on an amorphous silica support. The presence of silica has no impact on the formation of the solid solution of $\text{Ni}_x\text{Mn}_{1-x}\text{O}$. By varying the pH, the velocity of metal precipitation and silica precursor gelation is controlled so that the metal precipitates are highly dispersed into the silica network. Compared to other tedious methods, one-pot synthesis is efficient and scalable. In addition, the herein used silica precursor is sodium metasilicate (water glass), which is much cheaper than common silica precursors, e.g. with the price of only 0.2% of TEOS or TMOS.

During the catalytic applications, $\text{Ni}_x\text{Mn}_{1-x}\text{O}$ exhibits extraordinary high activity for the DRM reaction and the TDE of the reaction has been achieved for the first time at the reaction temperature below 600 °C. A summary of this project is presented in Figure 4.28. Taking all information presented into consideration, one can draw detailed conclusion how preparation methods and structural changes influence the catalytic performance of $\text{Ni}_x\text{Mn}_{1-x}\text{O}$ for the DRM reaction:



Bulk NiMnO : large spheres, long diffusion path for Ni^{2+} to the surface, difficult formation of Ni^0 . Nevertheless, active and stable.



NiMnO supported on silica: small NiMnO nanocrystallites, short diffusion path for Ni^{2+} to the surface, fast formation of Ni^0 . Highly active and stable

Figure 4.28 The overview of the project *Amorphous silica supported NiMnO nanocrystallites for the DRM reaction*.

A solid solution of $\text{Ni}_x\text{Mn}_{1-x}\text{O}$ with varied Ni/Mn composition can be obtained by the co-precipitation method. Due to the co-reactant NaHCO_3 , the obtained $\text{Ni}_x\text{Mn}_{1-x}\text{O}$ catalyst shows a high surface area of $150\text{--}170\text{ m}^2/\text{g}$. The bulk catalyst $\text{Ni}_{0.2}\text{Mn}_{0.8}\text{O}_{\text{cp}}$ is very active for the DRM reaction. It can be activated at a low reaction temperature and shows already some activity at $400\text{ }^\circ\text{C}$. Compared to $\text{Ni}_{0.2}\text{Mg}_{0.8}\text{O}_{\text{cp}}$ prepared by the same method under identical conditions,

$\text{Ni}_{0.2}\text{Mn}_{0.8}\text{O}_{\text{cp}}$ exhibits a significantly enhanced activity in the DRM reaction. Since both catalysts have a similar surface area and a solid solution structure, the activity promotion of $\text{Ni}_{0.2}\text{Mn}_{0.8}\text{O}_{\text{cp}}$ is most probably attributed to SMSI between Ni and MnO which is absent between Ni and MgO. Due to SMSI, the adsorption of CO and H_2 to the surface of the catalyst is strongly suppressed, which accelerates the DRM reaction to the production of synthesis gas. When Ni loading is controlled at 10 mol%, the catalyst shows the best performance. The fast deactivation during the beginning of the DRM reaction is mainly caused by metal/metal oxide particle agglomeration, which is irreversible. After a certain reaction time, when the structure of the catalyst becomes stable, surface carbon deposition is the main reason for the further slow deactivation which can be recovered by a reoxidation reaction.

A silica supported catalyst, $\text{Ni}_{0.2}\text{Mn}_{0.8}\text{O}_{\text{cp}}\text{-SiO}_2$, can be obtained by a combined method of co-precipitation and sol-gel process. This silica supported catalyst shows significant improvement in stability as well as in activity compared to the bulk catalyst, which is due to the formation of small and highly dispersed nanocrystallites of NiMnO. This causes easier formation of small Ni^0 clusters on the surface of the catalyst during the reduction process. $\text{Ni}_{0.2}\text{Mn}_{0.8}\text{O}_{\text{cp}}\text{-SiO}_2$ exhibits a different catalytic behavior with different reaction temperatures. At 500 °C, $\text{Ni}_{0.2}\text{Mn}_{0.8}\text{O}_{\text{cp}}\text{-SiO}_2$ is highly stable. After 40 h time on stream, no deactivation is observed, and no structure or phase change is detected. When the reaction temperature is increased to 550 °C, deactivation is observed due to Ni^0 particles growing and sintering. The solid solution phase remained, however, an increase in the size of nanocrystallites is observed. At 675 °C, the catalyst shows severe deactivation after 10 h time on stream, and it shows almost no activity after 65 h. Because of the high temperature, the solid solution $\text{Ni}_x\text{Mn}_{1-x}\text{O}$ phase converts to Mn_2SiO_4 and $\text{Ni}_\alpha\text{Mn}_\beta\text{O}_8$ phases.

After a further optimization by decreasing Ni loading (5 mol%) and increasing the calcination temperature (750 °C), the silica supported catalyst shows significantly improved stability. It is highly active with higher than 50% of CH_4/CO_2 conversion even after 5 days time on stream at 600 °C.

Many factors influence the catalytic performance of silica supported NiMnO nanocrystallites. Besides the preparation methods and structural change, reaction conditions are also studied. At low temperatures, the rate of the Boudouard reaction is too low to remove the surface carbon from CH_4 decomposition therefore surface carbon deposition is caused and the catalyst is fast

deactivated. At higher temperatures, a phase transition will occur and the catalyst is no longer a solid solution of NiMnO, so that the activity of the catalyst is decreased which slows down the reverse Boudouard reaction and causes surface carbon deposition and subsequent fast catalyst deactivation. 575-600 °C is an optimal reaction temperature for a silica supported NiMnO catalyst to maintain its best catalytic performance.

5. Mesoporous silica supported NMNPs for catalytic applications

5.1 One-pot synthesis of silica xerogel supported Pd NPs for catalytic applications

Recently, it was shown that a hyperbranched polymer polyglycerol block poly(ethylene glycol) (hPG-b-mPEG) can be used as a template for the preparation of mesoporous silicas.¹⁶⁰ In this project, hPG-b-mPEG is used as a stabilizer to avoid Pd NPs agglomeration during immobilization process. In this procedure, the stabilizer is allowed to be washed out completely by water extraction, instead of being removed and thus destroyed by calcination, an important prerequisite for up-scaling the catalyst preparation. Thus, in the next step the polymer can be reused as NP stabilizer for the preparation of the next batch of catalysts, so that the here shown process is highly material efficient.

The conditions of the sol-gel process which have strong influence on the specific surface area of silica gel and the accumulation of Pd NPs are investigated, and also the reactivity of the catalyst in the hydrogenation of cyclooctadiene (COD) is studied. The advantage of the strategy shown here is that preformed Pd NPs are used, which are stabilized by a water soluble polymer (hPG-b-mPEG) with core-shell structure. Thus the control of the particle size of Pd is ensured, compared to the direct reduction of metal salts in the sol-gel process. On the other hand, the support is synthesized in presence of the stabilized NPs ensuring embedding and stabilization of the metal inside the pores, instead of loading NPs into a preformed support in a subsequent step, which would constrict the applicable porous architectures as the particles have to diffuse through the porous system.

Chapter 5.1 shows the 1st project, “the one-pot synthesis of silica xerogel supported Pd NPs for catalytic applications”. In this project, I cooperated with Ms. Sabrina Nowag (AG Haag, FU Berlin), who provided preformed Pd metal sol solution stabilized by core-shell architecture hyperbranched polyglycerol block poly(ethylene glycol) (hPG-b-mPEG). The 2nd project shown in chapter 5.2 is “One-pot synthesis of Pt NPs supported on SBA-15 for catalytic applications”. In this project, I worked together with Dr. Junjiang Zhu (a former colleague in AG Thomas, TU Berlin, currently a Professor in South-central University for Nationalities, Wuhan, China). My work was mainly focused on the catalytic investigations and the synthesis method of SBA-15 supported NMNPs.

5.1.1 Synthesis and characterization of silica xerogel supported Pd catalysts

The synthetic scheme for the silica xerogel supported Pd material is presented in Figure 5.1. In the Pd sol, Pd NPs are stabilized by a core-shell architected polymer hyperbranched polyglycerol-block-poly(ethylene glycol) (hPG-b-mPEG), which inhibit Pd NPs agglomeration during the following sol-gel process. After gelation the stabilizer copolymer hPG-b-mPEG is completely removed by water ultrasonication and can be reused for the next preparation of the metal sol.

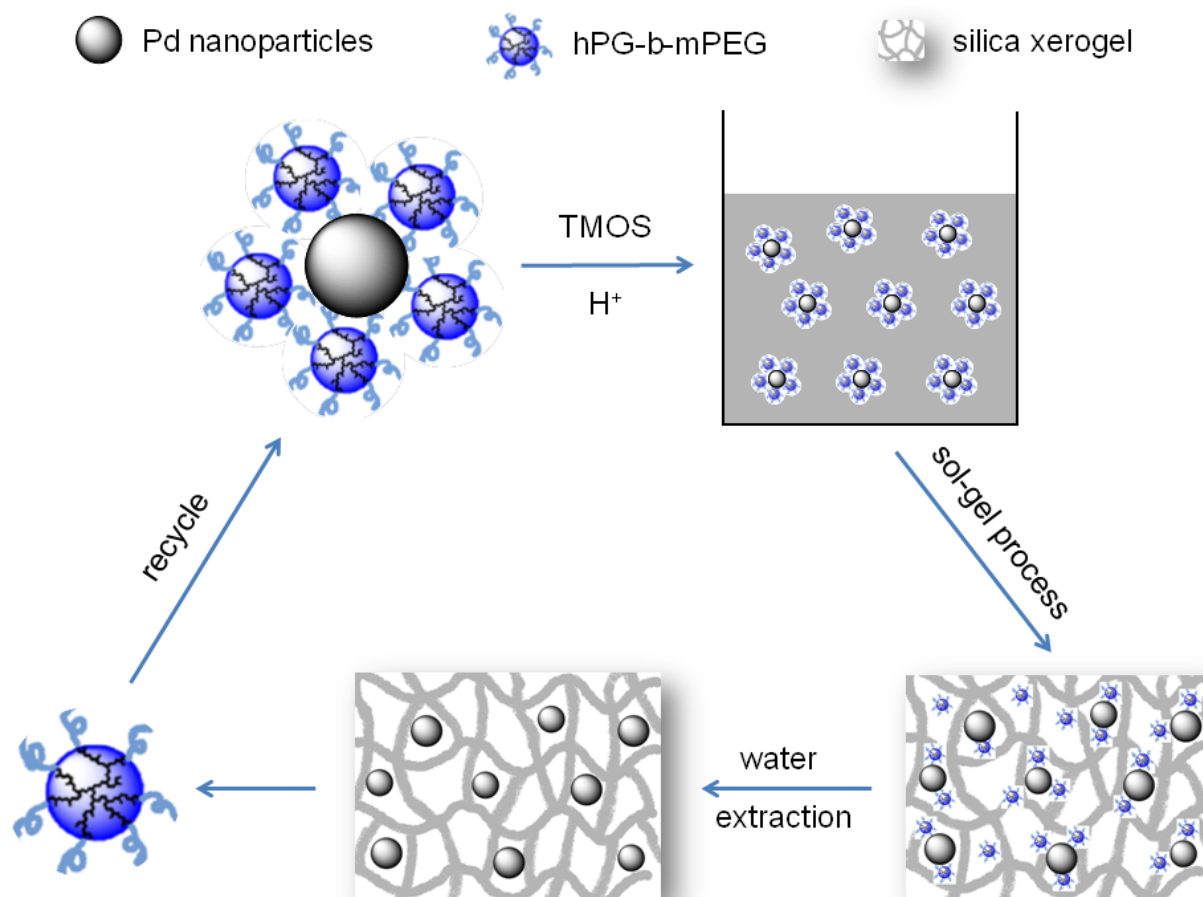


Figure 5.1 A schematic representation of the sol-gel process for immobilizing Pd NPs to a silica xerogel.

The key process for the stabilization of Pd NPs in the procedure is the coordination of Pd with a core-shell architected water soluble copolymer hPG-b-mPEG. It will be later shown that in the here presented process the copolymer hPG-b-mPEG does not influence the structure of the formed xerogel but is homogeneously dispersed into a silica monolith after condensation. This is different to the recently reported templating approach where the porosity of the silica was exclusively generated by the polymeric stabilizer.^{161,162}

It should be noted that the presence of hPG-b-mPEG stabilized Pd NPs sets certain demands on the sol-gel process. It is found that there is a competition between the hydrolysis of TMOS and the precipitation of Pd NPs. When the proton concentration is higher than 3.5 mol/L, the hydrolysis of TMOS dominates the process and Pd NPs are homogeneously distributed into the silica before they can precipitate. After adding the silica precursor to the acidified solution of the metal sol, the black solution shows fast increasing viscosity until it forms a gel with uniform gray color. In contrast, under lower acidic conditions, the precipitation of Pd NPs surpasses over the hydrolysis of TMOS, which is easily observed as the black solution become colorless and Pd precipitate to the wall of the flask, before a gel is being formed.

For a first evaluation of the effect of different pH values, two silica xerogel samples are prepared at the same temperature but under different acid concentrations, S1 in 5.0 mol/L and S2 in 3.6 mol/L, respectively. Figure 5.2A shows the nitrogen adsorption isotherms of the silica xerogels.

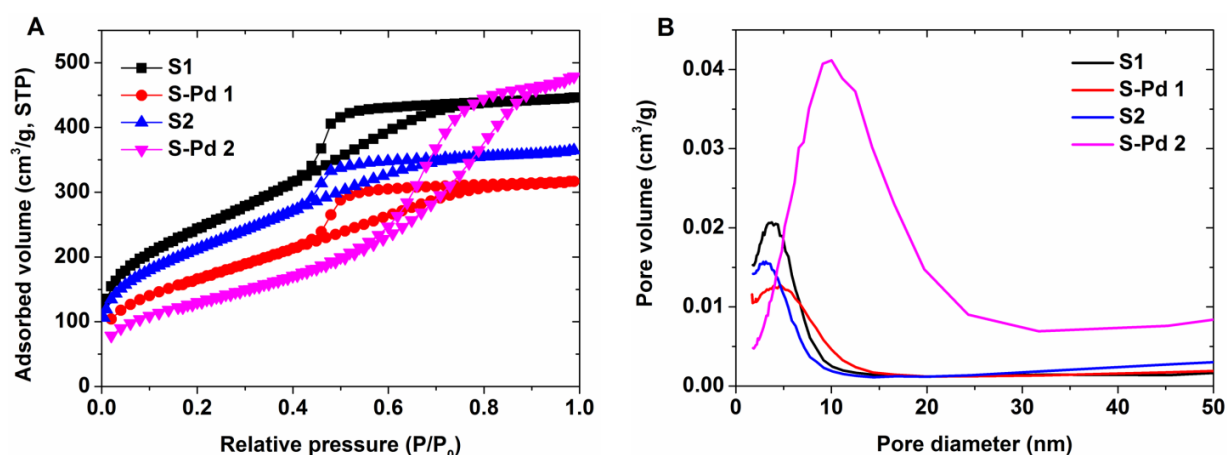


Figure 5.2 (A) Nitrogen adsorption isotherms and (B) BJH pore size distribution plots of 2 silica xerogels (S1 and S2 individually) and 2 Pd/silica xerogels (S-Pd 1 and S-Pd 2 individually).

Both samples exhibit mesopores with an average diameter of around 3.0 nm, and high BET surface area. Compared to the sample S2 with surface area of 753 m²/g, the sample S1 synthesized at higher acidic conditions shows higher surface area of 865 m²/g. The detailed information about the xerogels is presented in Table 4.

Table 4 Structural properties of silica xerogels and Pd/silica catalysts.

Sample name	[H ⁺] ^a (mol/L)	Pd content (wt%, ICP)	Surface area (m ² /g)	Pore diameter ^b (nm)
S1	5.0	---	865	3.6
S2	3.6	---	753	3.2
S-Pd 1	5.0	0.25	598	4.3
S-Pd 2	3.6	0.50	532	10.0
S-Pd 1 ^c	---	0.24	340	---

^aThe acid concentration during the sol-gel process,

^bAverage pore diameter from the BJH desorption branch,

^cThe catalyst S-Pd 1 after 10 runs of COD hydrogenation.

In the following study, two Pd/silica xerogels are prepared at different acidic conditions and different Pd loading, named as S-Pd 1 ([H⁺] = 5.0 mol/L, Pd loading 0.25 wt%) and S-Pd 2 ([H⁺] = 3.6 mol/L, Pd loading 0.50 wt%) respectively. To observe if the polymer stabilizer can be washed out completely, S-Pd 1 is analyzed by solid state NMR during the water extraction process. Figure 5.3 shows the ¹³C NMR spectra of the aqueous metal sol Pd/hPG-b-mPEG, as synthesized S-Pd 1 after 2 times and 3 times water extraction respectively.

The ¹³C NMR spectra of hyperbranched polyglycerol (hPG) show 7 main peak regions between 60 and 85 ppm.¹⁶³ In the solid state ¹³C NMR spectra, due to a lower resolution, not all peaks are observable. The ¹³C NMR spectra of linear PEG show a unique peak at δ 72 ppm,¹⁶⁴ which overlaps one of the peaks from hPG. In Figure 5.3, it is noticeable that during the washing

process, the peaks of hPG-b-mPEG are disappearing. After 3 times (3×15 min) washing, no peaks are observed, which means that the polymer is washed out completely by water extraction. The obtained polymer solution from extraction process can be reused for the next preparation of Pd sol.

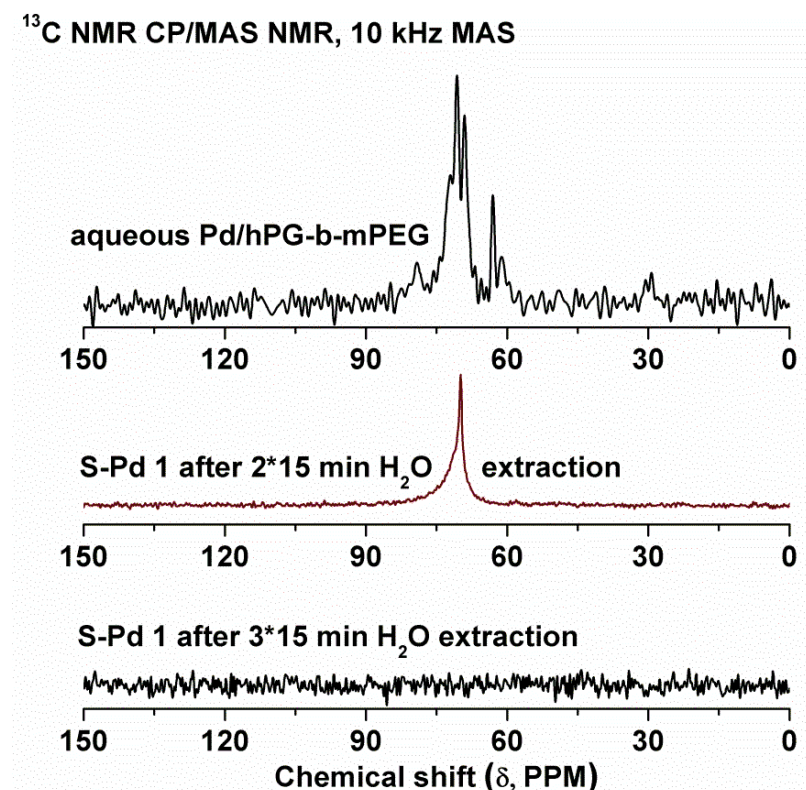


Figure 5.3 ^{13}C NMR spectra of Pd/hPG-b-mPEG, as synthesized S-Pd 1 after 2 times and 3 times water extraction respectively.

The nitrogen adsorption isotherms and pore size distribution of the Pd/silica xerogels are also shown in Figure 5.2. Compared to the silica xerogels, the Pd/silica xerogels show a lower surface area of 500-600 m^2/g . On one hand, the loading of Pd increases the density therefore decreases the gravimetric surface area of the obtained xerogel; on the other hand, the possible interaction between the OH groups on hPG-b-mPEG and TMOS disturbs the gelation of TMOS and therefore decreases the specific surface area of the obtained xerogel. With 0.25 wt% of Pd loading, the Pd/silica xerogel possesses a very similar porous structure as the pure silica xerogel

prepared under the same acidic conditions. However, when the loading of Pd increase to 0.50 wt%, both the surface area and the average pore size of the xerogel significantly change, due to a relatively high Pd loading. The structural properties of all the prepared xerogels are summarized in Table 4. The stability of Pd NPs during the catalyst preparation and the catalytic application is confirmed by TEM measurements, shown in Figure 5.4.

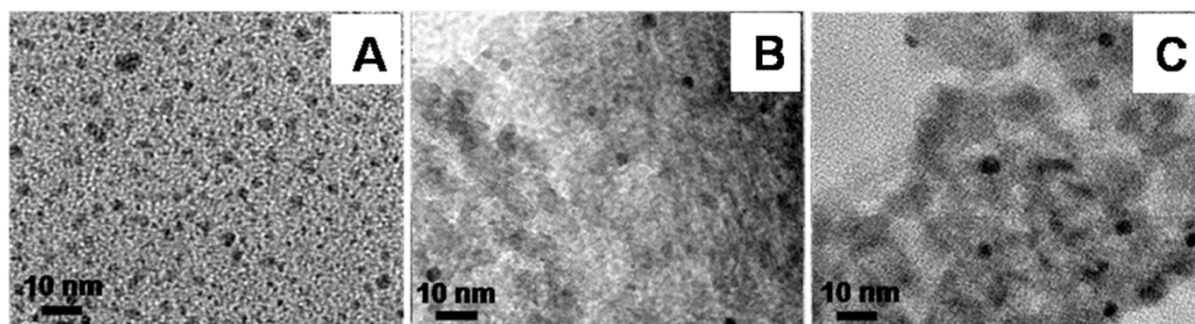


Figure 5.4 TEM images of Pd NPs in (A) hPG-b-mPEG aqueous solution, (B) S-Pd 1, (C) S-Pd 2.

Figure 5.4A shows the TEM image of an aqueous solution of Pd NPs stabilized by hPG-b-mPEG. One can see that Pd NPs are well dispersed in the aqueous polymer solution with the diameter of 3-6 nm, due to the stabilization of the PEG chain. Figure 5.4B and 5.4C are the TEM images of the Pd/silica xerogels S-Pd 1 and S-Pd 2 respectively. The TEM images show that the loading concentration of Pd influences its particle size. The sample S-Pd 1, with 0.25 wt% Pd loading, shows a good dispersion with similar Pd particle size as the aqueous solution of Pd/hPG-b-mPEG. In contrast, the sample S-Pd 2, with 0.5 wt% Pd loading, shows larger particles with the size of 4-8 nm.

5.1.2 Catalytic application of silica xerogel supported Pd catalysts

In order to evaluate the reactivity of the Pd/silica xerogel catalysts, we have studied the hydrogenation of COD with these catalysts. The kinetics of the hydrogenation reaction is recorded for the catalysts S-Pd 1 and S-Pd 2, shown in Figure 5.5. It is seen that both catalysts show similar reactivity in the reaction, but S-Pd 1 presents a slightly higher activity which is due

to a higher surface area of the xerogel and a better dispersion of Pd NPs. It is not surprising that with the reaction time the rate of reaction decreases since the concentration of the reactant COD is decreasing. In order to avoid the further conversion of cyclooctene to cyclooctane, the reaction is stopped when COD conversion reached about 90%.

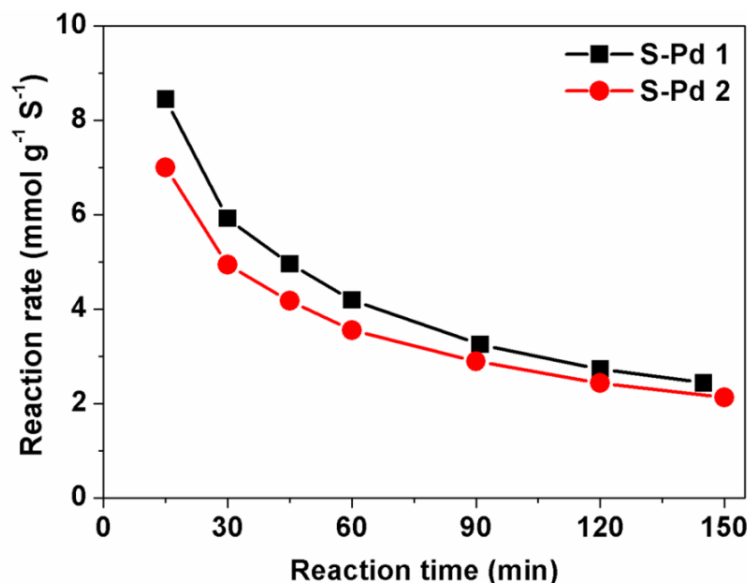


Figure 5.5 Reaction rate of the Pd/silica xerogels S-Pd 1 and S-Pd 2 in hydrogenation of COD reaction. (Note that the reaction rate is calculated basing on the overall amount of Pd.)

In a further study, S-Pd 1 is compared to the homogeneous Pd/hPG-b-mPEG catalyst of solution and 2 commercial heterogeneous catalysts, noted as Pd/activated carbon powder (Pd/AC, 5 wt% of Pd loading) and Pd/Al₂O₃ pellets (0.5 wt% of Pd loading, an egg-shell catalyst with 100 μ m active layer). Figure 5.6 presents the kinetics of the hydrogenation reaction with these 4 catalysts. The homogeneous catalyst Pd/hPG-b-mPEG solution exhibits the highest activity. Among the other three solid catalysts, Pd/Al₂O₃ shows lowest activity probably due to the large Pd particle size. After 30 min reaction, S-Pd 1 and Pd/AC show comparable reaction rate as the homogeneous catalyst Pd/hPG-b-mPEG, indicating the high activity of Pd NPs from these two solid catalysts.

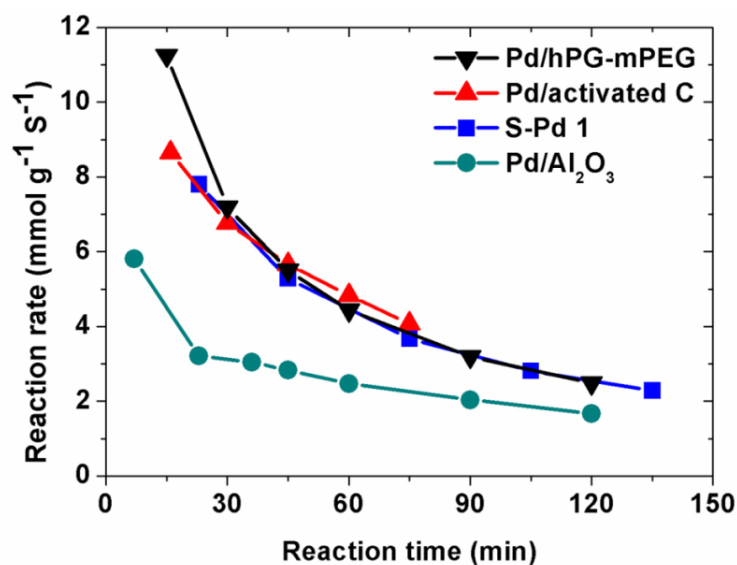


Figure 5.6 Reaction rate of 4 catalysts: Pd/hPG-b-mPEG, S-Pd 1, Pd/Al₂O₃ and Pd/AC in COD hydrogenation reaction. (Note that the reaction rate is calculated basing on the overall amount of Pd.)

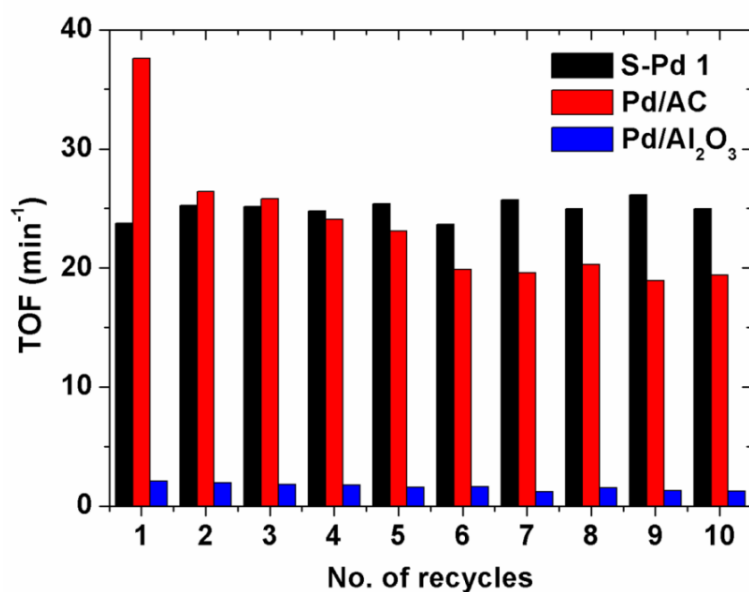


Figure 5.7 Recycling of S-Pd 1, Pd/Al₂O₃ and Pd/AC in the hydrogenation of COD.

The detailed information about the long term stability of these catalysts is obtained from recycling reactions. Figure 5.7 presents the turnover frequency as a function of the number of cycles. It must be mentioned that, in spite of high activity, Pd/ hPG-b-mPEG could not be

applied for recycling experiments, due to the infeasible separation. As for Pd/AC, since it is in the shape of fine powder, it precipitates very slowly from the solution so that it is most time consuming and durable during the recycling. Both S-Pd 1 and Pd/Al₂O₃ are separated from the system easily for further recycling. The recycling reactions are investigated under identical conditions over the catalysts S-Pd 1, Pd/Al₂O₃ and Pd/AC. The mass of Pd is equal for all these 3 catalysts.

From the recycling results, Pd/Al₂O₃ shows much lower TOF than S-Pd 1 or Pd/AC. For this catalyst the TOF decreases from 2 (in the first reaction) to 1.2 (after 10 hydrogenation recycles), which indicates a decreasing activity. Pd/AC exhibits higher TOF than S-Pd 1 during the first three runs. However the TOF dramatically drops during the recycling runs, which can be explained by fast deactivation. In contrast, S-Pd 1 shows constant TOF with just a slight fluctuation during the whole recycling experiments. After 4 runs, S-Pd 1 already has a higher TOF than Pd/AC. It can be therefore concluded that although Pd/AC is a highly active catalyst, the poor stability obstruct its performance. In contrast, S-Pd 1 shows an extraordinary stability as well as activity, which indicates that Pd NPs are stably dispersed on silica xerogel.

In order to follow the change of Pd NP size during catalytic applications, TEM measurements are obtained with the catalyst S-Pd 1 after recycling. Figure 5.8 shows the TEM images of S-Pd 1 after 2 runs (Figure 5.8A) and after 10 run (Figure 5.8B). Compared to the TEM image of S-Pd 1 before the reaction (Figure 5.4B), the particle size of Pd indeed increases to 10-20 nm, but remains constant after another 8 recycles, which indicates that the Pd NPs are stable during the recycling.

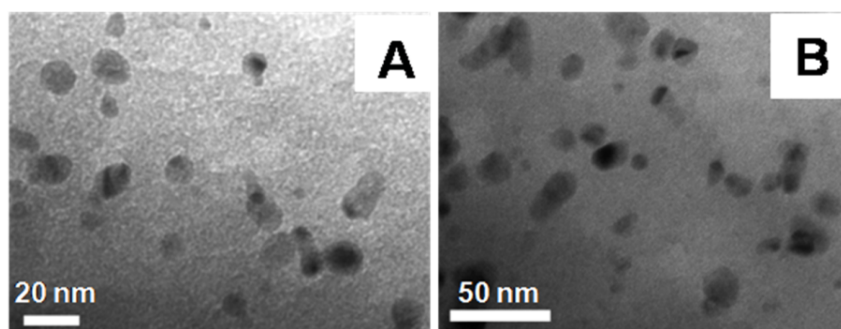


Figure 5.8 TEM images of the sample S-Pd 1 after catalytic recycles (A) after 2 runs and (B) after 10 runs.

The results from ICP measurements of S-Pd 1 are also in accordance to the TEM images, that is, the concentration of Pd keeps constant after 10 runs of the hydrogenation reaction. Thus the here presented catalyst is indeed highly active and stable as the immobilization of Pd NPs on the silica xerogel prevents leaching of the metal during the catalytic reactions.

5.1.3 Conclusion

A mesoporous silica xerogel supported Pd NPs is synthesized by a simple sol gel process. Herein a preformed sol of Pd NPs stabilized by a water soluble polymer hPG-b-mPEG is used for the synthesis. Because of the interconnectivity of the pores, the stabilizer hPG-b-mPEG can be washed out easily by ultrasonication and therefore be recycled, which is highly economical. In a specific pH range the sol-gel process ensures uniform Pd stabilization and yields xerogels with high surface area (up to 600 m²/g). The Pd NPs are immobilized stably in the silica monolith, which is confirmed by the TEM images and the ICP-MS data of this xerogel catalyst. During the recycling experiments, no particle sintering or catalyst deactivation is observed. The Pd NPs remain in the same size range between 10 to 20 nm after the recycling runs. Furthermore, ICP analysis shows that the concentration of Pd is constant during 10 runs of recycling. This xerogel catalyst shows comparable reactivity and selectivity to the homogeneous catalyst Pd/hPG-b-mPEG in the hydrogenation of COD, which is much higher than the commercial catalyst Pd/Al₂O₃. This observation demonstrates that the Pd NPs maintain the activity after immobilization in the silica xerogel. During the simple one pot synthesis, only minimal energy is consumed and no mass loss is caused, which is an important prerequisite for up-scaling the synthesis of the catalyst. Besides the simpleness and economic benefit of the synthesis, the high reactivity and stability make the catalyst extraordinarily interesting for industrial application.

5.2 Ultra high surface area SBA-15 supported Pt NPs for hydrogenation reactions

SBA-15 has received a lot of attention since it was first reported, and it is now one of the most widely used supports in catalysis, due to its easy accessibility and excellent textural properties, such as high surface area, ordered pore structure, controllable pore size, high thermal stability, etc. As the surface of SBA-15 is relatively inert, it is difficult to directly graft metal NPs on it. Hence, additives or surfactants are often used to functionalize the SBA-15 surface before grafting the metal NPs, and their deposition on the surface is usually carried out by a post-synthesis method.^{138,139,165,166} This leads to formation of NPs lacking uniformity in size and shape. Furthermore, the interaction between NPs and the support is not strong enough, and some NPs can agglomerate^{167–170} or leach out^{171–173} during reactions. This is true in particular for NM catalysts.

Recently, some efforts were made for in-situ incorporation of NMNPs into the SBA-15 structure.^{141,166,167} Richards et al¹⁷⁴ succeeded to confine Au NPs on the pore walls of SBA-15 by adding HAuCl₄ solution directly to the synthesis process. However, the sample showed irregular shapes and pores; Somorjai et al¹⁴⁹ reported that Pt with particle size ranging from 1.7 nm to 7.0 nm can be deposited on SBA-15 in the presence of PVP, whereas the synthesis process is complicated and severe conditions are required. Furthermore, the surface area and/or the pore size of the sample prepared significantly decreased when compared to the pure SBA-15. This leads to a negative effect on catalytic reactions, where surface area or pore size plays an important role.

In this project, Pt NPs are immobilized on SBA-15 by a one-pot synthesis. PVA is used in the synthesis process to stabilize in-situ formed Pt NPs. It is found that besides being a stabilizer, PVA can create additional mesopore connectivity in the structure, enhancing the surface area, while maintaining the same mesopore size. This is totally different from findings reported by other authors,^{149,175–177} who reported that the surface area of SBA-15 always decreased after the addition of Pt, no matter what the used additional agent was. The obtained catalyst Pt/SBA-15 is applied for gas-phase CO oxidation and also for liquid-phase COD hydrogenation. The following chapter will show the synthesis method and catalytic performance of this type of catalyst.

5.2.1 Synthesis and characterization of SBA-15 materials

The pure SBA-15 is synthesized using a similar procedure as reported elsewhere.¹⁷⁸ Based on the reported method, additional PVA is used in our approach. It is expected that PVA creates micropores between the mesoporous channels in SBA-15 therefore enhance the connectivity of these channels. Moreover, in the next step, PVA is used as a stabilizer of a Pt sol during the sol-gel process to immobilize Pt NPs on SBA-15.

To the reaction mixtures a freshly prepared 1 wt.% aqueous PVA ($M_w = 130,000$ g/mol) solution is added in different amounts. Depending on the amount of PVA added, the samples are named SBA-15-V (“V” is the volume ratio of PVA/TOES). Also, when referring to the aging temperature, the samples are named as SBA-15-V-T. For example, “SBA-15-3-100°C” means that SBA-15 is synthesized with 3 ml 1 wt.% PVA and 1 ml TEOS and is aged at 100 °C for 24 h. All the samples are calcined at 500°C for 4 h to remove the template completely.

Figure 5.9 shows the XRD patterns of the samples synthesized with different amount of PVA. All patterns show an intensive peak at $2\theta = 0.8 \sim 0.9$ that corresponds to the (100) diffraction of the 2D hexagonal structure of SBA-15, indicating the presence of an ordered pore structure and $d(100)$ values of 10.0-10.9 nm. The well-resolved (110) and (200) diffraction peaks indicate that there is no substantial change in the pore structure of the samples after PVA was added.

The ordered pore structure of the samples is further proven by TEM measurements, as shown in Figure 5.10. The samples possess well-ordered hexagonal arrays of mesopores, whether PVA is added or not. Thus it can be stated that the addition of PVA does not influence or even deteriorate the order of the pluronic-silica composite.

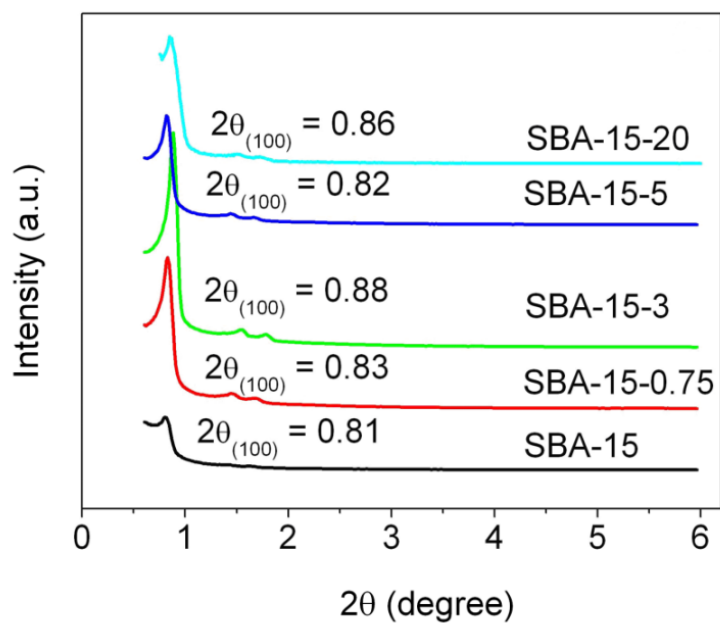


Figure 5.9 X-ray diffraction patterns of SBA-15 synthesized with different amount of PVA. Aging temperature for all the samples is 100°C.

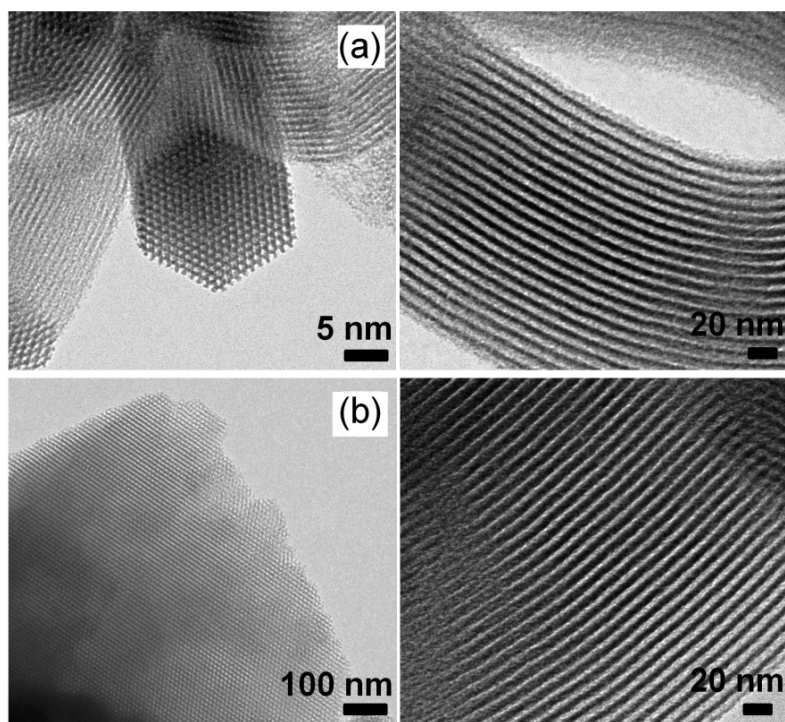


Figure 5.10 TEM images of (a) SBA-15, synthesized without PVA and (b) SBA-15-3, with PVA.

The nitrogen-adsorption isotherms of the samples synthesized with different amounts of PVA are presented in Figure 5.11(a). The corresponding porous characteristics are listed in Table 5. All samples show a defined step with a hysteresis loop corresponding to the filling of mesopores with narrow pore size distributions. The BET isotherms show the surface area of 877 m²/g and total pore volume of 1.15 cm³/g for SBA-15, of 1177 m²/g and 1.43 cm³/g for the sample SBA-15-3, respectively. However, despite the increase in surface area (~34%) and porosity (~24%), the pore size of the mesopores generated from the block-co-polymer P123 is almost unvaried based on the BJH method on the adsorption branch (shown in Figure VIII in Appendix A.).

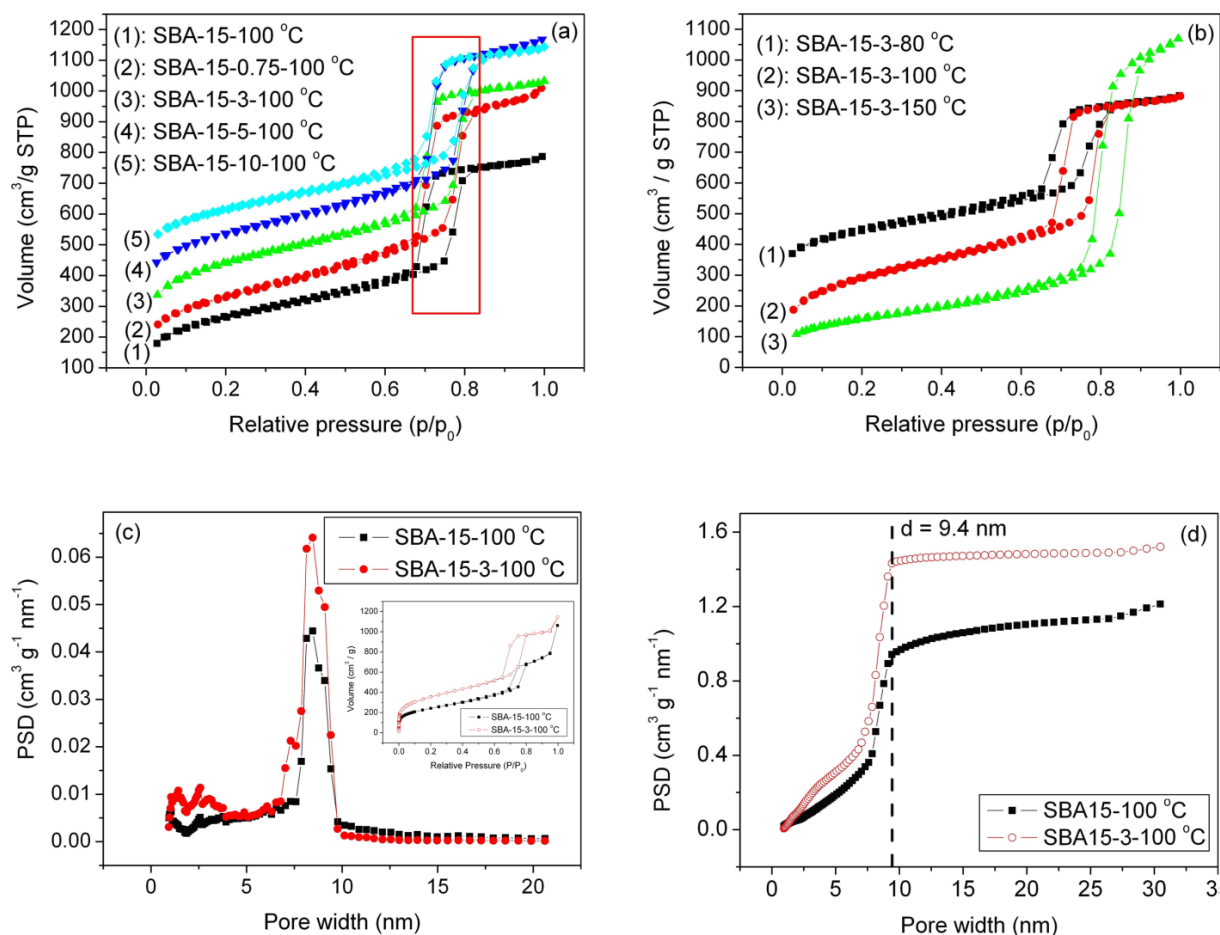


Figure 5.11 (a) and (b): Nitrogen adsorption isotherms for SBA-15-100 °C synthesized with different PVA contents and aging temperatures; (c) Pore size distribution derived from the BET isotherms with micropore analysis (inset) and (d) cumulative pore volume for SBA-15 and SBA-15-3-100 °C (both obtained using the NLDFT method).

Further increase of the PVA content does not yield further significant enhancement of the surface area or the pore volume. It can be concluded that the addition of PVA does not influence the mesopores created by polymer P123, thus the increase of surface area and porosity must be due to the creation of additional smaller pores. To prove this, nitrogen adsorption isotherms for SBA-15-100°C and SBA-15-3-100°C with additional micropore analysis are carried out. Pore size distribution and cumulative pore volume (obtained from non-local density functional theory, NLDFT) shown in Figure 5.11(c) and (d) indicate that there are indeed new, smaller pores created in sample SBA-15-3-100 °C.

Table 5 Textural properties of SBA-15 synthesized under different conditions.

Sample	SA (m ² /g) ^a	Pa (nm) ^b	PV (cm ³ /g) ^c
SBA15-100 °C	877	9.7	1.15
SBA15-0.75-100 °C	986	9.7	1.48
SBA15-3-100 °C	1177	9.7	1.43
SBA15-5-100 °C	1124	9.7	1.58
SBA15-10-100 °C	1182	9.7	1.49
SBA15-3-80 °C	1248	8.7	1.41
SBA15-3-150 °C	555	14.8	1.64

^a SA, Surface area, calculated by BET method,

^b Pa, Pore size, calculated from the adsorption branch,

^c PV, Pore volume, calculated at $p/p_0 = 0.99$.

The effect of aging temperature on the structural properties of SBA-15-3 is also investigated and the results are shown in Figure 5.11(b) and Table 5. One can see that the surface area increases and the pore size of SBA-15-3 decreases with decreasing temperature. As suggested by Galarneau et al.¹⁷⁹, this phenomenon is due to the aggregation of the PEO chains. However, this

effects achieves the peak at 80 °C and a further lower temperature (e.g. 60 °C) yields materials with lower surface areas (Figure IX in Appendix A.), which is explained by to the hydration of the PEO chains.¹⁷⁹

To verify that PVA can be used as a template to create porous silica, a silica sample is prepared using exclusively PVA as porogen, while all other preparation conditions are unchanged. It should be noted that for this control experiment a much higher amount of PVA is required (13 ml 1 wt.% PVA to 1 ml TEOS) to obtain an interconnected pore system.

The nitrogen adsorption and pore size distribution of obtained silica are presented in Figure 5.12. One can see that mesoporous silica with a pore size of ~ 5.6 nm was formed in this sample. These pores are rather big and are certainly absent in SBA-15-V samples prepared with the mixed templates of P123 and PVA. Regarding the big size, the pores cannot be created by a template of single PVA chains. Instead, replication of strands of PVA aggregates is much more likely. A similar behavior was observed when pure PEO polymers was used as templates for porous silicas.¹⁸⁰

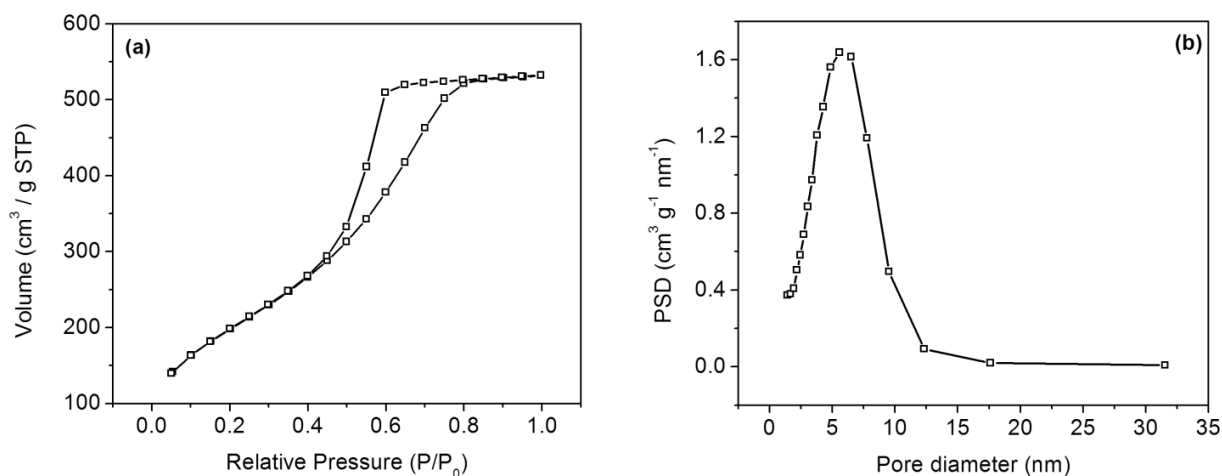


Figure 5.12 (a) Nitrogen adsorption isotherms (b) the corresponding pore distribution of as synthesized silica with the template PVA.

The additionally created porosity of SBA-15-V samples indicates that the micelles of P123 do not mix with PVA, even though both polymers are hydrophilic and water soluble, therefore PVA

contributed to the additional porosity. It has been reported that aqueous blends of PEO and PVA are immiscible with weak interactions between the polymers,¹⁸¹ however PVA/PEO cast films from aqueous blends show phase separation,¹⁸² which supports the here presented idea of the formation of a second porosity in our SBA-15 materials. The role of PVA in the synthesis of SBA-15 reported in this work can be simply illustrated by Figure 5.13.

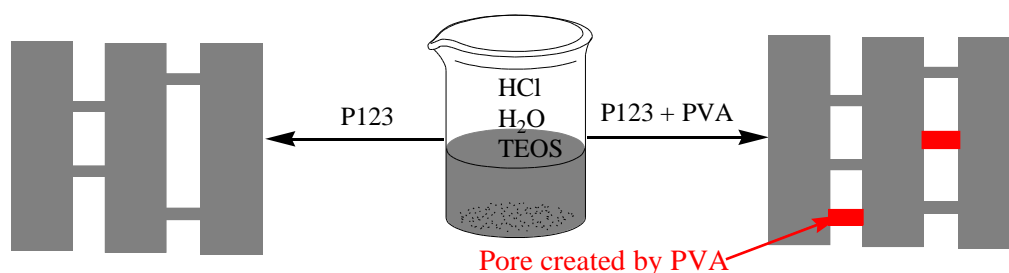


Figure 5.13 Scheme of the role of PVA in the formation process of SBA-15.

5.2.2 Synthesis and characterization of Pt@SBA-15 catalyst

As discussed above, PVA is used as a template to create secondary porosity to enhance the connectivity of the channels in SBA-15 materials. Besides of being a template, PVA also can be used as a stabilizer for the preparation of a metal sol and therefore to avoid metal NP agglomeration during the following sol-gel process. In this work, a catalyst of Pt NPs immobilized onto SBA-15 is obtained by employing a Pt sol stabilized by PVA. During the synthesis, a metal sol is prepared first by reduction of H_2PtCl_6 in presence of PVA solution. Instead of the pure PVA solutions, the obtained metal sol is added to the preparation of SBA-15. The same amount of PVA as the sample SBA-15-3 is used in the metal sol. A SBA-15 sample loaded with 0.3 wt% Pd is prepared, named 0.3%Pt@SBA-15. The obtained sample 0.3%Pt@SBA-15 is analyzed by ICP-MS and the concentration of Pt is 0.29 wt.%.

With a conventional method, after loading NMNPs, often the surface area of SBA-15 decreases significantly.^{183–185} However, this is not the case with the sample 0.3%Pt@SBA-15. The N_2 sorption isotherms in Figure 5.14 show that the surface area of 0.3%Pt@SBA-15 reaches $1137 \text{ m}^2/\text{g}$. As mentioned in chapter 5.3.1, the surface area of SBA-15-3 is $1177 \text{ m}^2/\text{g}$. Surprisingly,

after loading 0.3 wt.% Pt, there is no big change of the surface area. Moreover, no change in the pore size is observed. TEM images of 0.3%Pt@SBA-15 in Figure 5.15 show that Pt NPs are homogeneously dispersed on the support SBA-15, with a mean particle size of ~ 8 nm.

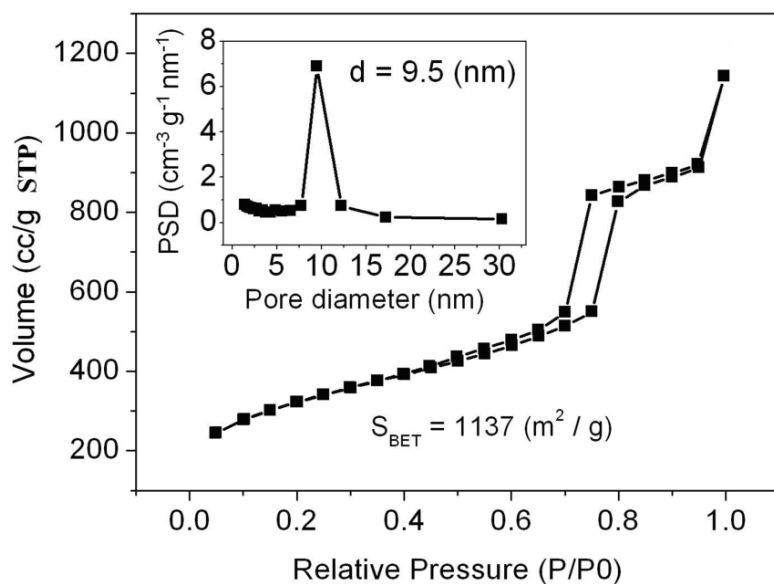


Figure 5.14 N₂ sorption isotherms and pore size distribution of the catalyst 0.3%Pt@SBA-15.

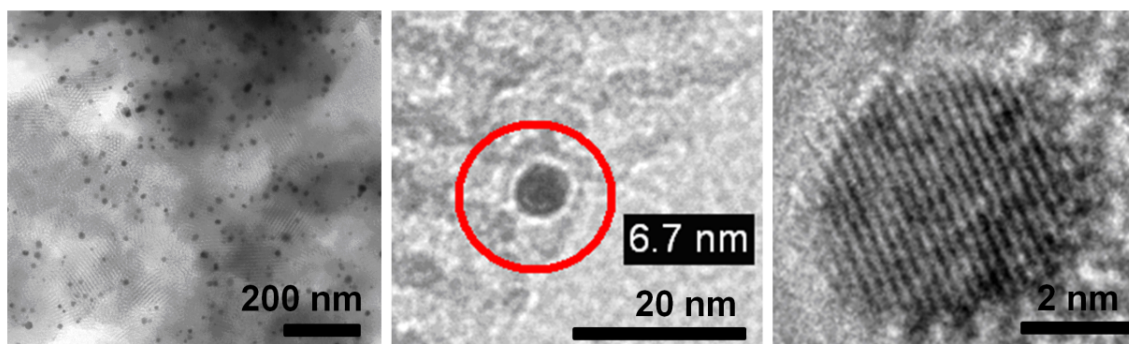


Figure 5.15 TEM images of the catalyst 0.3%Pt@SBA-15.

5.2.3 Catalytic application of Pt@SBA-15 catalyst

A series of Pt catalysts with different Pt loading are synthesized by the one-pot synthesis described above. Since a high Pt loading could disturb the formation of an ordered pore structure of SBA-15, the concentration of Pt is confined between 0.2 to 2.0 wt.%. The same concentration of PVA (the volume ratio of PVA/TEOS is 3) is employed for all Pt@SBA-15 catalysts preparation, to obtain similar surface area of SBA-15.

In order to investigate their catalytic performance, these Pt catalysts are applied for both gas phase CO oxidation reaction and liquid phase COD hydrogenation reaction. Figure 5.16 shows screening results of CO oxidation over SBA-15 with varied Pt loading (from 0 to 2.0 wt.%). The sample SBA-15 without Pt loading is also tested in this screening experiment. From Figure 5.16, one can find that all the Pt catalysts show no activity below 200 °C. Besides, the catalyst 0.2% Pt@SBA-15 shows similar catalytic performance as pure SBA-15. Their activity starts increasing dramatically above 300 °C, except that with the former catalyst CO conversion achieves full conversion at 350 °C. In contrast, with SBA-15, CO conversion has not achieved full conversion until reaction temperature at 400 °C. The catalysts 0.5%, 1.0% and 2.0% Pt@SBA-15 show almost identical catalytic behavior and CO conversion achieved full conversion below 300 °C.

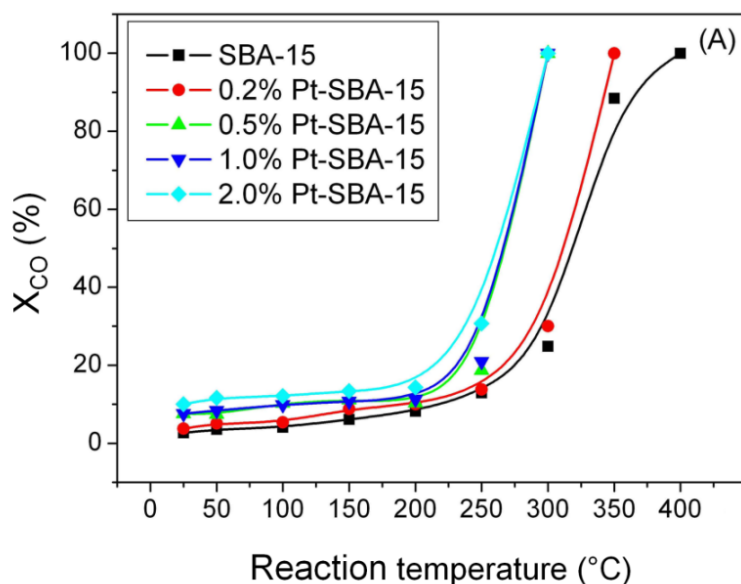


Figure 5.16 A screening experiment of CO oxidation, CO conversion as a function of reaction temperature over Pt@SBA-15 with varied Pt loading and pure SBA-15.

To obtain information about the catalytic stability, a LTM of CO oxidation is performed with the catalyst 0.5%Pt@SBA-15, shown in Figure 5.17. In order to avoid the full CO conversion, the reaction temperature of the LTM is set to 290 °C. It is obvious that CO conversion keeps constant at 80% during the whole reaction time of 15 h, indicating a high stability of 0.5% Pt@SBA-15.

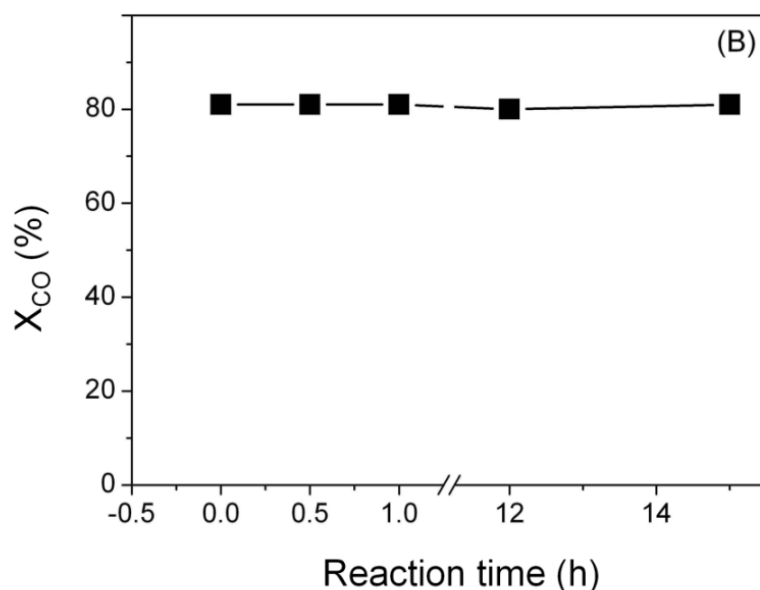


Figure 5.17 A LTM at 290 °C, CO conversion as a function of reaction time over the catalyst 0.5%Pt@SBA-15.

Besides being applied in the gas phase CO oxidation reaction, the catalyst 0.5%Pt@SBA-15 is also investigated in a liquid phase reaction, the hydrogenation of COD in heptane as solvent. This hydrogenation reaction over Pt@SBA-15 catalysts proceeds fast and conversion of COD achieves 90% after 30 min reaction, therefore the screening results are not presented. Figure 5.18 is the recycling results of COD hydrogenation over the catalyst 0.5%Pt@SBA-15. The conversion of COD keeps constant over 6 runs. It is noted that the reaction is stopped before the full conversion of COD in order to avoid over hydrogenation of COD to cyclooctane. Similar as in CO oxidation reaction, the catalyst shows high stability in COD hydrogenation reaction, suggesting a good reusability of the catalyst Pt@SBA-15 for different catalytic applications.

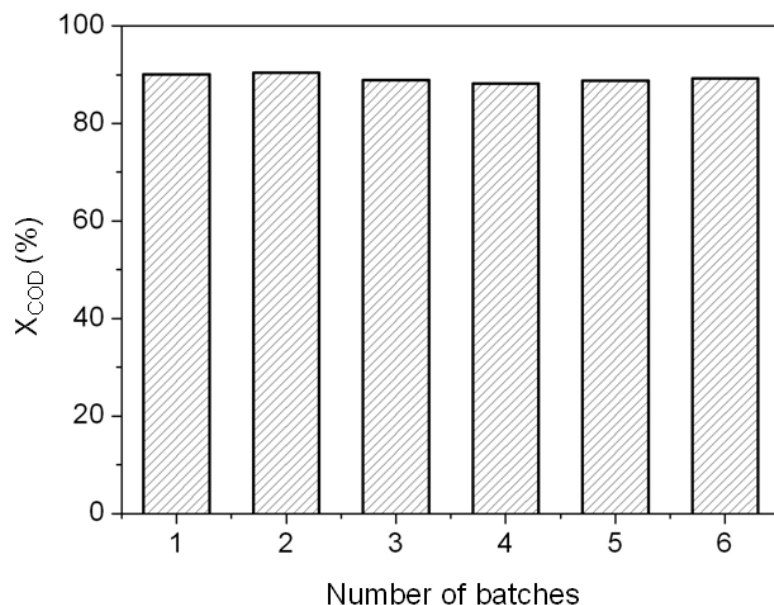


Figure 5.18 Recycling of COD hydrogenation over the catalyst 0.5%Pt@SBA-15. Reaction conditions: 1g catalyst + 1.13 ml COD + 60 ml heptane (solvent), 70 °C, P_{H_2} = 1.1 bar, reaction time 35 min.

To check if any structural changes occur to the catalyst during catalytic applications, 0.5%Pt@SBA-15 after reactions is analyzed by BET, XRD and TEM, and compared to the as synthesized catalyst. Figure 5.19 shows that there is no significant change both on the surface area and pore size distribution of 0.5%Pt@SBA-15 before and after CO oxidation application. The minor difference found in the surface area is within the experimental error (< 5%). However, a slight decrease of the surface area and pore size is detected after COD hydrogenation application.

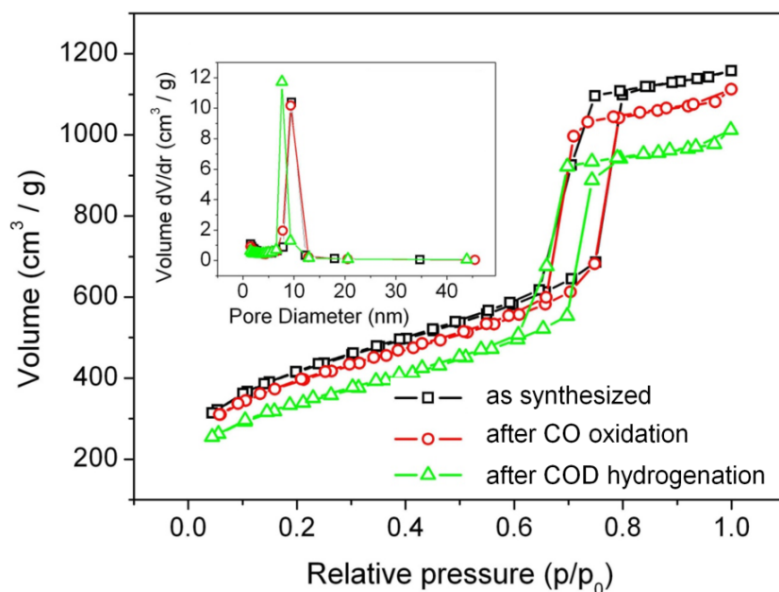


Figure 5.19 N_2 adsorption isotherms and the corresponding pore size distributions of the catalyst 0.5%Pt@SBA-15 as synthesized, after CO oxidation and after COD hydrogenation application separately.

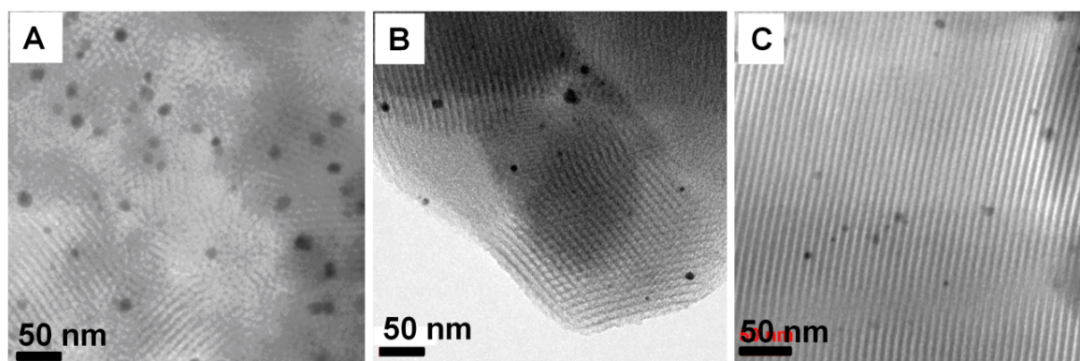


Figure 5.20 TEM images of the catalyst 0.5%Pt@SBA-15 (A) as synthesized; (B) after CO oxidation and (C) after COD hydrogenation application separately.

TEM images of the catalyst 0.5%Pt@SBA-15 as synthesized, after CO oxidation and after COD hydrogenation application are respectively shown in Figure 5.20. The highly ordered structure of this catalyst states that the porous framework of SBA-15 is intact during the reactions. Furthermore, the size of Pt NPs shows no observable increase after catalytic applications, even after the gas phase CO oxidation performed at 300 °C. When NMNPs catalysts are applied in liquid phase reactions, metal leaching is often a severe problem causing catalyst deactivation.

This is not the case with the catalyst 0.5%Pt@SBA-15. After COD hydrogenation reaction, this catalyst is analyzed by ICP, and the concentration of Pt shows no change, indicating that no Pt leaching occurred during the reaction. Therefore, it can be concluded that the here synthesized Pt@SBA-15 catalyst is highly stable as well as active.

5.2.4 Conclusion

A significant improvement on the porosity of SBA-15 by using amounts of PVA is achieved. Without changing the size or architecture of mesopores, the surface area is enhanced from 877 m²/g (without PVA) up to 1177 m²/g (with PVA). This can be explained by the formation of additional pores created by the PVA template, connecting the larger mesopores formed from the P123 template. Besides being a template, PVA can be further used to stabilize metal NPs. SBA-15 supported Pt NPs are obtained through a facile one-pot synthesis, by adding a preformed Pt sol stabilized by PVA. Compared to pure SBA-15, the surface area of this catalyst is improved, while the mesostructure and pore size are unchanged. This high surface area Pt@SBA-15 catalyst shows highly activity and stability during catalytic applications. Due to the high dispersion and firm immobilization of Pt NPs onto SBA-15, this catalyst shows no aggregation at high temperature gas phase CO oxidation and no Pt leaching in liquid phase COD hydrogenation reactions.

6. Summary and conclusion

Several one-pot approaches are applied to synthesize MONPs and NMNPs for catalytic applications. Through simple and up scalable one-pot approaches, NiMnO nanocrystallites supported on amorphous silica are obtained and applied for the DRM reaction, Pd NPs immobilized on silica xerogel are synthesized and tested for the hydrogenation of COD, Pt NPs immobilized on SBA-15 are synthesized and tested for both oxidation of CO and hydrogenation of COD reactions. By tuning the conditions of preparation methods and the structure of the materials, the catalytic properties of the obtained nanocatalysts are optimized for industrial applications.

Chapter 4 describes the 1st part of my PhD work, *amorphous silica supported NiMnO nanocrystallites for the DRM reaction*. There is a project from UniCat (Unifying of Catalysis), to combine the OCM and DRM process. The concept is to use the heat generated from highly exothermic OCM reaction, unreacted CH₄ and the main side product CO₂ from this reaction can convert to syngas, which is the DRM reaction. The combined process will be efficiently energy saving and also chemical saving. Considering the energy loss during the heat transfer, it is only practical that the DRM reaction proceeds at lower temperature than the OCM reaction. Therefore, my goal is to design a suitable Ni catalyst for low temperature DRM reaction (500 ~ 600 °C). Unfortunately, most of Ni catalysts exhibit little or no activity below 600 °C yet. In addition, the Boudouard reaction is favorable at low temperatures and therefore causes surface carbon deposition and catalyst deactivation. Therefore, it is crucial for a catalyst to activate the DRM reaction and meanwhile inhibit the Boudouard reaction at low temperatures. Considering the SMSI between Ni and MnO, the possible formation of a solid solution Ni_xMn_{1-x}O with varied Ni and Mn compositions, the strong CO₂ adsorption property of MnO, and the abundant resource of Ni and Mn, we choose a solid solution catalyst Ni_xMn_{1-x}O as the model catalyst for the DRM reaction applications.

By using conventional co-precipitation method with reactant NaHCO₃, a solid solution Ni_{0.2}Mn_{0.8}O with a high surface area (up to 170 m²/g) and mesoporous structure is obtained. This catalyst shows impressive activity in the DRM reaction. At 400 °C with a high GHSV value of 80 L h⁻¹ g⁻¹, Ni_{0.2}Mn_{0.8}O catalyst has been activated and already achieved TDE between 500-550 °C,

which prevails over the catalytic performance of any reported non-noble-metal catalysts. The occurred deactivation of the bulk catalyst is caused by particle sintering or agglomeration. The concentration of Ni has also influence on the catalytic behavior of this type of catalyst. Among a series of $\text{Ni}_x\text{Mn}_{1-x}\text{O}$ samples, $\text{Ni}_{0.1}\text{Mn}_{0.9}\text{O}$ shows the best catalytic performance.

After optimization, porous silica supported $\text{Ni}_{0.2}\text{Mn}_{0.8}\text{O}$ catalyst is obtained by a simple one-pot approach which is a combination of co-precipitation and sol-gel process. Due to the combining approach, $\text{Ni}_{0.2}\text{Mn}_{0.8}\text{O}$ is highly dispersed on porous silica and nanocrystallites of NiMnO with the size of ~ 10 nm are formed. Owing to the high dispersion and small size of NiMnO nanocrystallites, Ni^0 is fast and easily formed on the surface of the oxide therefore $\text{Ni}_{0.2}\text{Mn}_{0.8}\text{O}/\text{SiO}_2$ shows extraordinary activity for the DRM reaction. Compared to the bulk $\text{Ni}_{0.2}\text{Mn}_{0.8}\text{O}$, $\text{Ni}_{0.2}\text{Mn}_{0.8}\text{O}/\text{SiO}_2$ catalyst exhibits improved stability as well as activity. The latter one is stable at 500°C and no deactivation is observed after 60 h running. Only a neglectable amount of surface carbon (0.21 wt.%) is detected. When the reaction temperature increases to 550°C , this catalyst shows deactivation due to Ni^0 cluster sintering.

It is found that between $575\text{--}600^\circ\text{C}$, carbon deposition can be effectively suppressed due to the similar rates of methane decomposition and the Boudouard reaction; the phase transition from $\text{Ni}_{0.2}\text{Mn}_{0.8}\text{O}$ to Mn_2SiO_4 and $\text{Ni}_\alpha\text{Mn}_\beta\text{O}_8$ is also able to be avoided, therefore the catalyst shows the best performance. The advantages of economical materials, simple synthesis, large scalability and the distinctive catalytic performance bring a high potential to the NiMnO catalyst for industrial applications.

Chapter 5 describes the 2nd part of my PhD work, which is about immobilizing NMNPs catalysts onto porous silica materials for catalytic applications. Chapter 5.1 is about the synthesis of silica xerogel supported Pd NPs for catalytic applications. In this project, a silica xerogel supported Pd NPs catalyst is obtained through a one-pot approach. During the synthesis, a core-shell architected polymer hPG-b-mPEG is used to stabilize preformed Pd NPs, therefore the particle agglomeration during the immobilization process can be effectively suppressed. Due to the water solubility, hPG-b-mPEG can be easily removed out of the xerogel network by water extraction and be further used for Pd NP stabilization. The obtained silica xerogel supported Pd catalyst shows comparable activity as the aqueous Pd solution in the hydrogenation of COD. During the recycling investigation, a constant COD conversion is achieved for 10 runs and no activation is

observed, which indicated that Pd NPs are stabilized firmly onto silica xerogel by this one-pot approach.

Chapter 5.2 presents a one-pot synthesis of Pt NPs supported on SBA-15 for catalytic applications. A preformed Pt sol stabilized by PVA is used to avoid particle agglomeration during the sol-gel process. Besides of being a stabilizer, PVA has an additional function of a template. It is observed that the addition of PVA creates the connection between the larger mesopores created by the other template P123. Therefore, after loading a certain amount of Pt NPs, the surface area of SBA-15 shows only a negligible loss. Besides, no changes are observed on the pore size and porous structure of SBA-15. The obtained SBA-15 supported Pt catalyst shows a high activity in both liquid phase hydrogenation reaction and gas phase oxidation reaction. During the recycling application, no catalytic deactivation or metal leaching is observed, confirming that Pt NPs are effectively immobilized onto the support SBA-15.

In conclusion, the one-pot approach is a highly practical method to synthesize industrial catalysts. By adjusting the preparation conditions, MONPs and NMNPs can be highly dispersed on mesoporous silica materials. Due to the high accessibility of the mesoporous silica supports, the high dispersion and strong stabilization of nanoparticles, the catalysts showed impressive performance in some specific reactions. The easy procedure, up scalability and tunableness of the one-pot approach make it interesting for synthesizing industrial catalysts.

7. Outlook

Considering the simple synthesis, low cost of raw materials and impressive catalytic performance especially the capability of inhibiting carbon deposition, the $\text{Ni}_x\text{Mn}_{1-x}\text{O}$ catalyst has significant potential for industrial applications. However, there are still some interesting questions or aspects requiring a clear answer and further investigation.

1. Silica supported $\text{Ni}_x\text{Mn}_{1-x}\text{O}$ catalyst is a promising candidate catalyst for the DRM reaction in the combined process of the OCM and DRM reactions. However, in a single process, the DRM reaction is more practical to perform at 650-700 °C in order to obtain the balance between energy saving and reaction efficiency. Concerning the phase transition problem occurring above 600 °C from the support silica, it will be interesting to use another more thermal stable support, such as alumina. However, the influence on the formation of a solid solution $\text{Ni}_x\text{Mn}_{1-x}\text{O}$ should be considered.

2. The role of Mn in the DRM reaction is still unclear. It will be very interesting to investigate how Mn participates the DRM reaction through in-situ measurements, such as, in-situ IR. The influence of the oxidation state of Mn on the catalytic properties of the $\text{Ni}_x\text{Mn}_{1-x}\text{O}$ catalyst will be also interesting to study.

Using a water soluble stabilizer to immobilize NMNPs onto porous supports is highly desirable in industrial applications, due to the easy removal of the stabilizer by water extraction and the avoidance of thermal treatment. In this method, the interaction between the stabilizer polymer and NMNPs is an important factor to decide the dispersion of the supported NMNPs. A too strong interaction, e.g. covalent bonding, causes difficult removal of the stabilizer, and even the deactivation of the NMNPs. A weak interaction, e.g. electrostatic interaction, results in an inefficient stabilization especially in case of high NM loading, and particle sintering could occur. In our method, the stabilizer hPG-mPEG has relative weak interaction with Pd NPs. Therefore, optimizing the stabilizer or switch to another one to obtain a stronger interaction with NMNPs will be highly desirable for efficient stabilization of NMNPs.

Appendix A. Additional information

Amorphous silica supported NiMnO catalyst for the DRM reaction

In the DRM project, the bulk catalyst and supported catalyst are characterized before the reduction. The detailed results are presented in Figure I-IV. Figure I shows the nitrogen adsorption isotherms of both bulk catalyst $\text{Ni}_{0.2}\text{Mg}_{0.8}\text{O}_{\text{cp}}$ and $\text{Ni}_{0.2}\text{Mn}_{0.8}\text{O}_{\text{cp}}$. From the isotherms, both catalysts exhibit relative high surface area of $\sim 200 \text{ m}^2/\text{g}$ with meso size porosity.

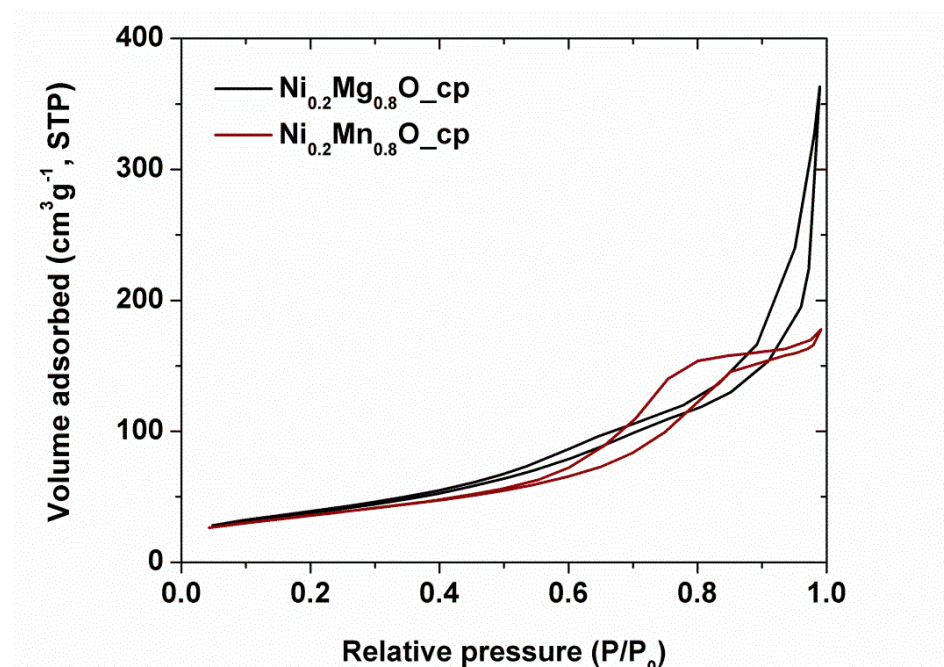


Figure I Nitrogen adsorption isotherms of $\text{Ni}_{0.2}\text{Mg}_{0.8}\text{O}_{\text{cp}}$ and $\text{Ni}_{0.2}\text{Mn}_{0.8}\text{O}_{\text{cp}}$ before reduction.

Figure II and III show the TEM images of $\text{Ni}_{0.2}\text{Mn}_{0.8}\text{O}_{\text{cp}}$ and $\text{Ni}_{0.2}\text{Mn}_{0.8}\text{O}_{\text{cp}}\text{-SiO}_2$ before reduction individually. In Figure II, Large spheres in the range of $0.5\text{-}2 \mu\text{m}$ are observed, which are composed of small crystallites with a size of approx. $5\text{-}7 \text{ nm}$. Compare to $\text{Ni}_{0.2}\text{Mn}_{0.8}\text{O}_{\text{cp}}$, $\text{Ni}_{0.2}\text{Mn}_{0.8}\text{O}_{\text{cp}}\text{-SiO}_2$ shows smaller spheres in Figure III, with porous silica surrounding the spheres, and the nanocrystallites are better dispersed and more spherical.

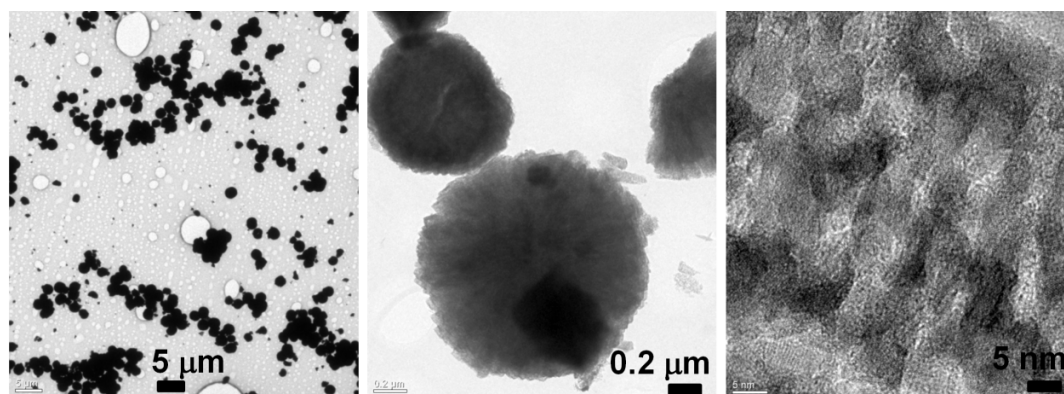


Figure II TEM images of $\text{Ni}_{0.2}\text{Mn}_{0.8}\text{O}_{\text{cp}}$ before reduction.

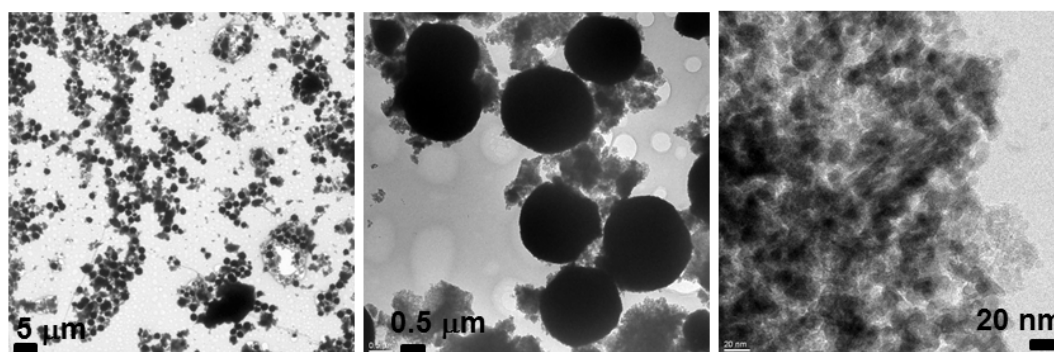


Figure III TEM images of $\text{Ni}_{0.2}\text{Mn}_{0.8}\text{O}_{\text{cp-SiO}_2}$ before reduction.

XRD patterns of $\text{Ni}_{0.2}\text{Mn}_{0.8}\text{O}_{\text{cp}}$ and $\text{Ni}_{0.2}\text{Mn}_{0.8}\text{O}_{\text{cp-SiO}_2}$ before reduction are presented in Figure IV. Both samples are composed of mixed phases of MnO_2 and NiMnO_3 . It confirms the assumption from the TPR experiments that the two dominant peaks are attributed to the reduction from MnO_2 to Mn_2O_3 and from Mn_2O_3 to MnO separately.

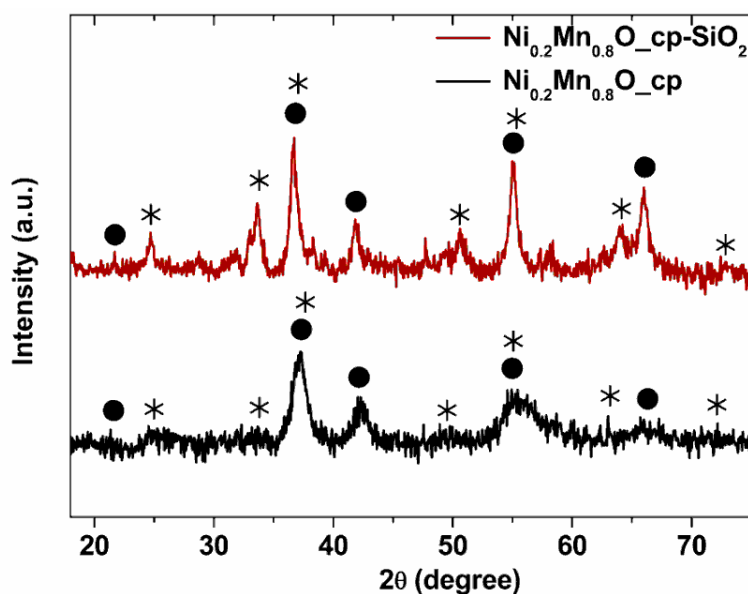


Figure IV XRD of $\text{Ni}_{0.2}\text{Mn}_{0.8}\text{O}_{\text{cp}}$ and $\text{Ni}_{0.2}\text{Mn}_{0.8}\text{O}_{\text{cp-SiO}_2}$ before reduction. Symbols denoted diffraction peaks of (●) – MnO_2 ¹⁸⁶ and (*) – NiMnO_3 ¹⁸⁷ ilmenite phase from database.

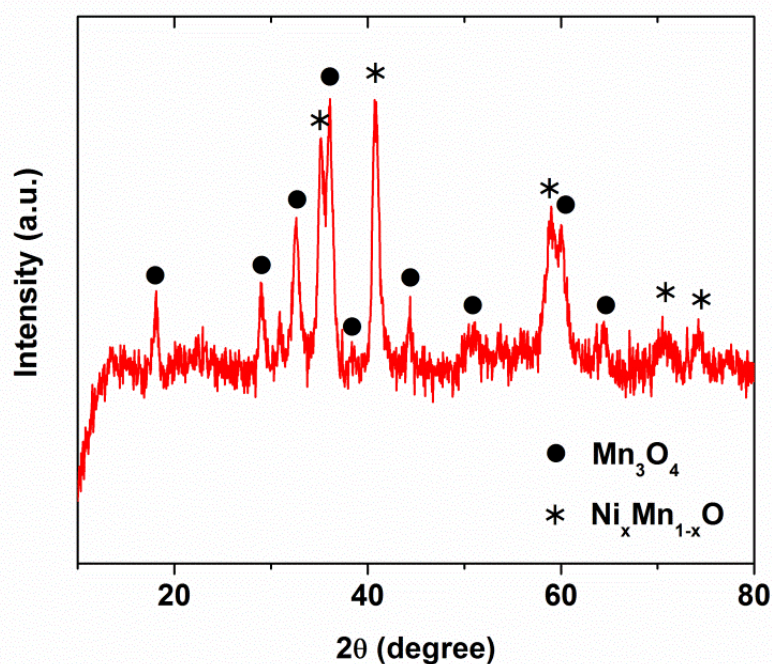


Figure V XRD patterns of $\text{Ni}_{0.2}\text{Mn}_{0.8}\text{O}_{\text{cp-SiO}_2}$ after 4 h reduction at 500 °C. Symbols denoted diffraction peaks of (●) – Mn_3O_4 and (*) – $\text{Ni}_x\text{Mn}_{1-x}\text{O}$ phase.

Figure V shows the XRD patterns of $\text{Ni}_{0.2}\text{Mn}_{0.8}\text{O}_{\text{cp-SiO}_2}$ 750 after 4 h reduction at 500 °C. The sample is composed of a mixed phases of $\text{Ni}_x\text{Mn}_{1-x}\text{O}$ ($x < 2$) and Mn_3O_4 , which means that this sample is not completely reduced yet. However, under the same reduction conditions, all catalysts calcined at 500 °C are reduced completely and formed a sole phase of $\text{Ni}_x\text{Mn}_{1-x}\text{O}$. This indicates that the catalyst calcined at higher temperature is more difficult to be reduced. This phenomenon is also observed in case of the solid solution catalyst $\text{Ni}_{0.03}\text{Mg}_{0.97}\text{O}$.⁷⁵ The calcination of this catalyst proceeded at 850 °C and the following reduction process requires the same high temperature.

Ultra high surface area SBA-15 supported Pt NPs for hydrogenation reactions

Figure VI shows the XRD patterns of SBA-15 samples aged at different temperatures. The sample aged at 100 °C showed highest 2 θ value, which indicates

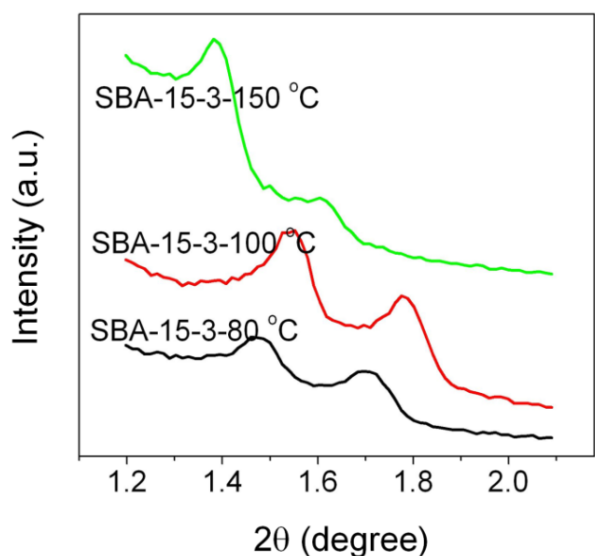


Figure VI XRD diffraction pattern of SBA-15-3 aged at different temperatures.

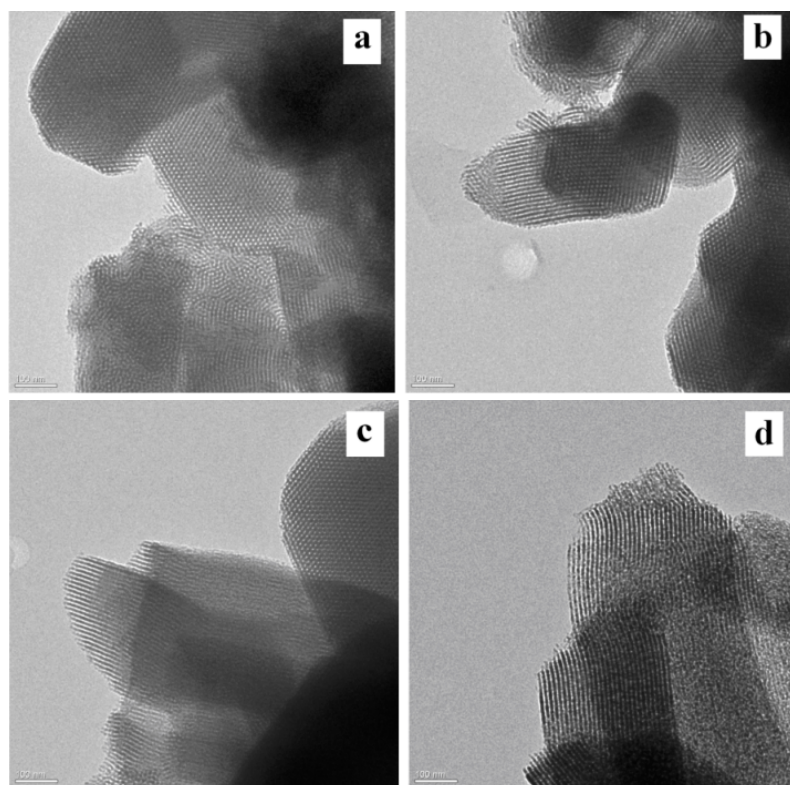


Figure VII TEM images of the samples (a) SBA-15-0.75; (b) SBA-15-5; (c) SBA-15-3-80; (d) SBA-15-3-150. The scale bar is 100 nm for all the images.

The TEM images of the SBA-15 samples synthesized with different molar ratio of PVA/TEOS are shown in Figure VII a-c. All TEM images exhibit similar well-ordered hexagonal arrays of mesopores. This means that the addition of PVA does not influence the order of the pluronic-silica composite. The pore size of the mesopores generated from the block-co-polymer is almost unchanged based on the BJH method on the adsorption branch (Figure VIII). Further increase of the PVA content does not yield further significant enhancement of the surface area or the pore volume.

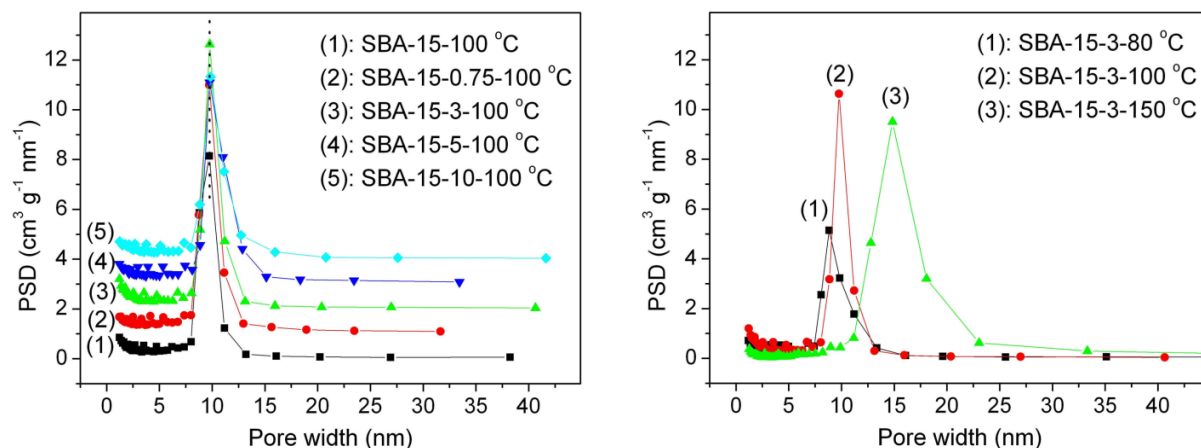


Figure VIII BJH pore size distribution plots of SBA-15 (calculated from the adsorption branch) synthesized under different conditions.

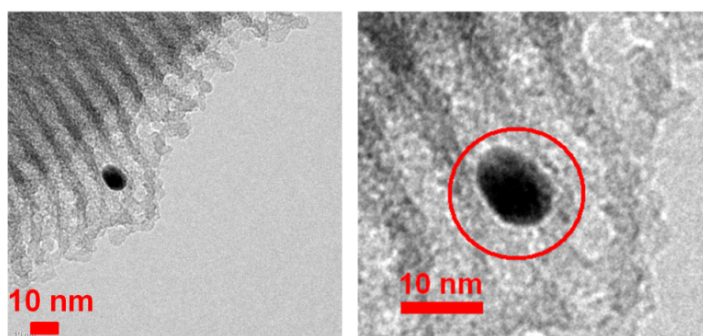


Figure IX Low and high magnification TEM image of a Pt NP within the pore channel of Pt-SBA-15-3.

High magnification TEM images of Pt-SBA-15-3 in Figure IX show that the Pt nanoparticles are located within the mesopores of SBA-15.

Appendix B. References

1. G. Q. Lu and X. S. Zhao, in *Nanoporous Materials: Science And Engineering*, 2004, pp. 1–12.
2. M. E. Davis, *Nature*, 2002, **417**, 813–821.
3. A. K. Cheetham, G. Ferey, and T. Loiseau, *Angew. Chem. Int. Ed*, 1999, **38**, 3268–3292.
4. D. Kaucký, A. Vondrová, J. Dědeček, and B. Wichterlová, *J. Catal.*, 2000, **194**, 318–329.
5. R. F. Lobo, *Nature*, 2006, **443**, 757–758.
6. J. Dwyer, *Chem. Ind.*, 1984, **7**, 258–269.
7. A. Corma, *Chem. Rev.*, 1997, **97**, 2373–2419.
8. R. M. Barrer and P. Denney, *J. Chem. Soc.*, 1961, 971–1000.
9. K. Byrappa and Y. M., *Handbook of hydrothermal technology*, 2001.
10. M. Jaroniec, and F. Schüth, *Chem. Mater.*, 2008, **20**, 599–600.
11. H. Li, M. Eddaoudi, M. O’Keeffe, and O. M. Yaghi, *Nature*, 1999, **402**, 276–279.
12. K. Seki, *Chem. Commun.*, 2001, 1496–1497.
13. A. C. Pierre and G. M. Pajonk, *Chem. Rev.*, 2002, **102**, 4243–4266.
14. M. Prassas and L. L. Hench, *Ultrastructure Processing of Ceramics, Glasses, and Composites*, New York. John Wiley & Sons, 1984.
15. L. H. Sommer, C. L. Frye, M. C. Musolf, G. A. Parker, P. G. Rodewald, K. W. Michael, Y. Okaya, and R. Pepinsky, *J. Am. Chem. Soc.*, 1961, **83**, 2210–2212.
16. L. H. Sommer and C. L. Frye, *J. Am. Chem. Soc.*, 1960, **82**, 3796.
17. L. H. Sommer, G. A. Parker, N. C. Lloyd, C. L. Frye, and K. W. Michael, *J. Am. Chem. Soc.*, 1967, **89**, 857–861.
18. N. Hüsing and U. Schubert, *Angew. Chem. Int. Ed*, 1998, **37**, 22–45.
19. E. R. Pohl and F. D. Osterholtz, *Molecular Characterization of Composite Interfaces*, Plenum, New York, 1985.

References

20. C. Chiang, C. M. Ma, D. Wu, and H. Kuan, *J. Poly. Sci.; Part A; Poly. Chem.*, 2003, **41**, 905–913.
21. C. J. Brinker and G. W. Scherer, *Sol-Gel Science: the Physics and Chemistry of Sol-Gel Processing*, San Diego, Academic Press Inc., 1990.
22. J. Estella, J. C. Echeverría, M. Laguna, and J. J. Garrido, *Microporous Mesoporous Mater.*, 2007, **102**, 274–282.
23. B. Topuz and M. Çiftçioğlu, *J. Memb. Sci.*, 2010, **350**, 42–52.
24. H. K. Schmidt, E. Geiter, M. Mennig, H. Krug, C. Becker, and R.-P. Winkler, *J. Sol-Gel Sci. Technol.*, 1998, **13**, 397–404.
25. C. Marzolin, S. P. Smith, M. Prentiss, and G. M. Whitesides, *Adv. Mater.*, 1998, **10**, 571–574.
26. Z. W. He, C. M. Zhen, X. Q. Liu, W. Lan, D. Y. Xu, and Y. Y. Wang, *Thin Solid Films*, 2004, **462-463**, 168–171.
27. G. C. Esther, J. A. Menéndez, and A. Arenillas, in *Nanotechnology and Nanomaterials*, 2011, p. 196.
28. A. C. Pierre, *Introduction to Sol-Gel Processing*, Kluwer Academic Publishers, 1998.
29. R. J. White, R. Luque, V. L. Budarin, J. H. Clark, and D. J. Macquarrie, *Chem. Soc. Rev.*, 2009, **38**, 481–94.
30. H. Choi, S. R. Al-Abed, S. Agarwal, and D. D. Dionysiou, *Chem. Mater.*, 2008, **20**, 3649–3655.
31. M. Kulawik, N. Nilius, and H.-J. Freund, *Phys. Rev. Lett.*, 2006, **96**, 036103–1–4.
32. J.-L. Lu, H.-J. Gao, S. Shaikhutdinov, and H.-J. Freund, *Catal. Lett.*, 2007, **114**, 8–16.
33. Z. H. Qin, M. Lewandowski, Y. N. Sun, S. Shaikhutdinov, and H. J. Freund, *J. Phys. Chem. C*, 2008, **112**, 10209–10213.
34. D. E. Starr, S. K. Shaikhutdinov, and H.-J. Freund, *Top. Catal.*, 2005, **36**, 33–41.
35. R. Y. Parapat, V. Parwoto, M. Schwarze, B. Zhang, D. S. Su, and R. Schomäcker, *J. Mater. Chem.*, 2012, **22**, 11605–11614.
36. R. Y. Parapat, M. Wijaya, M. Schwarze, S. Selve, M. Willinger, and R. Schomäcker, *Nanoscale*, 2013, **5**, 796–805.
37. A. Rodriguez, S. Chaturvedi, M. Kuhn, and J. Hrbek, *J. Phys. Chem. B*, 1998, 5511–5519.

References

38. M. Fernandez-Garcia, J. C. Conesa, and F. Illas, *Surf. Sci.*, 1996, **349**, 207–215.
39. R. Hoffmann, *Solids and Surfaces: a chemist's view of bonding in extended structures*, 1988.
40. J. L. Anchell and A. C. Hess, *J. Phys. Chem.*, 1996, **100**, 18317–18321.
41. A. M. Ferrari and G. Pacchioni, *J. Phys. Chem.*, 1995, **99**, 17010–17018.
42. J. A. Rodriguez, J. Hrbek, J. Dvorak, T. Jirsak, and A. Maiti, *Chem. Phys. Lett.*, 2001, **336**, 377–384.
43. R. Richards, W. Li, S. Decker, C. Davidson, O. Koper, V. Zaikovski, A. Volodin, T. Rieker, and K. J. Klabunde, *J. Am. Chem. Soc.*, 2000, **122**, 4921–4925.
44. J. a. Rodriguez, X. Wang, G. Liu, J. C. Hanson, J. Hrbek, C. H. F. Peden, A. Iglesias-Juez, and M. Fernández-García, *J. Mol. Catal. A Chem.*, 2005, **228**, 11–19.
45. A. M. Maitra, *Appl. Catal. A Gen.*, 1993, **104**, 11–59.
46. A. Z. Khan and E. Ruckenstein, *J. Catal.*, 1992, **138**, 322–342.
47. J. H. Lunsford, *Angew. Chem. Int. Ed. Engl.*, 1995, **34**, 970–980.
48. G. J. Hutchings, M. S. Scurrrell, and J. R. Woodhouse, *Chem. Soc. Rev.*, 1989, **18**, 251–283.
49. G. A. Olah, *Acc. Chem. Res.*, 1987, **20**, 422–428.
50. A. Granada, S. B. Karra, and S. M. Senkan, *Ind. Eng. Chem. Res.*, 1987, **26**, 1901–1905.
51. H. D. Gesser, N. R. Hunter, and C. B. Prakash, *Chem. Rev.*, 1985, **85**, 235–244.
52. R. A. Periana, D. J. Taube, E. R. Evitt, D. G. Löffler, P. R. Wentreck, G. Voss, and T. Masuda, *Science (80-.)*, 1993, **259**, 340–343.
53. M. J. Brown and N. D. Parkyns, *Catal. Today*, 1991, **8**, 305–335.
54. A. P. E. York, T. Xiao, M. L. H. Green, and J. B. Claridge, *Catal. Rev. -Sci. Eng.*, 2007, **49**, 511–560.
55. V. Havran, M. P. Dudukovi, and C. S. Lo, *Ind. Eng. Chem. Res.*, 2011, **50**, 7089–7100.
56. M. C. J. Bradford and M. a. Vannice, *Catal. Rev. -Sci. Eng.*, 1999, **41**, 1–42.
57. M. A. Vannice, *catal. Rev.-sci. eng.*, 1975, **14**, 153.
58. N. M. Bodrov, L. O. Apelbaum, and M. I. Temkin, *Kinet. Catal.*, 1964, **5**, 614.

References

59. N. M. Bodrov, L. O. Apel'baum, and M. I. Temkin, *Kinet. Catal.*, 1967, **8**, 326.
60. Z. L. Zhang and X. E. Verykios, *Catal. Today*, 1994, **21**, 589–595.
61. M. C. J. Bradford and M. A. Vannice, *Appl. Catal. A Gen.*, 1996, **142**, 73–96.
62. M. C. J. Bradford and M. A. Vannice, *J. Catal.*, 1998, **173**, 157–171.
63. M. M. Barroso-Quiroga and A. E. Castro-Luna, *Ind. Eng. Chem. Res.*, 2007, **46**, 5265–5270.
64. J. R. Rostrup-Nielsen and J.-H. Bak Hansen, *J. Catal.*, 1993, **144**, 38–49.
65. J. T. Richardson and S. a. Paripatyadar, *Appl. Catal.*, 1990, **61**, 293–309.
66. M. C. J. Bradford, *Catal. Lett.*, 2000, **66**, 113–120.
67. M. C. J. Bradford and M. A. Vannice, *Catal. Today*, 1999, **50**, 87–96.
68. X. Lv, J.-F. Chen, Y. Tan, and Y. Zhang, *Catal. Commun.*, 2012, **20**, 6–11.
69. S. Zhang, J. Wang, H. Liu, and X. Wang, *Catal. Commun.*, 2008, **9**, 995–1000.
70. J. Zhang, X. Zhang, M. Tu, W. Liu, H. Liu, J. Qiu, L. Zhou, Z. Shao, H. L. Ho, and K. L. Yeung, *J. Power Sources*, 2012, **198**, 14–22.
71. H. Koh, S. Lee, and J. Choi, *Bull. Korean Chem. Soc.*, 2004, **25**, 1253–1256.
72. N. Arena, F. Giordano, *J. Catal.*, 1991, **132**, 58–67.
73. Y. Chen, K. Tomishige, K. Yokoyama, and K. Fujimoto, *Appl. Catal. A Gen.*, 1997, **165**, 335–347.
74. Y. H. Hu and E. Ruckenstein, *Catal. Rev. -Sci. Eng.*, 2002, **44**, 423–453.
75. K. F. K. Yamazaki O, Tomishige, *Catal Lett*, 1996, **39**, 91–95.
76. K. Tomishige, O. Yamazaki, Y. Chen, K. Yokoyama, X. Li, and K. Fujimoto, *Catal. Today*, 1998, **45**, 35–39.
77. J. Alvarez, G. Valderrama, E. Pietri, M. J. Pérez-Zurita, C. U. Navarro, E. F. Sousa-Aguiar, and M. R. Goldwasser, *Top. Catal.*, 2011, **54**, 170–178.
78. G. C. De Araujo, S. M. De Lima, J. M. Assaf, M. A. Peña, J. L. G. Fierro, and M. do Carmo Rangel, *Catal. Today*, 2008, **133-135**, 129–135.
79. A. Khalesi, H. R. Arandiyani, and M. Parvari, *Ind. Eng. Chem. Res.*, 2008, **47**, 5892–5898.

References

80. S. Pavlova, L. Kapokova, R. Bunina, G. Alikina, N. Sazonova, T. Krieger, A. Ishchenko, V. Rogov, R. Gulyaev, V. Sadykov, and C. Mirodatos, *Catal. Sci. Technol.*, 2012.
81. S. Gallego, C. Batiot-dupeyrat, and F. Mondrago, *Ind. Eng. Chem. Res.*, 2008, **47**, 9272–9278.
82. I. Rivas, J. Alvarez, E. Pietri, M. J. Pérez-Zurita, and M. R. Goldwasser, *Catal. Today*, 2010, **149**, 388–393.
83. G. Valderrama, M. R. Goldwasser, C. U. De Navarro, J. M. Tatibouët, J. Barrault, C. Batiot-Dupeyrat, and F. Martínez, *Catal. Today*, 2005, **107-108**, 785–791.
84. Z. Zhang and X. E. Verykios, *Catal. Letters*, 1996, **38**, 175–179.
85. X. E. Verykios, *Int. J. Hydrogen Energy*, 2003, **28**, 1045–1063.
86. N. Laosiripojana, W. Sutthisripok, and S. Assabumrungrat, *Chem. Eng. J.*, 2005, **112**, 13–22.
87. N. a. Pechimuthu, K. K. Pant, S. C. Dhingra, and R. Bhalla, *Ind. Eng. Chem. Res.*, 2006, **45**, 7435–7443.
88. V. Sadykov, V. Muzykantov, A. Bobin, N. Mezentseva, G. Alikina, N. Sazonova, E. Sadovskaya, L. Gubanova, A. Lukashevich, and C. Mirodatos, *Catal. Today*, 2010, **157**, 55–60.
89. V. M. Gonzalez-delacruz, R. Pereniguez, F. Ternero, J. P. Holgado, and A. Caballero, *ACS Catal.*, 2011, **1**, 82–88.
90. S. Sokolov, E. V. Kondratenko, M.-M. Pohl, A. Barkschat, and U. Rodemerck, *Appl. Catal. B Environ.*, 2012, **113-114**, 19–30.
91. D. Liu, W. N. E. Cheo, Y. W. Y. Lim, A. Borgna, R. Lau, and Y. Yang, *Catal. Today*, 2010, **154**, 229–236.
92. P. Frontera, a. Macario, a. Aloise, F. Crea, P. L. Antonucci, J. B. Nagy, F. Frusteri, and G. Giordano, *Catal. Today*, 2012, **179**, 52–60.
93. J. Matos, M. Rosales, G. González, and C. U. De Navarro, *Open Mater. Sci. J.*, 2010, **4**, 125–132.
94. a Nandini, K. Pant, and S. Dhingra, *Appl. Catal. A Gen.*, 2005, **290**, 166–174.
95. F. Frusteri, F. Arena, G. Calogero, T. Torre, and a. Parmaliana, *Catal. Commun.*, 2001, **2**, 49–56.
96. J. Wei, *J. Catal.*, 2004, **225**, 116–127.

References

97. H. Y. Wang and C. T. Au, *Appl. Catal. A Gen.*, 1997, **155**, 239–252.
98. J. H. Bitter, K. Seshan, and J. A. Lercher, *J. Catal.*, 1998, **176**, 93–101.
99. Ş. Özkara-Aydinoğlu and a. E. Aksoylu, *Int. J. Hydrogen Energy*, 2011, **36**, 2950–2959.
100. G. K. Reddy, S. Lorient, A. Takahashi, P. Delichère, and B. M. Reddy, *Appl. Catal. A Gen.*, 2010, **389**, 92–100.
101. S. J. Tauster, *Facts and Uncertainties*, 1986, **298**, 1–9.
102. S. J. Tauster, *Acc. Chem. Res.*, 1987, **20**, 389–394.
103. O. Takayasu, N. Hongo, and I. Matsuura, *Stud. Surf. Sci. Catal.*, 1993, **77**, 305–308.
104. E. Ruckenstein and Y. H. Hu, *Appl. Catal. A Gen.*, 1995, **133**, 149–161.
105. Y. H. Hu and E. Ruckenstein, *Catal. Letters*, 1997, **43**, 71–77.
106. E. Ruckenstein and Y. H. Hu, *Appl. Catal. A Gen.*, 1997, **154**, 185–205.
107. M. Rigaud, G. Giovannetti, and M. Hone, *J. Chem. Thermodyn.*, 1974, **6**, 993–998.
108. S. L. Blank and J. A. Pask, *J. Am. Ceram. Soc.*, 1969, **52**, 669–675.
109. Y. F. Chang and H. Heinemann, *Catal. Lett.*, 1993, **21**, 215–224.
110. D. Dissanayake, M. P. Rosynek, and J. H. Lunsford, *J. Phys. Chem.*, 1993, **97**, 3644–3646.
111. E. Ruckenstein and H. Y. Wang, *Catal. Lett.*, 2001, **73**, 99–105.
112. M. A. Peña and J. L. G. Fierro, *Chem. Rev.*, 2001, **101**, 1981–2017.
113. N. K. Labhsetwar, A. Watanabe, and T. Mitsuhashi, *Appl. Catal. B Environ.*, 2003, **40**, 21–30.
114. C. Liu, J. Ye, J. Jiang, and Y. Pan, *ChemCatChem*, 2011, **3**, 529–541.
115. M. . Goldwasser, M. . Rivas, E. Pietri, M. . Pérez-Zurita, M. . Cubeiro, L. Gingembre, L. Leclercq, and G. Leclercq, *Appl. Catal. A Gen.*, 2003, **255**, 45–57.
116. M. R. Goldwasser, M. E. Rivas, E. Pietri, M. J. Pérez-Zurita, M. L. Cubeiro, A. Grivobal-Constant, and G. Leclercq, *J. Mol. Catal. A Chem.*, 2005, **228**, 325–331.
117. G. Valderrama, A. Kiennemann, and M. R. Goldwasser, *Catal. Today*, 2008, **133-135**, 142–148.

References

118. N. M. Rodriguez, *J. Mater. Res.*, 1993, **8**, 3233–3250.
119. A. T. Ashcroft, A. K. Cheetham, M. L. H. Green, and P. D. F. Vernon, *Nature*, 1991, **352**, 225–226.
120. O. Yamazaki, T. Nozaki, K. Omata, and K. Fujimoto, *Chem. Lett.*, 1992, 1953–1954.
121. F. Meshkani and M. Rezaei, *Int. J. Hydrogen Energy*, 2010, **35**, 10295–10301.
122. Tulsa, *Oil and Gas Journal Data Book*, Penn well, 1994.
123. Y. Mei, G. Sharma, Y. Lu, M. Ballauff, M. Drechsler, T. Irrgang, and R. Kempe, *Langmuir*, 2005, **21**, 12229–12234.
124. M. Schrunner, M. Ballauff, Y. Talmon, Y. Kauffmann, J. Thun, M. Möller, and J. Breu, *Science (80-.)*, 2009, **323**, 617–620.
125. H. Hata, Y. Kobayashi, V. Bojan, W. J. Youngblood, and T. E. Mallouk, *Nano Lett.*, 2008, **8**, 794–799.
126. Y. H. Ng, S. Ikeda, T. Harada, Y. Morita, and M. Matsumura, *Chem. Commun.*, 2008, 3181–3183.
127. G. Rupprechter, K. Hayek, and H. Hofmeister, *J. Catal.*, 1998, **173**, 409–422.
128. R. Narayanan and M. A. El-Sayed, *Nano Lett.*, 2004, **4**, 1343–1348.
129. C. Galeano, R. Güttel, M. Paul, P. Arnal, A. Lu, and F. Schüth, *Chem. - A Eur. J.*, 2011, **17**, 8434–8439.
130. F. Schwyer, P. Braunstein, J. Rosé, C. Estournès, J. Guille, H. Kessler, and J.-L. Paillaud, *Chem. Commun.*, 2000, 1271–1272.
131. J. L. Figueiredo, M. F. R. Pereira, P. Serp, P. Kalck, P. V. Samant, and J. B. Fernandes, *Carbon N. Y.*, 2006, **44**, 2516–2522.
132. H. Xie, J. Y. Howe, V. Schwartz, J. Monnier, C. T. Williams, and H. J. Ploehn, *J. Catal.*, 2008, **259**, 111–122.
133. C. Alié, F. Ferauche, A. Léonard, S. Lambert, N. Tcherkassova, B. Heinrichs, M. Crine, P. Marchot, E. Loukine, and J. P. Pirard, *Chem. Eng. J.*, 2006, **117**, 13–22.
134. J. Raula, J. Shan, M. Nuopponen, A. Niskanen, H. Jiang, E. I. Kauppinen, and H. Tenhu, *Langmuir*, 2003, **19**, 3499–3504.
135. C. A. Kawaguti, S. H. Pulcinelli, C. V. Santilli, and A. F. Craievich, *J. Sol-Gel Sci. Technol.*, 2006, **37**, 213–217.

References

136. F. Schweyer-Tihay, P. Braunstein, C. Estourne, J. L. Guille, B. Lebeau, J.-L. Paillaud, M. Richard-Plouet, and J. Rose, *Chem. Mater.*, 2003, **15**, 57–62.
137. H. Li, J. Lü, Z. Zheng, and R. Cao, *J. Coll. Int. Sci.*, 2011, **353**, 149–155.
138. Z. Zheng, H. Li, T. Liu, and R. Cao, *J. Catal.*, 2010, **270**, 268–274.
139. W. Huang, J. N. Kuhn, C.-K. Tsung, Y. Zhang, S. E. Habas, P. Yang, and G. A. Somorjai, *Nano Lett.*, 2008, **8**, 2027–2034.
140. R. M. Crooks, M. Zhao, L. Sun, V. Chechik, and L. K. Yeung, *Acc. Chem. Res.*, 2001, **34**, 181–190.
141. Y. Guari, C. Thieuleux, A. Mehdi, C. Reyé, R. J. P. Corriu, S. Gomez-Gallardo, K. Philippot, B. Chaudret, and R. Dutartre, *Chem. Commun.*, 2001, 1374–1375.
142. Y. Guari, C. Thieuleux, A. Mehdi, C. Reye, R. J. P. Corriu, S. Gomez-gallardo, K. Philippot, and B. Chaudret, *Chem. Mater.*, 2003, **15**, 2017–2024.
143. Y. Guari, K. Soulantica, K. Philippot, C. Thieuleux, A. Mehdi, C. Reye, B. Chaudret, and R. J. P. Corriu, *New J. Chem.*, 2003, **27**, 1029–1031.
144. V. Hulea, D. Brunel, A. Galarneau, K. Philippot, B. Chaudret, P. J. Kooyman, and F. Fajula, *Micro. Meso. Mater.*, 2005, **79**, 185–194.
145. N. Job, S. Lambert, M. Chatenet, C. J. Gommès, F. Maillard, S. Berthon-Fabry, J. R. Regalbuto, and J.-P. Pirard, *Catal. Today*, 2010, **150**, 119–127.
146. L. Courthéoux, F. Popa, E. Gautron, S. Rossignol, and C. Kappenstein, *J. Non-Crystal. Solids*, 2004, **350**, 113–119.
147. A. Kaiser, C. Görsmann, and U. Schubert, *J. Sol-Gel Sci. Technol.*, 1997, **8**, 795–799.
148. C. Aprile, A. Abad, H. García, and A. Corma, *J. Mater. Chem.*, 2005, **15**, 4408–4413.
149. H. Song, R. M. Rioux, J. D. Hoefelmeyer, R. Komor, K. Niesz, M. Grass, P. Yang, and G. A. Somorjai, *J. Am. Chem. Soc.*, 2006, **128**, 3027–3037.
150. M. Boualleg, J. Basset, J. Candy, P. Delichere, K. Pelzer, L. Veyre, and C. Thieuleux, *Chem. Mater.*, 2009, **21**, 775–777.
151. S. J. Tauster, S. C. Fung, R. T. Baker, and J. a Horsley, *Science (80-.)*, 1981, **211**, 1121–5.
152. S. Takatani and Y.-W. Chung, *J. Catal.*, 1984, **90**, 75–83.
153. Y.-W. Chung and Y. B. Zhao, *ACS Symp. Ser.*, 1986, **298**, 54–59.

References

154. S. H. Choi, S. H. Seok, and J. S. Lee, *J. Synchrotron Radiat.*, 2001, **8**, 596–598.
155. S.-H. Seok, S. H. Choi, E. D. Park, S. H. Han, and J. S. Lee, *J. Catal.*, 2002, **209**, 6–15.
156. S.-H. Seok, Han, Sung Hwan, and J. S. Lee, *Appl. Catal. A Gen.*, 2001, **215**, 31–38.
157. L. Christel, A. Pierre, and D. A.-M. R. Abel, *Thermochim. Acta*, 1997, **306**, 51–59.
158. Y. H. Hu and E. Ruckenstein, *Catal. Letters*, 1996, **36**, 145–149.
159. P. J. Linstrom and W. G. Mallard, *NIST Chem. WebBook*, *NIST Chem. WebBook*, *NIST Stand. Ref. Database Number 69*, Natl. Inst. Stand. Technol. Gaithersbg. MD, 20899, 2012, 6.
160. S. Nowag, X. S. Wang, J. Keilitz, A. Thomas, and R. Haag, *ChemCatChem*, 2010, **2**, 807–811.
161. B. Heinrichs, F. Noville, and J.-P. Pirard, *J. Catal.*, 1997, **170**, 366–376.
162. J. Zhu, X. Xie, S. a. C. Carabineiro, P. B. Tavares, J. L. Figueiredo, R. Schomäcker, and A. Thomas, *Energy Environ. Sci.*, 2011, **4**.
163. D. Steinhilber, *Master Thesis*, 2008, P36.
164. F.-S. Lin, C.-T. Chien, W.-C. Chiu, S.-Y. Lin, F.-G. Tseng, Y. Hwu, and C.-S. Yang, *RSC Adv.*, 2012, **2**, 7174–7179.
165. B. Lee, Z. Ma, Z. Zhang, C. Park, and S. Dai, *Micro. Meso. Mater.*, 2009, **122**, 160–167.
166. X. Liu, A. Wang, X. Wang, C.-Y. Mou, and T. Zhang, *Chem. Commun.*, 2008, 3187–3189.
167. M. N. Timofeeva, S. H. Jhung, Y. K. Hwang, D. K. Kim, V. N. Panchenko, M. S. Melgunov, Y. A. Chesalov, and J.-S. Chang, *Appl. Catal. A Gen.*, 2007, **317**, 1–10.
168. C.-P. Huang and Y.-H. Huang, *Appl. Catal. A Gen.*, 2008, **346**, 140–148.
169. M. N. Timofeeva, O. a. Kholdeeva, S. H. Jhung, and J.-S. Chang, *Appl. Catal. A Gen.*, 2008, **345**, 195–200.
170. P. Han, H. Zhang, X. Qiu, X. Ji, and L. Gao, *J. Mol. Catal. A Chem.*, 2008, **295**, 57–67.
171. J. Demel, J. Čejka, and P. Štěpnička, *J. Mol. Catal. A Chem.*, 2010, **329**, 13–20.
172. F. Su, L. Lv, F. Y. Lee, T. Liu, A. I. Cooper, and X. S. Zhao, *J. Am. Chem. Soc.*, 2007, **129**, 14213–14223.
173. D. P. Serrano, J. Aguado, and C. Vargas, *Appl. Catal. A Gen.*, 2008, **335**, 172–179.

References

174. J. Hu, L. Chen, K. Zhu, A. Suchopar, and R. Richards, *Catal. Today*, 2007, **122**, 277–283.
175. R. M. Rioux, R. Komor, H. Song, J. D. Hoefelmeyer, M. Grass, K. Niesz, P. Yang, and G. A. Somorjai, *J. Catal.*, 2008, **254**, 1–11.
176. C. Yang, P. Liu, Y. Ho, C. Chiu, and K. Chao, *Chem. Mater.*, 2003, **15**, 275–280.
177. J. Liu, Q. Yang, X. S. Zhao, and L. Zhang, *Micro. Meso. Mater.*, 2007, **106**, 62–67.
178. D. Zhao, J. Feng, Q. Huo, N. Melosh, G. H. Fredrickson, B. F. Chmelka, and G. D. Stucky, *Science (80-.)*, 1998, **279**, 548–552.
179. A. Galarneau, H. Cambon, F. Di Renzo, R. Ryoo, M. Choi, and F. Fajula, *New J. Chem.*, 2003, **27**, 73–79.
180. C. G. Göltner, B. Smarsly, B. Berton, and M. Antonietti, *Chem. Mater.*, 2001, **13**, 1617–1624.
181. R. Paladhi and R. P. Sinch, *J. Appl. Polym. Sci.*, 1994, **51**, 1559–1565.
182. S. G. Abd Alla, H. M. Said, and A. W. M. El-Naggar, *J. Appl. Polym. Sci.*, 2004, **94**, 167–176.
183. S. Chytil, W. R. Glomm, and E. A. Blekkan, *Catal. Today*, 2009, **147**, 217–223.
184. M. Santhosh Kumar, D. Chen, A. Holmen, and J. C. Walmsley, *Catal. Today*, 2009, **142**, 17–23.
185. L. Jiao and J. R. Regalbuto, *J. Catal.*, 2008, **260**, 342–350.
186. Soven, *Econ. Geol.*, 1960, **55**, 278.
187. W. H. Cloud, *Phys. Rev.*, 1958, **111**, 1046.

Appendix C. Characterization methods

X-ray diffraction (XRD)

X-rays primarily interact with electrons in atoms. When x-ray photons collide with electrons, some photons from the incident beam will be deflected away from the direction where they original travel. If the wavelength of these scattered x-rays did not change (meaning that x-ray photons did not lose any energy), the process is called elastic scattering (Thompson Scattering) in that only momentum has been transferred in the scattering process. These are the x-rays measured in diffraction experiments, as the scattered x-rays carry information about the electron distribution in materials. Diffracted waves from different atoms can interfere with each other and the resultant intensity distribution is strongly modulated by this interaction. If the atoms are arranged in a periodic fashion, as in crystals, the diffracted waves will consist of sharp interference maxima (peaks) with the same symmetry as in the distribution of atoms. Measuring the diffraction pattern therefore allows us to deduce the distribution of atoms in a material.

The peaks in an X-ray diffraction pattern are directly related to the atomic distances in the crystalline powder according to a mathematical relation called “Bragg’s Law”. Bragg reflection occurs only when the angle of incidence (here measured between the incident direction and the planes) is equal to a Bragg angle θ_B that satisfies Bragg’s law:

$$n\lambda = 2d \sin\theta$$

where **n** is an integer,

λ is the wavelength of the incident X-ray beam,

d is the distance between atomic layers in a crystal, generating the diffraction and

θ is the diffraction angle of incidence.

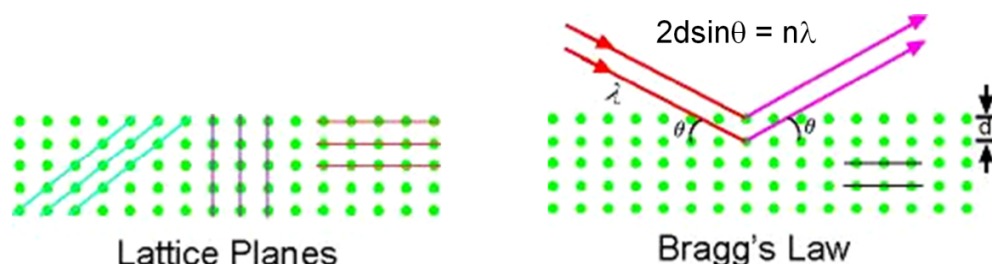


Figure i. Lattice planes in a crystalline and Bragg's Law reflection. The diffracted X-rays exhibit constructive interference when the distance between paths ($2d\sin\theta$) differs by an integer number of wavelengths (λ).

λ and d are measured in the same units, usually angstroms. For a powder specimen in a diffractometer having a statistically infinite amount of randomly oriented crystallites, diffraction maxima (or peaks) are measured along the 2θ diffractometer circle. The “angle” of the diffraction (recorded as 2θ by convention) is related to the interplanar spacing, d , by the Bragg law, and the intensity of the diffraction maximum is related to the strength of those diffractions in the specimen.

A coherent beam of monochromatic X-rays of known wavelength is required for XRD analysis. Striking a pure anode of a particular metal with high-energy electrons in a sealed vacuum tube generates X-rays that may be used for X-ray diffraction. By the right choice of metal anode and energy of accelerated electrons, a known wavelength (i.e., energy) or group of wavelengths will dominate the X-rays generated. Copper (Cu) X-ray tubes are most commonly used for X-ray diffraction of inorganic materials. The wavelength of the strongest Cu radiation ($K\alpha$) is approximately 1.54 angstroms (\AA). Other anodes commonly used in X-ray generating tubes include Cr ($K\alpha$ 2.29 \AA), Fe ($K\alpha$ 1.94 \AA), Co ($K\alpha$ 1.79 \AA), and Mo ($K\alpha$ 0.71 \AA).

Powder Diffraction

Powder XRD (X-ray Diffraction) is perhaps the most widely used x-ray diffraction technique for characterizing materials. As the name suggests, the sample is usually in a powdery form, consisting of fine grains of single crystalline material to be studied. The technique is used also

widely for studying particles in liquid suspensions or polycrystalline solids (bulk or thin film materials).

The real meaning of the term 'powder' is that the crystalline domains are randomly oriented in the sample. Therefore when the 2-D diffraction pattern is recorded, it shows concentric rings of scattering peaks corresponding to the various d spacings in the crystal lattice. The positions and the intensities of the peaks are used for identifying the underlying structure (or phase) of the material. For example, the diffraction lines of graphite would be different from diamond even though they both are made of carbon atoms. This phase identification is important because the material properties are highly dependent on structure.

Powder diffraction data can be collected using either transmission or reflection geometry, as shown in Figure ii. Because the particles in the powder sample are randomly oriented, these two methods will yield the same data. In the MRL x-ray facility, powder diffraction data are measured using the Philips XPERT MPD diffractometer, which measures data in reflection mode and is used mostly with solid samples, or the custom built 4-circle diffractometer, which operates in transmission mode and is more suitable for liquid phase samples.

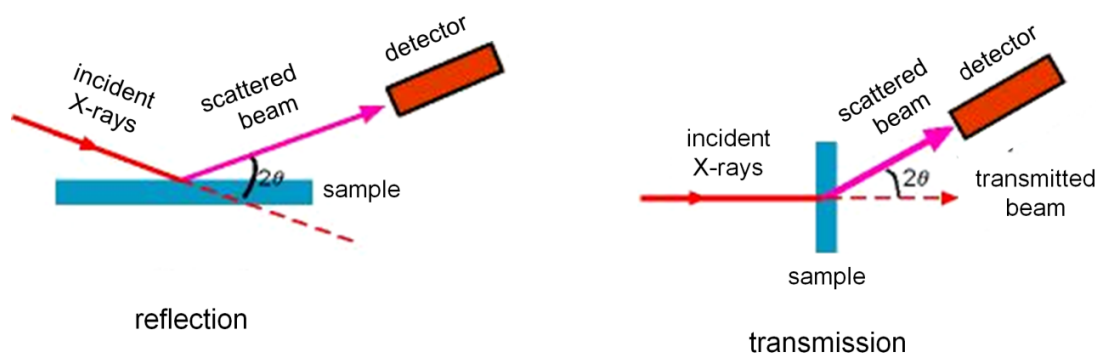


Figure ii. Geometry of XRD: (left) reflection mode; (right) transmission mode.

Transmission electron microscopy (TEM)

The TEM has been proved invaluable for examining the ultrastructure of metals. For example, crystalline defects known as dislocations were first predicted by theorists to account for the fact that metals deform under much lower forces than calculated for perfect crystalline array of atoms.

They were first seen directly in TEM images of aluminum. With a modern TEM (resolution ≈ 0.2 nm), it is even possible to image individual atomic planes or columns of atoms.

In a transmission electron microscope, electrons penetrate a thin specimen and are then imaged by appropriate lenses, in broad analogy with the biological light microscope. The focusing of electrons relies on the fact that, in addition to their wave like character, they behave as negatively charged particles and are therefore deflected by electric or magnetic fields.

Early in the 20th century, physicists discovered that material particles such as electrons possess a wavelike character. Inspired by Einstein's photon description of electromagnetic radiation, Louis de Broglie proposed that their wavelength is given by

$$\lambda = h / p = h / (mv)$$

where $h = 6.626 \cdot 10^{-34}$ Js is the Planck constant; p , m , and v represent the momentum, mass, and speed of the electron. For electrons emitted into vacuum from a heated filament and accelerated through a potential difference of 50 V, $v \approx 4.2 \cdot 10^6$ m/s and $\lambda \approx 0.17$ nm. Because this wavelength is comparable to atomic dimensions, such "slow" electrons are strongly diffracted from the regular array of atoms at the surface of a crystal, as first observed by Davisson and Germer.

Raising the accelerating potential to 50 kV, the wavelength shrinks to about 5 pm and such higher-energy electrons can penetrate distances of several microns into a solid. If the solid is crystalline, the electrons are diffracted by atomic planes inside the material, as in the case of X-rays.

There are four main components to a transmission electron microscope: an electron optical column, a vacuum system, the necessary electronics (lens supplies for focusing and deflecting the beam and the high voltage generator for the electron source), and control software.

The electron column includes elements analogous to those of a light microscope. The light source of the light microscope is replaced by an electron gun, which is built into the column. The glass lenses are replaced by electromagnetic lenses. Unlike glass lenses, the power (focal length) of magnetic lenses can be changed by changing the current through the lens coil. The eyepiece or ocular is replaced by a fluorescent screen and/or a digital camera.

The electron beam emerges from the electron gun (usually at the top of the column), and is condensed into a nearly parallel beam at the specimen by the condenser lenses. The specimen must be thin enough to transmit the electrons, typically 0.5 μm or less. Higher energy electrons can penetrate thicker samples. After passing through the specimen, transmitted electrons are collected and focused by the objective lens and a magnified real image of the specimen is projected by the projection lens onto the viewing device at the bottom of the column. The entire electron path from gun to camera must be under vacuum (otherwise the electrons would collide with air molecules and be scattered or absorbed).

Three main types of electron sources are used in electron microscopes including tungsten, lanthanum hexaboride (LaB_6), and field emission gun (FEG). Each represents a different combination of costs and benefits. The choice of source type is an important part of the instrument selection process. Perhaps the single most important characteristic of the source is brightness, which characterizes the electron current density of the beam and the angle into which the current is emitted (current density per steradian solid angle); and ultimately determines the resolution, contrast and signal-to-noise capabilities of the imaging system. FEG sources offer brightness up to 1000 times greater than tungsten emitters, but they are also much more expensive. In some high current applications, LaB_6 or tungsten may actually work better than FEG.

Contrary to what might be expected, most specimens are not adversely affected by the electron bombardment as long as beam conditions are controlled judiciously. When electrons impinge on the specimen, they can cause any of the following:

Some of the electrons are absorbed as a function of the thickness and composition of the specimen; these cause what is called amplitude (or mass thickness) contrast in the image.

Other electrons are scattered over small angles, depending on the composition and structure of the specimen; these cause what is called phase contrast in the image.

- In crystalline specimens, the electrons are scattered in very distinct directions that are a function of the crystal structure; these cause what is called diffraction contrast in the image.
- Some of the impinging electrons are deflected through large angles or reflected (back scattered) by sample nuclei.

- The impinging electrons can knock electrons from sample atoms which escape as low energy secondary electrons.
- The impinging electrons may cause specimen atoms to emit X-rays whose energy and wavelength are related to the specimen's elemental composition; these are called characteristic X-rays.
- The impinging electrons cause the specimen to emit photons (or light); this is called cathodoluminescence.
- Finally, transmitted beam electrons can be counted and sorted by an energy loss spectrometer according to the amount of energy they have lost in interactions with the specimen. The energy loss carries information about the elemental, chemical, and electronic states of the sample atoms.

In a standard TEM, mass thickness is the primary contrast mechanism for non-crystalline (biological) specimens, while phase contrast and diffraction contrast are the most important factors in image formation for crystalline specimens (most non-biological materials).

One limitation of the TEM is that, unless the specimen is made very thin, electrons are strongly scattered within the specimen, or even absorbed rather than transmitted.

Nitrogen sorption measurements

In physical adsorption study, the experimental information of dominant importance is the adsorption isotherm which is a plot of equilibrium amounts adsorbed (n_a in mmol g^{-1}) against the relative pressure (p/p^0) of the adsorbate.

Isotherms from N_2 -sorption measurements of catalysts contain specific information on the porosity of the particles. Information about the substance can be concluded already from the isotherm type. Such isotherms are classified into six shapes by IUPAC, shown in Figure iii.

Type-I isotherms reach a maximum value of adsorption without inflections and are characteristic of carbons containing only microporosity (very few materials do). The gradients of the initial part of the isotherm, with p/p^0 values between 0 ~ 0.05, are indicative of the dimensions of the

microporosity, the steeper the gradient the narrower are the micropores. **Type II isotherms** show an inflection in the region of $p/p^0 > 0.1$, and at high relative pressure, $p/p^0 > 0.9$, where extents of adsorption rise very rapidly. Such isotherms are characteristic of adsorption on open surfaces with multilayer formation occurring in the final stages of the process. **Type II isotherms** also describe adsorption in mixed situations of micropores and open surfaces. **Type III isotherms** are convex, looking upwards, and are characteristic of adsorption at sites of low adsorption potential, as is the case for adsorption on surfaces of organic polymeric systems. **Type IV isotherms** resemble Type II isotherms but additionally, instead of adsorption on open surfaces at high relative pressures, adsorption takes place in mesoporosity. Such isotherms may exhibit hysteresis when the mechanism of filling by capillary condensation in mesopores differs from that of mesopore emptying. **Type V isotherms** are those of a low energy, homogeneous solid surface possessing mesoporosity. **Type VI isotherms** are of surfaces with an extremely homogeneous structure (e.g. pyrolytic graphite) using, for example, argon and methane as adsorbates (but not nitrogen).

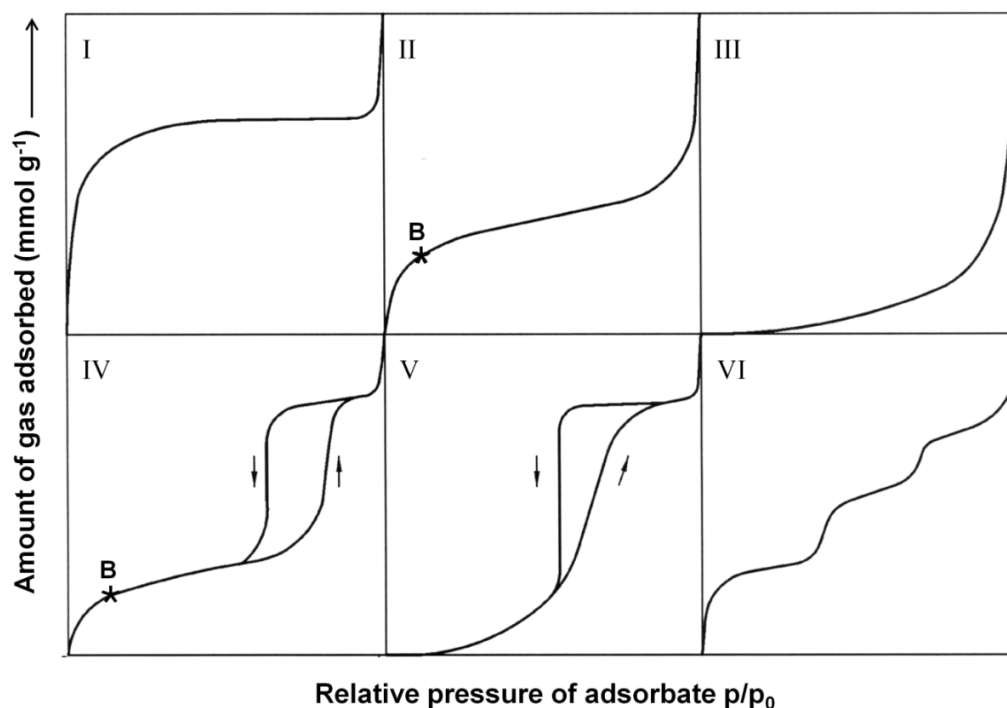


Figure iii. Classification of the isotherm types by IUPAC.

The Langmuir isotherm and Langmuir equation

The Langmuir isotherm was developed by Irving Langmuir in 1916 to describe the dependence of the surface coverage of an adsorbed gas on the pressure of the gas above the surface at a fixed temperature. There are many other types of isotherm (Temkin, Freundlich ...) which differ in one or more of the assumptions made in deriving the expression for the surface coverage; in particular, on how they treat the surface coverage dependence of the enthalpy of adsorption. Whilst the Langmuir isotherm is one of the simplest, it still provides a useful insight into the pressure dependence of the extent of surface adsorption.

Assumptions used for the Langmuir isotherm are:

1. Gaseous molecules behave ideally.
2. Only one monolayer forms.
3. All sites on the surface are equivalent.
4. No adsorbate – adsorbate interactions.
5. An adsorbate molecule is immobile.

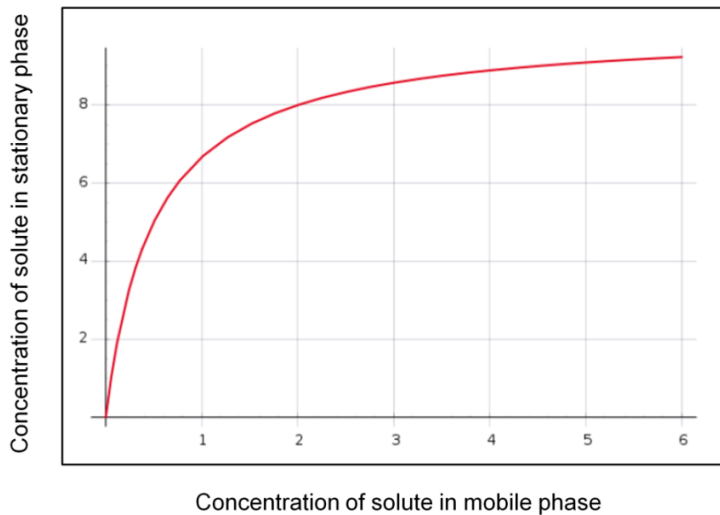


Figure iv The Langmuir isotherm.

$$\text{Langmuir Equation } \frac{p/p^0}{n^a} = \frac{1}{bn_m^a} + \frac{p/p^0}{n_m^a}$$

Where p = equilibrium vapor pressure (Pa), p^0 = saturation vapor pressure (Pa), n^a = amount adsorbed (mmol g^{-1}), n_m^a = monolayer capacity (mmol g^{-1}). The Langmuir equation is a plot of n^a against p/p^0 and provide a value for n_m^a (amount of adsorbate which forms a monolayer), which interprets the Langmuir isotherm.

The Langmuir isotherm gives us a wonderfully simple picture of adsorption at low coverage and is applicable in some situations. At high adsorbate pressures and thus high coverage, this simple isotherm fails to predict experimental results and thus cannot provide a correct explanation of adsorption in these conditions. What is missing in the Langmuir treatment is the possibility of the initial overlayer of adsorbate acting as a substrate surface itself, allowing for more adsorption beyond saturated (monolayer) coverage. This possibility has been treated by Brunauer, Emmett, and Teller and the result is named the BET isotherm. This isotherm is useful in cases where multilayer adsorption must be considered.

The BET isotherm and BET equation

The BET isotherm predicts that the amount of adsorption increases indefinitely as the pressure is increased since there is no limit to the amount of condensation of the adsorbate, which allows for multiple nitrogen molecules to adsorb to each stationary site.

The assumptions used to drive the BET isotherm are:

1. Gaseous molecules behave ideally.
2. Multiple nitrogen molecules can be adsorbed to each site.
3. Each adsorbed molecule provides a site for the adsorption of the molecule in the layer above it.
4. All sites on the surface are equivalent.
5. No adsorbate – adsorbate interactions
6. An adsorbed molecule is immobile.
7. Nitrogen in the second and higher layers is assumed to be liquid like.

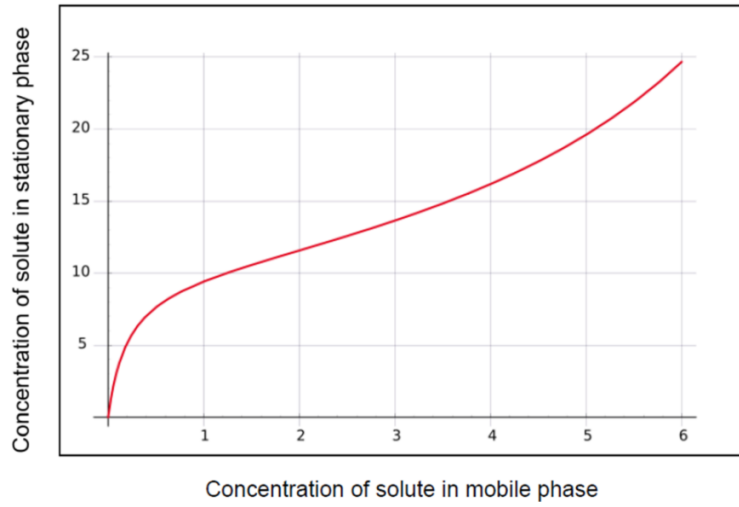


Figure v. The BET isotherm

$$\text{BET Equation } \frac{p}{V(p^0 - p)} = \frac{1}{V_m c} + \frac{(c-1)p}{V_m c p^0}$$

Where V = amount adsorbed in volume STP (cm^3/g), V_m = monolayer capacity in volume STP (cm^3/g), which interprets the BET isotherm. Similar as the Laugmuir equation, the BET equation also provides a value for n_m^a . The parameter c of the BET equation is indicative of the energetic of the adsorption process. The BET equation does not describe the entire isotherm from the relative pressure p/p^0 of 0.0 to 1.0. It is recommended by Rouquerol et al. (1999) that the best linear fit should include Point B of the isotherm. Point B is the position of n_m^a .

The BET isotherm is accurate when the relative pressure p/p^0 is between 0.05 ~ 0.3, at which pressures only a few complete layers have formed. At low pressures the BET isotherm does not do a good job at describing adsorption because in deriving the isotherm it was assumed that all the sites on the adsorbent surface are equivalent. This is not really the case and when only a few molecules have adsorbed, effects from inhomogeneities in the surface become more important. At high pressures, the cracks and roughness of the surface cause the BET isotherm to fail. This is especially true for very porous materials where the indents have a width of only a few monolayers. This is because the cracks can only hold a few monolayers and as the cracks fill up, the effective surface area of the solid where the nitrogen adsorbs can change.

The adsorption equations (the Langmuir equation and the BET equation) mentioned above predict values of monolayer capacity (n_m^a in mmol/g) which can be converted to an apparent surface area (A_s in $\text{m}^2 \text{g}^{-1}$) provided that the area effectively occupied by an adsorbed molecule (a_m in $\text{m}^2 \text{molecule}^{-1}$) can be estimated. Values of a_m are obtained from density data:

$$A_s = n_m^a N_a a_m$$

where N_a is the Avogadro constant, 6.013×10^{23} .

N₂ sorption measurement

Before each measurement the sample surface is being cleaned of water and low simmering organic compounds which might be adsorbed on the surface. For this surface cleaning (the so-called “out-gassing”) the sample is annealed under vacuum above 100 °C for a certain time (the appropriate temperature and time depend on the material).

Afterwards the measurement is performed. The measuring cell containing the sample is being evacuated and cooled down to the temperature of liquid nitrogen ($T = 77 \text{ K}$). At this temperature the N₂-sorption-isotherm is measured. For this, small amounts of the nitrogen gas (adsorptive) are injected into the cell step-by-step, which is being absorbed on the solid material’s (adsorbent) surface. This is a physisorptive interaction between nitrogen molecules and the sample surface, which is characterized by lower binding energy as opposed to the chemisorption. Dependent on the amount of the adsorbed nitrogen the pressure related to a specific introduced nitrogen-volume will decrease. During the measurements different pressures (expressed as relative pressure p/p^0 , p_0 is atmospheric pressure) are controlled and the amount of nitrogen introduced to reach this pressure is appointed. Therefore, the adsorption isotherm gives a plot of the volume of nitrogen (related to 1 g of material) as a function of the relative pressure p/p^0 .

At first a mono layer is formed on the surface of the solid material. By controlling larger relative pressures (adding more nitrogen) multi layers are forming. Parallel to the multilayer formation capillary condensation in the pores can occur. This process is described by the Kelvin-equation and correlates the pressure. In the last step of the measurement nitrogen is being desorbed step-by-step again until a specific relative pressure is reached.

Inductively coupled plasma mass spectrometry (ICP-MS)

Inductively Coupled Plasma Mass Spectrometry (ICP-MS) is an analytical technique used for elemental determinations. The technique was commercially introduced in 1983 and has gained general acceptance in many types of laboratories. An ICP-MS combines a high-temperature Inductively Coupled Plasma (ICP) source with a mass spectrometer. The ICP source converts the atoms of the elements in the sample to ions. These ions are then separated and detected by the mass spectrometer.

The sample is typically introduced into the ICP plasma as an aerosol, either by aspirating a liquid or dissolved solid sample into a nebulizer or using a laser to directly convert solid samples into an aerosol. Once the sample aerosol is introduced into the ICP torch, it is completely desolvated and the elements in the aerosol are converted first into gaseous atoms and then ionized towards the end of the plasma. Once the elements in the sample are converted into ions, they are then brought into the mass spectrometer via the interface cones. The interface region in the ICP-MS transmits the ions traveling in the argon sample stream at atmospheric pressure ($\sim 1\text{bar}$) into the low pressure region of the mass spectrometer ($<1 \times 10^{-5}$ torr). This is done through the intermediate vacuum region created by the two interface cones, the sampler and the skimmer (see Figure vi).

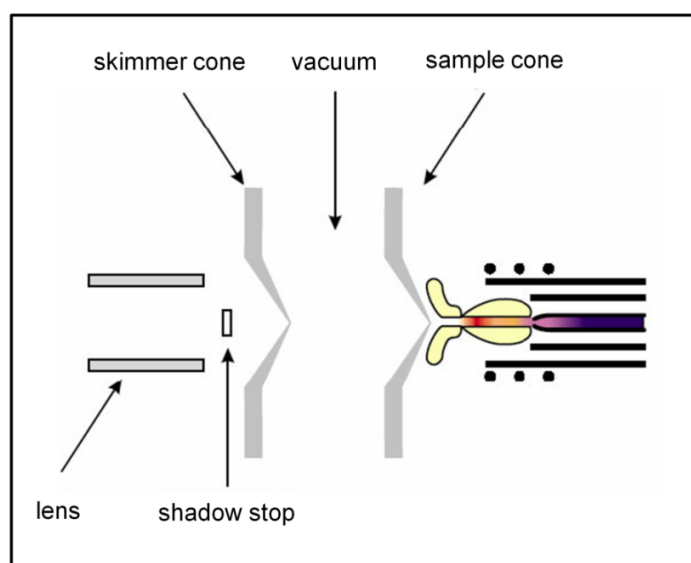


Figure vi. The interface region of an ICP-MS.

The interface region is one of the most critical areas of an ICP mass spectrometer. Its role is to help the ions be transported efficiently and with electrical integrity from the plasma, which is at atmospheric pressure (760 torr) to the mass spectrometer analyzer region at approximately 10^{-6} torr. The sampler and skimmer cones are metal disks with a small hole (~ 1 mm) in the center. The purpose of these cones is to sample the center portion of the ion beam coming from the ICP torch. A shadow stop (in Figure vi) or similar device blocks the photons coming from the ICP torch, which is also an intense light source. Due to the small diameters of the orifices in the sampler and skimmer cones, ICP-MS has some limitations as to the amount of total dissolved solids in the samples. Generally, it is recommended that samples have no more than 0.2% total dissolved solids (TDS) for best instrument performance and stability. If samples with very high TDS levels are run, the orifices in the cones will eventually become blocked, causing decreased sensitivity and detection capability and requiring the system to be shut down for maintenance. This is why many sample types, including digested soil and rock samples must be diluted before running on the ICP-MS.

The ions from the ICP source are then focused by the electrostatic lenses in the system. Remember, the ions coming from the system are positively charged, so the electrostatic lens, which also has a positive charge, serves to collimate the ion beam and focus it into the entrance aperture or slit of the mass spectrometer. Different types of ICP-MS systems have different types of lens systems. The simplest employs a single lens, while more complex systems may contain as many as 12 ion lenses. Each ion optic system is specifically designed to work with the interface and mass spectrometer design of the instrument. Once the ions enter the mass spectrometer, they are separated by their mass-to-charge ratio.

The versatility of ICP-MS makes it a good analytical technique for a wide variety of applications. This versatility is due not only to the large number of elements that can be determined rapidly at trace levels but also to the wide variety of sample types that can be analyzed using the ICP-MS technique.

Appendix D. Publications and conference contributions

Publications

1. Junjiang Zhu, **Xiao Xie**, Sónia A. C. Carabineiro, Pedro B. Tavares, José L. Figueiredo, Reinhard Schomäcker and Arne Thomas, *Energy Environ. Sci.*, **2011**, 4, 2020-2024.
2. Junjiang Zhu, Kamalakannan Kailasam, **Xiao Xie**, Reinhard Schomaecker and Arne Thomas, *Chem. Mater.*, **2011**, 23, 2062–2067.
3. **Xiao Xie**, Torsten Otremba, Patrick Littlewood, Reinhard Schomäcker and Arne Thomas, *ACS Catalysis*, **2013**, 3, 224-229.
4. **Xiao Xie**, Sabrina Nowag, Rainer Haag and Reinhard Schomaecker, *One-pot synthesis of silica xerogel supported Pd nanoparticles for catalytic applications*, manuscript submitted.

Oral and poster presentations

1. **Xiao Xie**, Sabrina Nowag, Rainer Haag, Arne Thomas, Reinhard Schomäcker. *One-pot approach synthesized Pd NPs supported on silica xerogel for catalytic applications*, NCCC XII-Netherlands Catalysis and Chemistry Conference, poster presentation, 2010, Amsterdam, Netherland.
2. **Xiao Xie**, Riny Parapat, Arne Thomas, Reinhard Schomäcker. *Loading noble metal nanoparticles into oxide supportes by different methods and application in hydrogenation reactions*, poster presentation, 2010, Weimar, Germany.
3. **Xiao Xie**, Torsten Otremba, Reinhard Schomäcker, Arne Thomas. *Synthesis of porous NiMnO and its application in dry reforming of methane*, International Symposium on Relations between Homogeneous and Heterogeneous Catalysis, oral presentation, 2011, Berlin, Germany.
4. **Xiao Xie**, Torsten Otremba, Arne Thomas, Reinhard Schomäcker, *A solid solution catalyst NiMnO for dry reforming of methane*, 6th Asia Pacific Chemical Reaction Engineering Symposium, poster presentation, 2011, Beijing, China.

Appendix E. Curriculum Vitae

Xiao Xie

Technical University of Berlin

Research Group Prof. Dr. Arne Thomas & Prof. Dr. Reinhard Schomäcker

Date of birth: 08. 04. 1981

Nationality: Chinese

Phone: +49 30 34089443

Mobile: +49 176 63145638

Email: xiaoxiexy@mail.com

Mail address: Gallwitzallee 73
12249 Berlin

Experiences

Technical University of Berlin

04.2009-11.2013

Graduate student with a scholarship from Berlin International Graduate School for Natural Sciences and Engineering (BIG-NSE) in the group of Functional Materials and the group of Chemical Engineering and Catalysis.

Project 1: “Designing an industrial catalyst for dry reforming of methane”.

Project 2: “Immobilization of noble metal nanoparticles onto porous silica materials for catalytic applications”.

Die DFG-Begutachtung von UniCat (Unifying of Catalysis) in Bonn

02.2012

A representative of BIG_NSE, responsible for providing the referees information about BIG_NSE school and polymer science program.

PhD Workshop (International PhD Programs for Top Graduate Students)

10.2009

Representative assistant, responsible for delivering information about funding application possibilities for abroad study opportunities, introducing BIG_NSE to final year undergraduate students.

Technical University of Berlin

10.2008-03.2009

Lab assistant in the group of Chemical Engineering and Catalysis.

Project: “Application of membrane reactor for catalyst separation and recycling in liquid phase reactions”.

Northwest University of Shanxi Province

08.2005-08.2006

Lab assistant in the group of analytical and environmental chemistry.

Project: "Micro flow reactor chips with integrated luminescence chemosensors for determination of pesticides residue in local vegetables and fruits".

Education

Ph.D in Material Science and catalysis

2009-2013

08.2013 - 10.2013 PhD graduation scholarship, Technical University of Berlin

04.2009 - 03.2013 BIG_NSE scholarship holder (DFG), Technical University of Berlin

Supervisors: Prof. Dr. Arne Thomas and Prof. Dr. Reinhard Schomäcker

Thesis: Synthesis of model nanocatalysts for industrial applications

M.S. in Polymer Science

2006-2008

Technical University of Berlin, Free University of Berlin, Humboldt University of Berlin and University of Potsdam, an international joint program

Supervisor: Prof. Dr. Reinhard Schomäcker (Technical University of Berlin)

Thesis: Synthesis of polycarbonate by polymerization of phenol and Bisphenol A in a FT-IR reactor

B.S. in Chemistry

2001-2005

Department of Chemistry, Northwest University in Xi'an City, China

Supervisor: Prof. Dr. Zhenhua Song

Teaching experience

2009-2012 tutor for Polymer Science lab, annually.

2010-2012 tutor for Polymer and Colloid Chemistry lab, annually.

Awards

2009, DAAD-Assistantship, Technical University of Berlin, Germany.

2005, the 2nd prize for the best students, Northwest University, China.

2004, the 3rd prize for the best students, Northwest University, China.

2003, the 3rd prize for the best students, Northwest University, China.